The Dissertation Committee for Chengshu Wang
certifies that this is the approved version of the following dissertation:

Velocity estimation from seismic data by nonlinear inversion and characterization of gas hydrate deposits offshore Oregon

Committee:

Mrinal K. Sen, Co-Supervisor

Robert H. Tatham, Co-Supervisor

Nathan L. B. Bangs

Robert J. Ferguson

Paul L. Stoffa

Velocity Estimation from Seismic Data by Nonlinear Inversion and Characterization of Gas Hydrate Deposits Offshore Oregon

by

Chengshu Wang, B.E., M.Sc.

Dissertation

Presented to the Faculty of the Graduate School of
The University of Texas at Austin
in Partial fulfillment
of the Requirements
for the Degree of

DOCTOR OF PHILOSOPHY

The University of Texas at Austin
August 2003

Dedication

To My Parents

Acknowledgments

I would like to express my deepest gratitude to my advisor, Dr. Mrinal K. Sen, for his guidance, inspiration, encouragement, and support throughout my dissertation work. I would also like to thank my co-supervisor, Dr. Robert H. Tatham, for his comments and suggestions. I would like to thank Dr. Nathan Bangs for many discussions on Oregon data and serving on my dissertation committee. I thank Dr. Kirk McIntosh for many discussions on Costa Rica data. I would like to thank Dr. Robert J. Ferguson and Dr. Paul L. Stoffa for serving as my committee members.

I wish to thank Dr. Noel Tyler, my former supervisor, who offered me support for my admission to PhD program in Geological Sciences and for my studies during the first two academic years. I also thank Dr. Bob Hardage for his support for my studies in the Fall semester 1998, and Drs. Yosio Nakamora and Jay Pulliam for their support for my studies in the Fall semester 1999. I would like to acknowledge the support of the Weeks Fellowship from the Geology Foundation, and the Ewing/Worzel fellowship from the Institute for Geophysics.

I would like to thank Drs. Indrajit Roy, Lopamudra Roy, Ranjit Shaw, Youlong Xia, and Qianzhen Mu for their kind help in my dissertation work. I would also like to extend my thanks to my former and current fellow students at the Instutite for Geophysics: Junru Jiao, Faqi Liu, Anubrati Mukherjee, Imtiaz Ahmed, Xun Hao, Dhananjay Kumar, Armando Sena, Xinxia Wu, Hongbo Lu, Mingjuan Shi, Deon Dempsey, Donna Cathro, Sylvia Nordfjord, Robert Rogers, Tip Meckel, Alejandro

Escalona, and Ricardo Combellas-Bigott. Disscussions with them made my studies effective and their rich, diverse cultural background made my life more enjoyable and diverse. I give my special thanks to my friends Qing Fang, Ning Li, Bingwen Hao and Chuanbing Wu for their help during the beginning of my studies in Austin, to my friends Jinhua Chen, Wei Gao for their help in my studies, and to my friends Yan Zhang, Chenyang Wei, Honghui Deng, Haifeng Zhu, Lihui Lin, Shengli Wu, Bing Jiang, Zhidi Shang, Linyun Zhu, Dongyuan Wang, Shaochang Wang, and Xiajun Yang for their sharing life with me in Austin.

I offer special thanks to many staff at the Institute for their help. I specially thank Mark Wiederspahn, Kevin Johnson, Steffen Saustrup, Jonh Gerboc, Lisa Gahagan for their technical support, Judy Sansom, and Nancy Hard for their kind help.

This dissertation is the result of consistent education and training. I thank all my teachers for their instructions and my colleagues for their cooperation and help. I especially acknowledge Dr. Hongzhen Wang, my former supervisor for M.Sc. degree at China University of Geosciences (formerly named Wuhan College of Geology), for leading me to research in Geology. I also acknowledge Prof. Xiufu Qiao, my mentor at Chinese Academy of Geological Sciences, for his cooperation and help in my research of Geology.

I would like to give my sincere thanks to my parents for their positive influence in my life. In his lifetime, my father always encouraged me to positively face and accept challenges.

Velocity Estimation from Seismic Data by Nonlinear Inversion and Characterization of Gas Hydrate Deposits Offshore Oregon

Publication No. _________________

Chengshu Wang, Ph.D.
The University of Texas at Austin, 2003
Supervisors: Mrinal K. Sen
Robert H. Tatham

Seismic attributes such as traveltimes and reflection amplitude variation with offset contain information on the elastic parameters of subsurface rocks. The aim of generalized inversion of seismic data is to estimate values of the elastic parameters such as P-wave velocity, S-wave velocity and density for lithology discrimination and direct detection of hydrocarbons. My dissertation research comprises two parts: development of a method to improve the least-squares and the preconditioned conjugate gradient algorithm, and estimation of detailed velocity structure of gas hydrate-bearing sediments offshore Oregon from Ocean-bottom seismometers (OBS) and multi-channel streamer (MCS) data.

I developed a new nonlinear inversion algorithm for estimating velocities from fully stacked reflection data with application to a field data set consisting of well logs from Ocean Drilling Program (ODP) Leg 170 and multi-channel seismic reflection (MCS) data offshore Costa Rica. Inversion of post-stack seismic data generally yields reflection coefficients or impedance as a function of two-way reflection time. In this experiment, fully stacked seismic data and density logs at selected locations along a 2-D seismic line are inverted to estimate seismic velocities. Mathematically, generalized inversion provides the best estimate of earth model parameters by minimizing the so-called cost (or misfit between observed and computed seismic data) function, which is a function of the data covariance matrix $\mathbf{C}_D$ and the *a priori* model covariance matrix $\mathbf{C}_M$. Matrices $\boldsymbol{C_D}$ and $\boldsymbol{C_M}$ (generally approximated by scalars σ_d and σ_m) introduce stability to the process and robustness and thus have strong influence on the quality of the final inversion solution. Based on the least-squares and the preconditioned conjugate gradient algorithm, I have developed a 2-step procedure to solve this nonlinear inverse problem by first determining the two matrices $\boldsymbol{C_D}$ and $\boldsymbol{C_M}$ using the two-step procedure that involves mapping the sensitivity of model smoothness and data error to the parameters σ_d and σ_m .I found that there always exits an area in the $\sigma_d\sigma_m$ plane in which the low values of the cost function lie, and hence a large 2-dimensioanl search space can be reduced to a significantly smaller search region. This led to the easy application of this method.

The results from this experiment show that almost every identified reflector of seismic data is very well matched by final synthetic seismograms and the density from borehole log data, which confirms that my estimates of velocities are reliable. Combination of the inverted velocity and density profiles allows identification of major stratigraphic boundaries.

The improved inversion method is extended to the inversion of pre-stack seismic data, which is applied to estimate seismic velocities of gas hydrate-bearing sediments, offshore Oregon. Gas hydrates are recognized as a target for major future energy reserves, are believed to be a potential source of an important greenhouse gas, and are considered to be a possible cause of submarine geo-hazard. A simple indicator of gas hydrate is a bottom-simulating reflector (BSR), which marks the transition between hydrate-bearing sediments with high V_p above free gas with low V_p. A 3-D streamer and ocean bottom seismometer (OBS) survey in the Hydrate Ridge, offshore Oregon was conducted to image structures controlling the migration of methane-rich fluid and free gas and to map the gas-hydrate distribution. Preliminary V_p and V_s profiles obtained from OBS data by interactive analysis are used as a starting model to estimate V_p from the streamer data.

The results of my inversion and interpretation study in Hydrate Ridge are summarized below:

- Both 3-D streamer and OBS data show a strong BSR indicating the presence of gas hydrate above and free gas below.
- Interactive P- and S-wave velocity analysis of OBS data allows us to identify the presence of a "conversion surface" in the gas hydrate-bearing sediments. The conversion surface separates the overlying low P-wave velocity layer and underlying high P-wave velocity layer.

- Inverted velocity profiles show a low-velocity layer existing below the sea floor and above the normal gas hydrate, suggesting a new geological model of gas hydrates.
- Two types of hydrate fabrics, massive and porous hydrates, observed by deep-towed video survey, were identified in the P-wave velocity profiles. Three main layers of gas hydrate-sediments separated by the conversion surface and BSR are distinguished. Below the free gas is the normal sedimentary section.
- The profiles reflecting the physical properties of sediments, such as the P-wave velocity, acoustic impedance and Poisson's ratio profiles, are able to map the distribution of gas hydrates and show very similar trends of lateral variation of the main layers.
- A series of faults in the accretionary complex under the ridge not only offer pathways for methane and fluid ascending from deeper layers but also control the distribution of the porous hydrates with low velocity below the seafloor.
- Hornbach et al. (2003) suggest their results using velocity analysis of seismic reflection data on the Blake Ridge is the first direct seismic detection of concentrated hydrate confirmed by velocity analysis. My results of direct inversion of seismic data extend these results to greater resolution of the entire seismic data set. Further, my results may be the first seismic indication of a visually observed porous hydrate zone.

TABLE OF CONTENTS

Page

LIST of FIGURES

Chapter 1: Introduction

1.1 Objectives

One of the main objectives of seismic exploration is to find a reliable image of the Earth's subsurface for locating major stratigraphic sequences from a seismic reflection response and to obtain estimates of physical properties of individual layers for identifying lithology. Various migration techniques applied to poststack and prestack seismic data provide the structural image. AVO or waveform inversion techniques use the amplitude and traveltime information of the reflection to extract physical properties which vary on a spatial scale consistent with the seismic frequency band.

Seismic attributes such as traveltimes and reflection amplitude variation with offset (AVO) contain information on the elastic parameters of the rocks such as the P-wave velocity, S-wave velocity and density in isotropic media. In transversely isotropic media we consider vertical P-wave velocity, vertical S-wave velocity and three dimensionless anisotropic parameters ε, γ and δ. The aim of inversion of seismic data is to directly estimate the values of these elastic parameters to describe the subsurface and to ultimately identify lithology, fluid properties and other rock properties. For this purpose, inverse theory and various inversion methods have been developed. Since the recorded seismic data depend nonlinearly on the parameters describing the earth, nonlinear inverse methods are developed for solving inverse problems. One important element of inversion is 'optimization', which is employed to find an earth model corresponding to the minimum of a function that measures the misfit between observed and numerically predicted (synthetic) data. Global optimization methods such as a genetic algorithm and simulated annealing, and local optimization methods such as conjugate gradient algorithm and Newton's method are popular in geophysics. In my dissertation research, I have used inversion techniques with local optimization for estimating rock properties from seismic reflection data. In particular, I have studied the characteristics and distribution of gas hydrate bearing sediments as derived from inversion of seismic reflection data.

Gas hydrates, found in marine, permafrost, and lake environments worldwide, have recently become a major focus of international research. Gas hydrates are important primarily because they may store large amounts of methane, and secondarily because they influence the physical properties of the gas hydrate-bearing sediments masking images of deeper structure. The estimation of physical properties of the gas hydrate-bearing sediments from seismic data allows us to identify the presence of gas hydrates, to study their character, formation and distribution, and to estimate the amount of gas hydrate and/or free gas that may be present in the sediments. The inversion of seismic data offers a tool for the remote extraction of physical properties of the sediments from surface-recorded data.

In my dissertation research, I apply the least-squares and the preconditioned conjugate gradient algorithm to acoustic impedance inversion and pre-stack waveform inversion. I have developed an algorithm to determine a data covariance matrix C_D and a priori model covariance C_M of the cost function for use in post- and pre-stack waveform inversion. My experiments are based on field data. I use data recorded with ocean-bottom seismometers (OBS) and multi-channel streamer (MCS) from offshore Oregon to estimate velocities of the gas hydrate-bearing sediments by interactive velocity analysis and pre-stack waveform inversion.

My project includes two parts: developing a method to improve the least-squares and conjugate gradient algorithm for inversion of seismic data, and applying the method to estimate velocities of gas hydrate-bearing sediments offshore Oregon from OBS and MCS data.

Part I—Improvement of the inversion algorithm—involves the application of the algorithm to a field data set consisting of borehole data from Ocean Drilling Program (ODP) Leg 170 and multichannel seismic reflection (MCS) data offshore Costa Rica. In the experiment of estimating velocities using 1-D waveform inversion, I solve the inverse problem using an iterative least squares approach in which a smooth error function comprising a data and a model misfit is minimized using a conjugate gradient scheme. The data covariance matrix C_D and the *a priori* model covariance matrix C_M introduce stability and robustness and thus have strong influence on the quality of the final result. However, no detailed method has been previously introduced to determine the two matrices. The main objectives of the experiment include:

- Developing effective methods to determine matrices C_D and C_M based on the preconditioned conjugate gradient algorithm,
- Poststack waveform inversion for P-wave velocity from the offshore Costa Rica field data set using the inproved inversion method, and

- Geological interpretation.

Part II—the offshore Oregon experiment—focuses on velocity estimation of gas hydrate-bearing sediments by combining the OBS and MCS data. The main objectives of this experiment include:

- Interactive P- and S-wave velocity analysis from OBS data;
- Prestack waveform inversion for P-wave velocity from MCS data using the improved preconditioned conjugate gradient algorithm, and
- Interpretation of the formation and distribution of gas hydrates at Hydrate Ridge.

1.2 Inverse Theory and Methods

1.2.1 Inverse theory

Inverse theory is an organized set of mathematical techniques for reducing data to obtain useful information about the physical world on the basis of inferences drawn from observations (Menke, 1984). The observations of "the world" consist of a set of measured data, and the specific properties of "the world" are called model parameters. We assume that there is some specific method, usually a mathematical theory or a model, for relating the model parameters to the data. The relationship between data and model parameters can be expressed by an implicit vector equation as follows

$$\mathbf{f}(\mathbf{d}, \mathbf{m}) = 0, \tag{1.1}$$

where **d** is the data vector, and **m** the model parameter vector.

There are two problems to be solved: forward and inverse. Forward theory is defined as the process of predicting observed data (the results of measurements), which starts with model parameters and some model, and finally produces the predicted data. The forward problem is briefly described as:

model parameters → model → prediction of data.

The general forward model is given by:

$$\mathbf{d} = \mathbf{g}(\mathbf{m}), \tag{1.2}$$

where **m** is the model parameters, **d** the predicted data, and **g** a (linear or nonlinear) operator mapping the model space ***M*** into the data space ***D***.

Inverse theory addresses the reverse problem, which starts with data and a model, and ultimately determines estimates of the model parameters. The inverse problem is briefly described as:

data → model → estimation of model parameters.

Basically, the inverse problem means a quest for information (Tarantola and Valette, 1982). Generally, inverse problems are substantially more difficult to solve than their corresponding forward problems and solutions are generally non-unique because they are inherently unstable.

Inverse problems arise in many branches of the physical sciences, leading inverse theory to be developed by scientists and mathematicians having various backgrounds and goals. Therefore, various inverse methods for different problems have been developed in a variety of scientific disciplines.

1.2.2 Inverse methods

The inverse methods developed in geophysics may be classified into (1) operator-based or direct-inverse methods and (2) optimization or model-based inverse methods (Hampson, 1991; Sen and Stoffa, 1995). In operator-based inversions, such as Born-type inversion, recursive inversion, layer stripping inversion and migration, observed data are used directly to estimate the model parameters without an iterative process. Inversions of this type are based on certain mathematically reversible models. In model-based inversions, in addition to an assumption of particular mathematical description of the relation between the model parameters and the observed data, synthetic data need to be produced to initially compare with the observed data. After the initial synthetic data are compared with the observed data, the model parameters are revised and updated, and then new synthetic data are generated and compared with the observations. The process is repeated until sufficient agreement between the observed and the synthetic data is achieved. In this case, inversion is a mathematical optimization process in which model parameters are sought to best explain the observed data (Sen and Stoffa, 1995). The function to be optimized is variously called the objective function, cost function, misfit function or fitness function. The best estimate is defined herein as the parameter set from which synthetic data can be computed to best fit the observed data. The flow chart of an optimization process is shown in Fig. 1.1.

For model-based inversion algorithms, the performance of the inversion procedure depends critically on the technique used for solving the forward problem, i.e., particular mathematical equations describing the relationship between the model

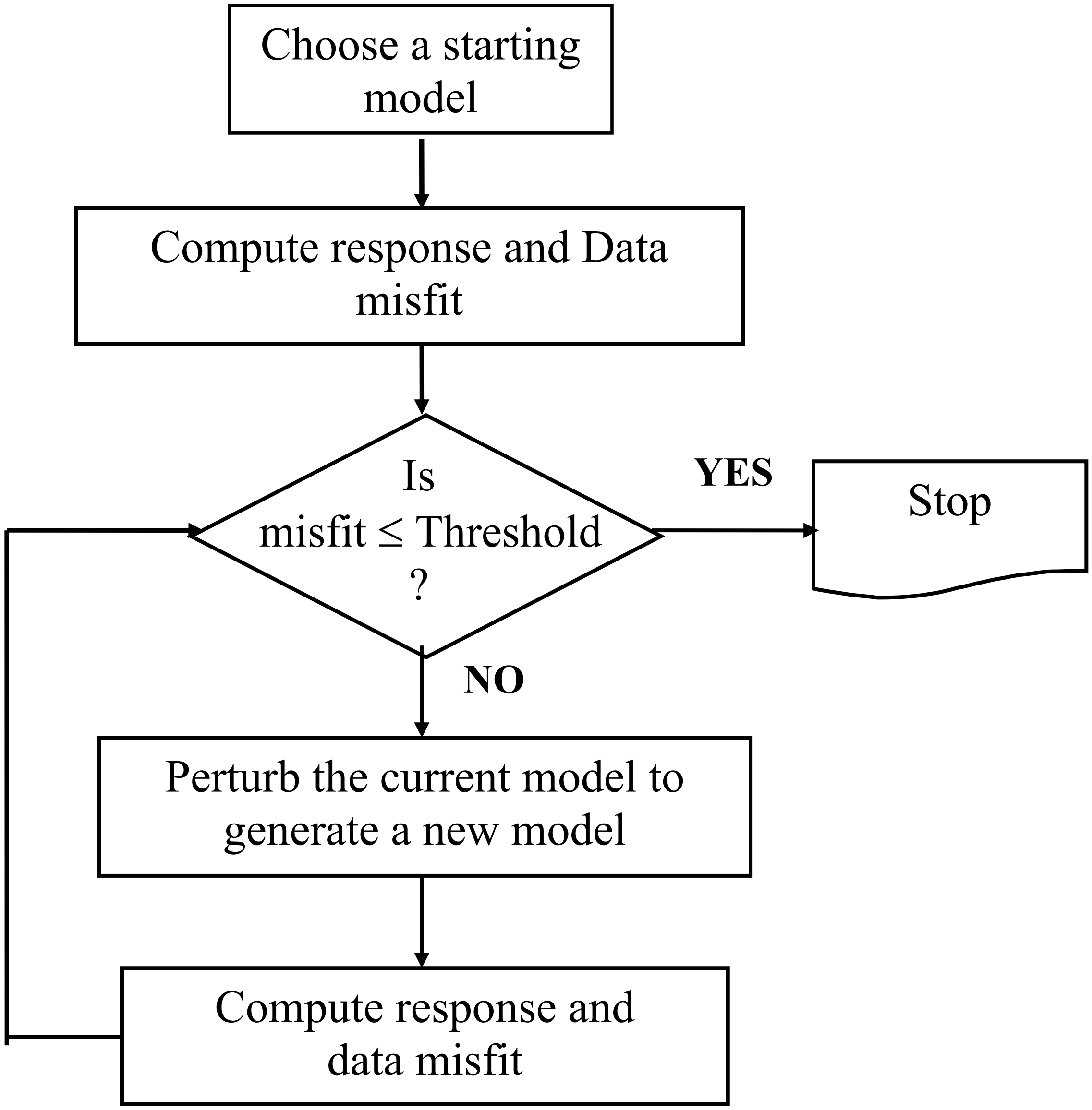

Fig. 1.1 Flow chart of an optimization.

parameters and the observed data. Also, careful selection of the initial model minimizes the inherent effects of non-uniqueness associated with the method. Facing the fact that the observed seismic data depend nonlinearly on the appropriate model parameters, people have developed two types of techniques to compute synthetic seismograms: linearizing forward modeling for linearized inversion (Clayton and Stolt, 1981; Tarantola, 1984a; Ikelle et al., 1986, 1988), and nonlinear forward modeling for nonlinear inversion (e.g., Tarantola, 1984a, 1987; Sen and Stoffa, 1995).

To solve an inverse problem using a model-based optimization approach, some *a priori* constraints are often added to derive geologically meaningful results. In the nonlinear model-based inversion, there are two groups of techniques for nonlinear optimization: local optimization and global optimization (Gauthier et al., 1986; Sambridge and Drijkoningen, 1992). Local optimization, including steepest descent, and conjugate gradient techniques, uses local information about the gradient of the objective (cost or misfit) function to improve upon some starting model in an iterative fashion. Global optimization applies random processes to search the model parameter space to find better model parameters. Using Bayesian statistics, the solution of an inversion problem is described by the *a posteriori* probability density function (PPD) which is proportional to the product of a likelihood function and prior probability density function. In a local optimization approach, one finds a best fit model. A Gaussian PPD is assumed and the curvature of the error function at the best-fit model is used to compute the posterior co-variance of the model. On the other hand, when we use global optimization schemes, there is no need to assume the shape of the PPD and complex PPD can be sampled using a Gibbs' sampler (Sen and Stoffa, 1996). However, often given a good prior knowledge of the geology of an area, a local optimization may be reasonably cost effective.

The linearized inversion is heavily influenced by the choice of an initial model. Thus, some knowledge of local geological conditions is essential. If a starting model is known to be reasonably close to the actual medium, linearized inversion will probably perform well. Without the dependence of the initial model, global optimization methods for solving nonlinear inversion problems can produce a mathematically best fitness in a given model parameter space, but it does not guarantee a physically reasonable result. A local optimization method can find the correct solution when the starting model is inside the valley of the so-called global minimum (Fig. 1.2). In practice, if there is a "good" initial model derived from other related measurements, local optimization may be the most efficient method. Using a local optimization method this nonlinear inverse problem can be solved iteratively by using a generalized least-squares formalism. A conjugate gradient technique is often chosen for solving the resulting system of equations.

In exploration geophysics, some special inverse methods have been developed to solve particular practical problems. In my dissertation research, the related inverse methods include acoustic impedance inversion and prestack waveform inversion.

1.3 Acoustic Impedance Inversion

Acoustic impedance is the product of rock density and seismic P-wave velocity, which means that the acoustic impedance is a bulk rock property rather than an interface

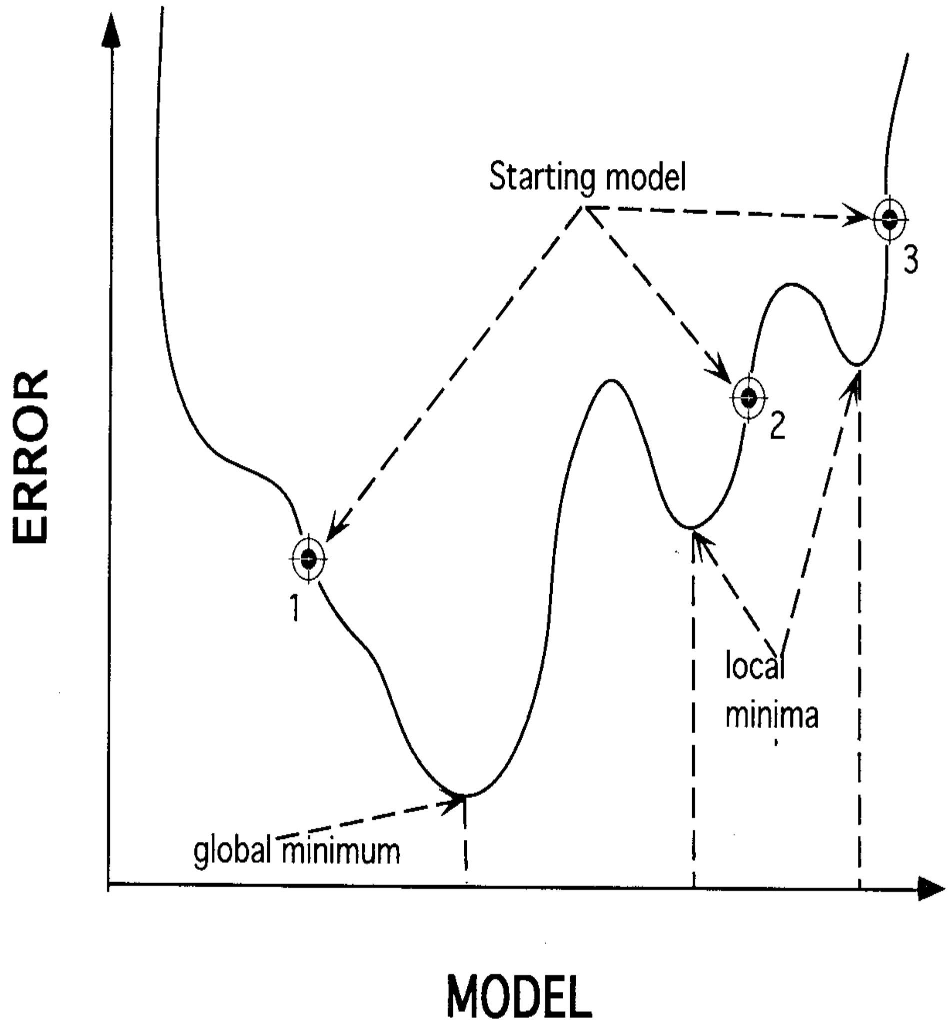

Fig. 1.2 A hypothetical error function as a function of model (the model is assumed to have only model parameter) showing several minima. The iterative gradient method will find the global minimum only when starting at position 1. Other will end up in secondary minima of the error function. (after Sen and Stoffa, 1995)

property, such as seismic reflection strength. Acoustic impedance yields important information concerning the nature of the rock and changes in lithology. Inversion of seismic data to acoustic impedance is a rapidly growing field, due primarily to the ease and accuracy of interpretation of the impedance data (Latimer et al., 2000). Traditionally, the acoustic impedance is recovered as a function of traveltime (or depth) from observed normal incidence seismograms by 1-D seismic inverse method such as a recursive inversion (Bamberger et al., 1979; Lindseth, 1979; Bamberger et al., 1982; Berteussen, and Ursin, 1983; Oldenburg et al., 1983; Ursin, 1986). The estimate of the acoustic impedance series may be considered the reversal of the process used to compute a synthetic seismogram from an acoustic impedance log. An estimate of the primary reflection coefficient series is first obtained from reflection seismic data by very careful data processing, and then the reflection coefficients are converted into acoustic impedance by a simple recursive formula. There are two methods to solve this inverse problem: direct inversion and model-based inversion.

1.3.1 Direct-inverse method for acoustic impedance inversion

A direct-inverse method for estimating acoustic impedance was employed by several researchers (Becquey et al., 1979; Lindseth, 1979; 1982; Berteussen, and Ursin, 1983). The key step for this inverse method is to obtain the reflection coefficient series directly from reflection seismic data. In practice, initial data processing, including true-amplitude recovery and deconvolution, is necessary to produce an estimate of the reflection coefficient series.

Minimum entropy deconvolution (Wiggins, 1977) and sparse-spike inversion (Oldenburg et al., 1983) are two approaches that aim to recover a sparse, blocky impedance model by attempting to reproduce the data with a limited number of simple interface reflections (reflectivity spikes). Simmons and Backus (1996) developed a matched-filter algorithm to impedance estimation. In the matched-filter algorithm, a trace is modeled as a superposition of simple interfaces, high impedance layers, and low impedance layers. This parameterization permits a parsimonious blocky model of the impedance.

We assume that the earth is an isotropic stratified elastic medium represented by a stack of thin homogeneous layers (Fig. 1.3a). The seismogram, denoted by s(t), may be considered to be a result of a convolution of a reflection function r(t) with a known (or at least well approximated) wavelet w(t). That is:

$$s(t) = r(t)*w(t). \tag{1.3}$$

Fig. 1.3(b) shows the relationship between a reflection function (being a function of the earth's acoustic impedance) and an ideal seismic trace.

The acoustic impedance in the kth layer is defined as

$$z_k = \rho_k v_k\,, \tag{1.4}$$

where ρ_k and v_k are the mass density and velocity respectively. The reflection coefficient at the base of the kth layer (r_k) in terms of the adjacent acoustic impedances is defined as follows:

$$r_k = \frac{z_{k+1} - z_k}{z_{k+1} + z_k}\,, \qquad k = 1, 2, 3, \ldots, \tag{1.5}$$

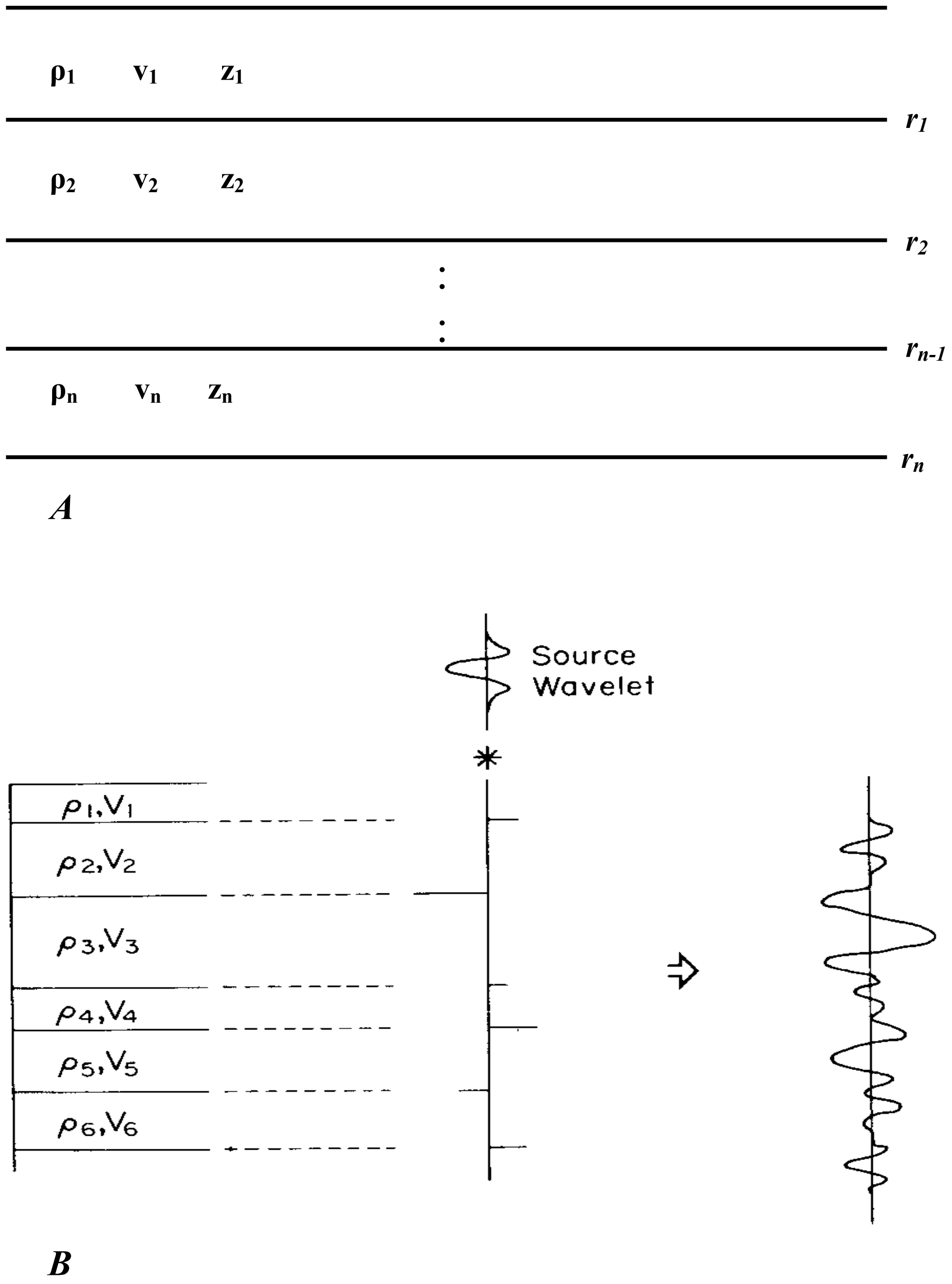

Fig. 1.3 (A) General model describing n layers of the isotopic media. (B) The relationship between the earth's acoustic impedance function and an ideal seismic trace.

Equation (1.5) can be rewritten to express z_{n+1} in terms of z_n and r_n:

$$z_{k+1} = z_k \frac{1+r_k}{1-r_k}, \qquad k = 1, 2, 3, \ldots, \tag{1.6}$$

which is a recursive formula. The acoustic impedance Z_1 in the first layer is assumed to be known. By successive applications of equation (1.6) we obtain the nonlinear expression:

$$z_{k+1} = z_1 \prod_{j=1}^{k} \frac{1+r_j}{1-r_j}, \tag{1.7}$$

which relates the acoustic impedance to the reflection coefficients.

Deconvolution of the seismogram (here equation (1.3)) will yield an estimate of the reflection coefficient series, and then acoustic impedance series can be computed using equation (1.7). Another method, sparse-spike deconvolution is used by Oldenburg et al. (1983) to recover a sparse, blocky impedance model.

Recursive inversion is an excellent method of quickly and inexpensively estimating relative impedance changes, but absolute impedance information is very difficult to obtain with this method and resolution is highly dependent on the success of wavelet removal.

1.3.2 Model-based inverse method for acoustic impedance inversion

To apply model-based inversion, a so-called forward model is used to generate synthetic seismic data. A forward model for acoustic impedance inversion is expressed by equation (1.3), which can be rewritten in discrete form as:

$$s_{syn}(t) = \sum_{i=1}^{nl} w(t) \bullet r_0(t - t_i), \tag{1.8}$$

where $s_{syn}(t)$ = synthetic seismograms, $w(t)$ = source wavelet, r_0 is the normal incidence reflection coefficient series defined by adjacent acoustic impedances, *nl* is the number of layers. If the observed seismic data (s_{obs}) is known, the error or cost function *e* can be defined as:

$$e = \sum_{i=1}^{nl} (s_{obs} - s_{syn})^2 \ . \tag{1.9}$$

To solve this acoustic impedance inversion, there are two commonly used methods. The earliest method was generalized linear inversion (Cooke and Schneider, 1983), which is based on a Taylor series expansion of the forward model without assumption that the data and *a priori* model parameters (here acoustic impedances) have Gaussian distributions with covariance C_D and C_M, respectively. Recently, genetic algorithm (Nolte and Frazer, 1994) and very fast simulated annealing (McIntosh and Sen, 2000) were used to estimate acoustic impedance profiles.

1.4 Pre-stack Waveform Inversion

The aim of waveform inversion is to obtain the contrast in physical properties across the reflecting surface by using amplitude and traveltime information of either poststack or prestack data. In general, the physical properties obtained from a prestack inversion method provide more detailed stratigraphic features of the subsurface than a poststack inversion method can provide. This is mainly because pre-stack seismic data contain more fundamental information, such as true-amplitudes at multiple offsets, as well as moveout and reflector times than fully stacked data. This additional information may enable prestack waveform inversion to be capable of recovering acoustic impedance and Poisson's ratio. These physical properties can be used to infer the subsurface lithology and fluid saturant properties.

The waveform inversion method estimates model parameters, $\mathbf{m}$, of the subsurface by matching recorded seismic data, $\mathbf{d}(t, \mathbf{x}_j)$, with equivalent synthetic data , $\mathbf{u}(t, \mathbf{x}_j, \mathbf{m})$, produced by using the estimated model parameters. The method used to calculate the synthetic seismograms, $\mathbf{u}(t, \mathbf{x}_j, \mathbf{m})$, depends on the data set, $\mathbf{d}(t, \mathbf{x}_j)$, and the model, $\mathbf{m}$, the information required from the inversion and computing considerations. In practice, the choice of an appropriate modeling methodology is crucial in implementing a stable prestack inversion process. For a given model, $\mathbf{m}$, virtually any method of calculating synthetic seismograms, $\mathbf{u}(t, \mathbf{x}_j, \mathbf{m})$, is only approximate. Three methods for the physics of forward problem have generally been developed: reflectivity, ray-tracing and finite-difference methods.

The reflectivity method (Fuchs and Muller, 1971; Kennett, 1983) for the computation of synthetic seismograms in layered media is widely used. This method computes the seismic response of plane waves in the frequency-wavenumber domain by a matrix method that automatically includes contributions from all possible generalized rays within the reflecting zone, and then the responses for the individual plane waves are summed to generate seismograms in the offset-time domain (field or shot record) using a Fourier-Hankel transformation. No ray expansion is necessary but the synthetic seismograms are band-limited in horizontal slowness and frequency. If the input seismic data are decomposed into individual plane wave components, it is possible, using the reflectivity method, to compute plane-wave synthetic seismograms to match the observed seismic data. Because of the assumption that the earth model must be horizontally stratified, the reflection method does not work well for inversion in structurally complex areas. Although the original reflectivity formulation computes a complete seismic response including mode conversions and multiple reflections, it is not difficult to limit the formulation to obtain primary reflection mode conversion (PP- and PS- waves) energy only, or primary and multiple PP-wave energy only, or primary PP-wave energy only. Application of the Radon transform (or plane-wave decomposition) to the solution of the wave equation (and to the source and to common-midpoint gathers of the data) reduces 3-D model to 1-D models (Treitel et al., 1982). The reflectivity method is a good choice for generating 1-D synthetic PP- and PS-wave seismograms.

The ray-tracing methods, based on the asymptotic solution of the Eikonal equation, are fast, flexible and well suited for application to the calculation of synthetic seismograms for three-dimensionally heterogeneous earth models, even in anisotropic media (e.g., Cerveny, 1972; Gajewski and Psencik, 1987). The decomposition of the wavefield into individual arrivals, such as reflections from a specific interface, allowed by the ray approach gives a clear intuitive understanding of the effects of different parts of the model on seismic observations which is not possible with full waveform approaches. The most fundamental aspects of the asymptotic ray-tracing method are based on a high-frequency solution to the wave equation for a 3-D, inhomogeneous, anisotropic medium. These methods calculate only the most of the singular part of the solution, which is characterized by a traveltime function and an amplitude function. The traveltime function is a solution of the Eikonal equation, and the amplitude function is a solution of the transport equation (Carcione et al., 2002). They are perhaps the most efficient of the three methods for calculation of synthetic seismograms, especially for large, 3-D models. Ray-tracing methods and their extensions have been applied for linearized inverse formulations (e.g., Chapman and Orcutt, 1985) and nonlinear inverse formulations (Mora, 1985).

Finite-difference methods are numerical methods that provide an accurate means to solve the forward problem of computing seismograms for arbitrarily complex earth models. To solve the wave equation by finite-difference methods, the geological model is approximated by a numerical mesh; that is, the model is discretized into a finite numbers of points. These methods are able to compute seismic response, including mode conversions and intra-bed multiple reflections for 2-D or 3-D media. Since the pioneering work of Alterman and Karal (1968), two different formulations have arisen: the homogeneous formulation requiring explicit boundary conditions, and the heterogeneous formulation requiring implicit boundary conditions (Kelly et al., 1976). A principal disadvantage of finite-difference methods is that they can be more computationally intense, and hence more expensive than reflectivity and ray methods in terms of computer time.

1.5 A New Approach for Least-squares and Conjugate Gradient Algorithm Applied to Inversion of Seismic Data

The generalized least-squares approach to seismic inversion involves a systematic search for an earth model which best fits the observed seismic data in a least-squares sense. Since the observed seismic data depend nonlinearly on the parameters describing the earth, nonlinear inversion should be used to estimate the parameters. Nonlinear least-squares techniques have proven to be useful for performing such an inversion (Tarantola and Valette, 1982; Tarantola, 1984; Lines and Treitel, 1984; Mora, 1987, 1988; Norton, 1988; Pica et al., 1990; Kormendi and Dietrich, 1991). The nonlinear inverse problem can be solved using iterative gradient techniques with the final result, a maximum probability estimate of elastic parameters. Because of its simplicity and good convergence properties, the preconditioned conjugate gradient method of nonlinear least-squares inversion has been effectively applied to the seismic inverse problem (e.g., Tarantola, 1984b; Mora, 1987, 1988; Kormendi and Dietrich, 1991; Sen and Roy, 2002). Mathematically the best estimate of model parameters using this optimization method is obtained by minimizing a so-called cost (or misfit) function which is a function of the data covariance matrix and the *a priori* model covariance matrix. Although these two matrices have a key influence on the final inversion solution, little attention is paid on how to determine them. I have developed an effective method for determining these two matrices in AVO and nonlinear waveform inversion problems in isotropic media and applied them to the problems of estimating the character of subsurface sediments and gas hydrates.

1.6 Gas Hydrates: A New Focus of International Research

Gas hydrates, crystalline substances of an expanded solid-water lattice with cages trapping guest gas molecules (largely methane), are formed at low temperature and high pressure in marine sediments when gas concentrations exceed those which can be held in solution (Sloan, 1990). Natural gas hydrates occur worldwide in marine, permafrost, and lake environments. Since their natural occurrences were reported in the early 1970s, gas hydrates have attracted increasing attention of the scientific community because they may represent (1) a major future energy source, (2) a potential source of an important greenhouse gas, and (3) a possible cause of a submarine hazardous condition (geohazard) (Kvenvolden, 1993).

Three kinds of evidence have been used to identify the presence of natural gas hydrate—geological, geochemical and geophysical (Kvenvolden and Lorenson, 2001). Geological evidence includes sediment properties, stratigraphic relationships, gas-migration pathways, and, more importantly the description and actual recovery of gas-hydrate samples. Pore fluid chemistry and gas compositions are important aspects of gas hydrate chemistry. Geophysical evidence includes seismic and well-logging data. The seismic signature of gas hydrates on seismic reflection sections is commonly represented by a bottom simulating reflector (BSR), mimicking the sea bottom topography within the sedimentary section.

The discovery of large gas hydrate accumulations in terrestrial permafrost regions of the Arctic and beneath the sea along the outer continental margins of the world's oceans has heightened interest in gas hydrates as a possible energy resource. However, gas production from gas hydrates is not a present-day objective for the petroleum industry (Grauls, 2001). Some major issues concerning gas hydrates, such as their origin and potential gas recovery, are still poorly understood. This lack of knowledge precludes pursuing new deposits as an exploration target for an additional energy source.

Chapter 2: Velocity estimation from post-stack seismic data and density log by an nonlinear inversion of multi-channel seismic data, offshore Costa Rica

Seismic wave velocities through sediments in trench slope areas at convergent plate margins are important for identifying stratigraphic units, detecting geological structures and investigating hydrogeologic processes at convergent plate boundaries. The changes in seismic P-wave velocity in vertical profile follow the vertical variations of physical properties of sediments and rocks, which offer the geophysical base of stratigraphic division. A series of velocity profiles across a regional profile demonstrate the character of sediments and rocks and their lateral changes, which allow us to directly detect geological structure by stratigraphic correlation of seismic reflections. The velocity profile is also the basis of seismic reflection imaging. The velocity profiles are used in estimation of thickness of stratigraphic units which show the lateral thickness variations of sedimentary section, and can be used to interpret dewatering and deformation processes at convergent margins (McIntosh and Sen, 2000). One of my objectives is to develop an effective method to estimate the velocities of sediments and basement rocks. The work reported here is aimed at the analysis of post-stack seismic and well log data from the ODP Leg 170 area offshore Costa Rica, a convergent margin (Fig. 2.1).

Investigations of the internal structure, formation and evolution of modern accretionary margins rely on the combination of drilling and seismic reflection profiles.

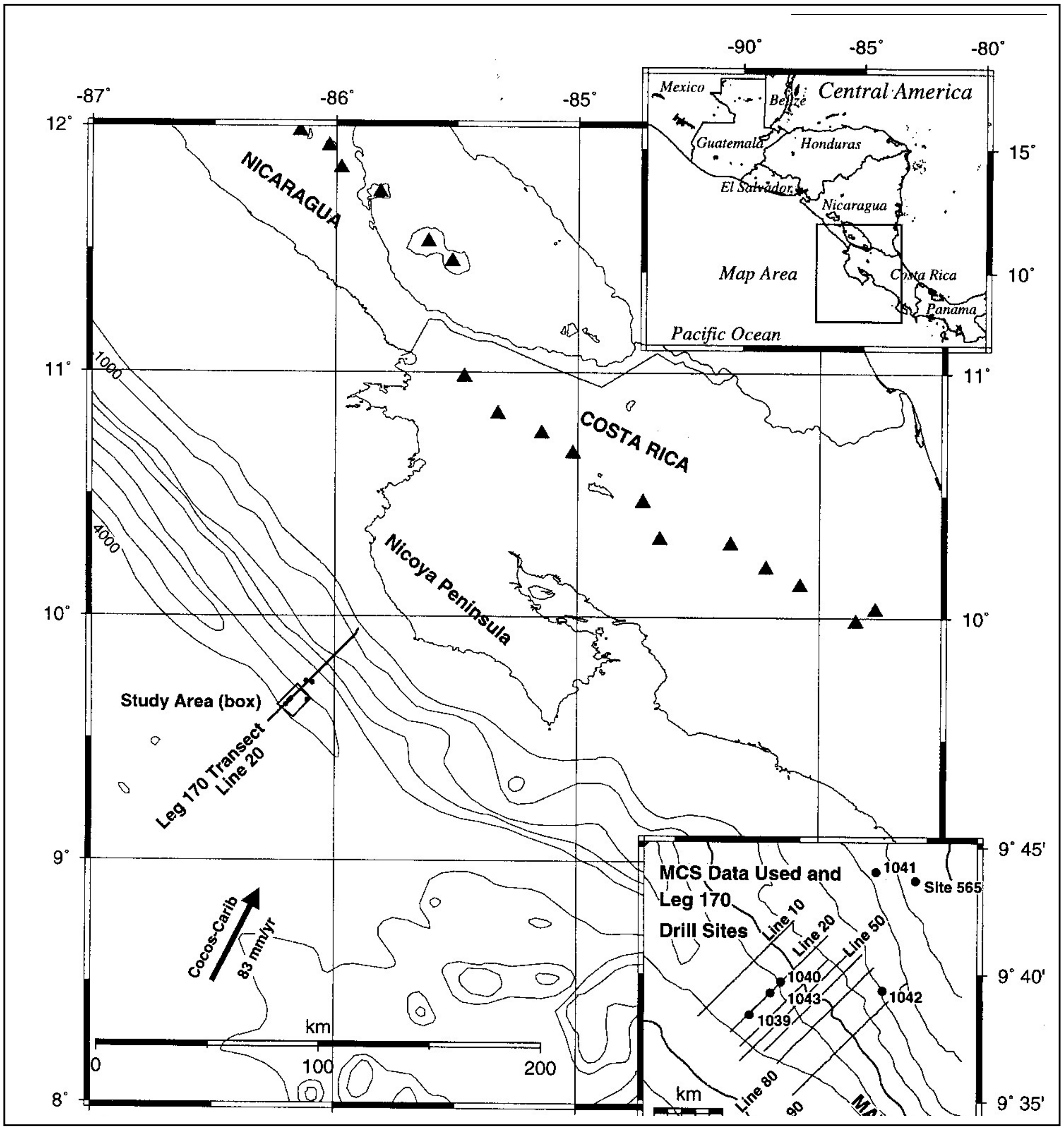

Fig. 2.1. Location map showing study area off the Nicoya Peninsula, Costa Rica. Upper insert shows the regional geographic setting; lower insert shows the portions of the MCS lines used in this investigation, Leg 170 ODP drill sites and Site 565 from DSDP Leg 84. Black triangles on land mark the volcanoes of the Central America volcanic arc. Plate convergence vector is calculated from De Mets et al. (1994). (after McIntosh and Sen, 2000).

Seismic reflection imaging is a primary tool for investigating structural, statigraphic and hydrogeological processes at convergent margins. However, at the great depths of most trenches, especially where the sedimentary section is thrust beneath a complex upper plate, it is difficult to determine precise velocities directly from the multichannel seismic reflection (MCS) data. Borehole data from the Ocean Drilling Program (ODP) allow reliable description of physical property changes and the detection of the thickness variation of underthrust sediments, but these data are restricted to point locations associated with drilling. To systematically explore the active processes at convergent margins, it is better to take advantage of both the reliable drilling data and the more regional distribution of the MCS data.

The main objectives of the research reported in this chapter are to improve the least squares and the preconditioned conjugate gradient algorithm, and then to apply the improved algorithm to estimate seismic P-wave velocities of sediments and basement rocks in a trench slope area. For this, I address the inverse problem of estimating velocities by 1-D post-stack waveform inversion using a field data set consisting of borehole data from Ocean Drilling Program (ODP) Leg 170 and multichannel seismic reflection (MCS) data offshore Costa Rica **(**Fig. 2.1). McIntosh and Sen (2000) used the same data set to quantify thickness changes in underthrust sediments away from the boreholes. They estimated the velocity profiles of three ODP drilling sites by 1-D waveform inversion using a nonlinear optimization algorithm called very fast stimulated annealing (VFSA) to minimize the cost (error) function. The inverse method they used is a global optimization technique. Because we have reliable density data and a good estimate of the initial model, I try to use a local optimization technique, the least squares and the preconditioned conjugate gradient algorithm, to solve the inverse problem in greater detail. This is motivated by the fact that it is more convenient to incorporate prior information and it is easy to use over-parameterized models in a local optimization scheme. Therefore, I revisit the problem of inversion of post-stack seismic data with a new application and a new approach to regularized inversion. In my experiment, I have (1) the observed data (selected CDPs from post-stack seismic data), (2) well-log derived density at selected locations along a 2-D seismic line and (3) rough estimates of smooth variations in P-wave velocities. My goal is to obtain better velocity estimates by seeking the best data fitting.

Inversion of post-stack seismic data may yield acoustic impedance as a function of two-way reflection time, from which estimate of velocity profile can be derived when the density profile is known. Traditional impedance inversion of a recursive scheme (e.g., Wiggins, 1977; Becquey etal., 1970; Lindseth, 1979; 1982; Berteussen and Ursin, 1983; Oldenburg et al., 1983, Ursin, 1986) is an excellent method of quickly and inexpensively determining relative impedance changes, but absolute impedance information is very difficult, if not impossible, to obtain with this method alone. To realize detailed impedance information for a complex inverse problem, model-based inversion with iterative process (Cooke and Schneider, 1983; Nolte and Frazer, 1994; McIntosh and Sen, 2000) is a better choice. In the present inverse problem of post-stack seismic data, additional complexity in the model parameter estimation problem occurs in that changes in velocity cause changes in two way travel time, and hence non-linearity is introduced.

Unlike generalized linear inversion (Cooke and Schneider, 1983), genetic algorithm (Nolte and Frazer, 1994) and simulated annealing (McIntosh and Sen, 2000), I solve the inverse problem using an iterative least squares approach in which a smooth error functional comprising a data and a model misfit is minimized using a conjugate gradient scheme. The data covariance matrix C_D and the a priori model covariance matrix C_M introduce stability and robustness and thus have strong influence on the quality of final inversion solution. Based on the preconditioned conjugate gradient algorithm, I have developed effective methods to determine the constant diagonal elements or the weights to model and data norms using a variant of an L-curve technique.

Combination of the estimated velocities and acoustic impedance profiles at the same site allows me to give a general geological interpretation of the subject profile along MSC Line 20.

2.1 Forward modeling

In my experiment, I consider an isotropic stratified elastic medium which consists of a stack of thin homogeneous layers less than ½ or ¼ of the shortest wavelength contained in the seismic data. Therefore, the earth model is described by three parameters that vary with depth and locations. I chose density, the P-wave velocity, and the S-wave velocity to describe the layers. For 1-D post-stack seismic data, synthetic data can be generated simply by convolution when the normal incidence reflection coefficient that is dependent only on density and P-wave velocity is given.

The forward model for this experiment is a very simple convolution given by:

$$f(t) = \sum_{i=1}^{nl} S(t) \bullet R_0 (t - t_i), \tag{2.1}$$

where *f*(t) is the synthetic seismograms, *nl* the number of layers, *S*(t) the source wavelet, R_0 the normal incidence reflection coefficient vector given by the acoustic impedance contrast between two consecutive layers:

$$R_0 = \frac{Z_2 - Z_1}{Z_2 + Z_1}, \tag{2.2}$$

where $Z = \rho V$ is the acoustic impedance. We assume that the wavelet is known and vectors $\boldsymbol{\rho}$ (from log density data) and $\boldsymbol{V}$ (starting or updated model) are given, and hence I can compute the synthetic seismograms *f*(t).

2.2 Inversion Method

To solve the problem of nonlinear acoustic impedance inversion of post-stack seismic data, I use the least squares and the preconditioned conjugate gradient algorithm initially developed by Taratola (1984b). Mathematically the best estimate of model parameters using this optimization method is obtained by minimizing a so-called cost (or misfit) function which is a function of the data covariance matrix C_D and the *a priori* model covariance matrix C_M. Matrices C_D and C_M have strong influence on the quality of final inversion solution because of their introduction of stability and robustness. Therefore, an important factor for obtaining better estimate of velocity profile is to determine the matrices C_D and C_M which are able to strike a balance between data fitting and model smoothness.

2.2.1 Least squares and the preconditioned conjugate gradient algorithm

The general nonlinear forward model is given by:

$$\mathbf{d} = \mathbf{f}(\mathbf{m}), \tag{2.3}$$

where $\mathbf{m}$ is an earth model vector (parameters), $\mathbf{d}$ is the seismic data vector, and $\mathbf{f}$ is a nonlinear operator mapping the model space M into the data space D.

Because seismic data are often contaminated with noise, we have to devise methods to deal with uncertainty in measurements in practical inversion applications. Typical problems encountered in any inversion include non-uniqueness, illposedness and instability. However, these problems can be addressed systematically by using probability theory that provides us with tools to incorporate *a priori* information on the data and model parameters. The central limit theorem states that the sum of independent noise distributions tends to have a Gaussian distribution. Model parameters in general are not Gaussian distributed, but this limitation can be at least partially handled by allowing the model mean to vary with iteration (Mora, 1987). By assuming a Gaussian-distributed model and data errors, Taratola (1984b) developed an inversion algorithm that is an iterative least squares approach using the preconditioned conjugate gradient method. The method was extended further by Mora (1987) and Kormendi and Dietrich (1991). Given a Gaussian-distributed model and data spaces, the joint *a posteriori* probability function is given by

$$P(\mathbf{d}, \mathbf{m}) = \text{constant} \bullet \exp\left[-\tfrac{1}{2}\left(\Delta\mathbf{d}^T \mathbf{C}_D^{-1} \Delta\mathbf{d} + \Delta\mathbf{m}^T \mathbf{C}_M^{-1} \Delta\mathbf{m}\right)\right], \tag{2.4}$$

where $\Delta\mathbf{d} = \mathbf{d} - \mathbf{d}_{\text{obs}} = \mathbf{f}(\mathbf{m}) - \mathbf{d}_{\text{obs}}$ is the data misfit vector corresponding to the earth model parameters $\mathbf{m}$ and data observations $\mathbf{d}_{\text{obs}}$, $\Delta\mathbf{m} = \mathbf{m} - \mathbf{m}_0$ is the model perturbation vector measured relative to the a priori model $\mathbf{m}_0$, and $\mathbf{C}_D$ and $\mathbf{C}_M$ are the *a priori* data covariance and model covariance matrices respectively. The superscript T denotes the transpose of a matrix.

Clearly, the solution corresponding to the maximum probability (also called maximum *a posteriori* or MAP solution) can be obtained by minimizing the least-squares function, also known as cost (or misfit) function, given by:

$$S(\mathbf{m}) = \tfrac{1}{2}\,(\Delta\mathbf{d}^T\mathbf{C}_D^{-1}\Delta\mathbf{d} + \Delta\mathbf{m}^T\mathbf{C}_M^{-1}\Delta\mathbf{m}), \tag{2.5}$$

which is a function of the data covariance matrix $\mathbf{C}_D$ and the a priori model covariance matrix $\mathbf{C}_M$.

Because of its simplicity and good convergence property, I chose the preconditioned conjugate gradient method of nonlinear least-squares to minimize the cost function for the case of nonlinear function $\mathbf{f}(\mathbf{m})$. The algorithm is iterative with background model varying with each iteration and is further summarized by Kormendi and Dietrich (1991) as follows (see appendix in detail):

Step 1: Compute the synthetic data $\mathbf{d}_n$ for $\mathbf{m}_n$

$$\mathbf{d}_n = \mathbf{f}(\mathbf{m}_n), \qquad n = 0, 1, 2, \ldots.$$

Step 2: Compute the data residuals $\Delta\mathbf{d}$

$$\Delta\mathbf{d}_n = \mathbf{d}_n - \mathbf{d}_{\text{obs}},$$

and the discrepancies with respect to the *a priori* model $\Delta\mathbf{m}_n$

$\Delta\mathbf{m}_n = \mathbf{m}_n - \mathbf{m}_0$.

Step 3: Compute the cost function $\boldsymbol{S}(\mathbf{m}_n)$

$\boldsymbol{S}(\mathbf{m}) = \frac{1}{2}(\Delta\mathbf{d}^T\underline{\mathbf{C}}_D{}^{-1}\Delta\mathbf{d} + \Delta\mathbf{m}^T\underline{\mathbf{C}}_M{}^{-1}\Delta\mathbf{m}),$

and apply the stopping test (exit if converged).

Step 4: Compute the direction of steepest ascent Γ_n

$\Gamma_n = \underline{\mathbf{C}}_M\underline{\mathbf{F}}_n{}^T\underline{\mathbf{C}}_D{}^{-1}\Delta\mathbf{d} + \Delta\mathbf{m}_n,$

where $\mathbf{F}_n = \partial\mathbf{f}/\partial\mathbf{m}_n$ is the Frechet derivative matrix.

Step 5: Compute the conjugate direction Φ_n

$\Phi_n = \Gamma_n + \sigma_n\Phi_{n-1} \qquad (\Phi_0 = \Gamma_0).$

Step 6: Compute the optimum step μ_n to minimize the cost (misfit) function. The optimum step is the heart of the algorithm and is computed by using a three-point parabolic inverse interpolation.

Step 7: Update the model $\mathbf{m}_n$

$\mathbf{m}_{n+1} = \mathbf{m}_n - \mu_n\Phi_n,$

and go back to step (1).

The data covariance matrices C_D and C_M are analogous to data and model weighting matrices that reflect our knowledge on the error in data and level of certainty in the prior model. I describe these matrices in detail in the following section.

2.2.2 Data covariance matrix $\mathbf{C_D}$ and *a priori* model covariance matrix $\mathbf{C_M}$

Because experimental data are never perfect, a covariance operator is used to describe the uncertainties in a data set. The diagonal elements of the covariance matrix are a measure of the width of the distribution of the data, and the off-diagonal elements indicate the degree to which pairs of data are correlated. Therefore, a covariance operator describes not only the estimated variance of each particular datum but also the estimated correlation between errors.

As shown in equation (2.5), the least-squares cost function is defined as a function of the data covariance matrix $\mathbf{C}_D$ and the *a priori* model covariance matrix $\mathbf{C}_M$. Before undertaking the preconditioned conjugate gradient algorithm the matrices $\mathbf{C}_D$ and $\mathbf{C}_M$ must be determined. In general, it is extremely difficult to correctly estimate these matrices. For practical applications, they are chosen such that they introduce stability and help derive realistic estimates. Although $\mathbf{C}_D$ and $\mathbf{C}_M$ play a key role in such least-squares optimization method, no detailed discussion on how to determine them has been given so far. If these were assumed to be arbitrary, not only excessive computer storage and CPU time would be required but also convergence may not be attained. In practice, diagonal matrices are often chosen. However, the covariance matrixes need not be constant but may vary along the diagonal with the assumption of independent, but nonconstant, noise and independent model parameters. Therefore, the covariance matrixes $\mathbf{C}_D$ and $\mathbf{C}_M$ need to be chosen carefully to obtain the best estimates of model parameters.

In my experiment of estimating velocities using 1-D waveform inversion for acoustic impedance with the conjugate gradient technique, three *a priori* conditions are imposed on the determination of C_D and C_M:

- I assume that the observed data are uncorrelated,
- The diagonal matrix is chosen as the forms of both C_D and C_M for data fitting,
- A second derivative weighting factor for model smoothness is used to determine matrix $\mathbf{C}_M^{-1}$ in real data case.

Unlike most existing algorithms, the inversion is a two-step procedure in which I search for optimal regularization weights in the first step of inversion and then in the second step allow for detailed data fitting. Application to field data resulted in an excellent data fit and allowed for a detailed stratigraphic interpretation.

2.3 Field Data Experiment

2.3.1 Geological and tectonic setting

The study area (Fig. 2.1) is along a portion of the Middle America Trench (MAT) off the Nicoya Peninsula, Costa Rica, where the oceanic Cocos Plate, of late Oligocene age (Klitgord and Mammerickx, 1982; Meschede et al., 1998), subducts beneath the western edge of the Caribean Plate at a rate of about 83 km/Myr (or 8.3 cm/yr) (DeMets et al., 1994). Onshore, the Nicoya Peninsula is a complex mixture of oceanic igneous and associated sedimentary rocks, which probably consists of Late Cretaceous, oceanic, intraplate volcanics and intrusives and the associated Late Cretaceous and younger sedimentary rocks overlying Jurassic to Early Cretaceous oceanic crust (Galli-Olivier, 1979; Schmidt-Effing, 1979; Lundberg, 1982; Meschede and Frisch, 1994; Sinton et al., 1997) and may be part of the Caribbean Cretaceous oceanic plateau (Donnelly, 1994). Offshore, the top of the oceanic crust can be traced (in seismic reflection profiles) landward beneath the continental slope and shelf to a depth of about 9 or 10 km. The slope is divided into an upper portion, the slope cover, consisting of late Miocene and early Pliocene to Recent terrigenous muds (Aubouin et al., 1982), and a lower portion, the accretionary prism. There is no detectable trench fill, only the incoming about 250 m of oceanic pelagic carbonates and about 175 m of more terrigenous hemipelagic sediments on the late Oligocene crust of the Cocos plate are being carried into the margin (Shipley et al., 1990). At the trench axis, recent ODP drilling at site 1039 reveals that the Cocos plate stratigraphy consists of three sedimentary units and one intrusive unit (Kimura et al., 1997). According to Kimura et al. (1997), these units are Unit U1 (Underthrust 1), consisting of hemipelagic olive green diatomaceous ooze with numerous ash layers, Unit U2, composed of hemipelagic silty clay, Unit U3, consisting of pelagic calcareous ooze with breccias of debris flows and turbidites (U3C), and Unit U4, composed of pyroxene gabbro representing the basement of oceanic sediments. Recent wide-angle seismic experiments extending across the Nicoya Peninsula and the offshore margin to the MAT show that the onshore velocity structure, representing the Nicoya Complex, continues offshore to within less than about 20 km of the trench (Bialas et al., 1996; Christeson et al., 1999).

The convergent margin off the Nicoya Peninsula of Costa Rica has been the site of many surveys including seismic reflection surveys (von Huene and Flueh, 1994), and Deep Sea Driling Project (DSDP) and Ocean Drilling Program (ODP) drilling (von Huene et al., 1985; Kimura et al., 1997). The primary goals of these projects have been to identify the crustal structure of the margin, and to investigate the processes that have shaped the margin, and the currently active processes. ODP Leg 170 drilled at one site (1039) on the Cocos Plate, as a reference section, and at four sites (1040 to 1043) into the toe of the upper plate wedge (Fig.2.2). Reference Site 1039 sampled an approximately 152 m thick hemipelagic section with ages 0-5 Ma, an approximately 225 m thick pelagic section with ages 5-16.5 Ma, and a post-15.6 Ma age gabbroic intrusion (Kimura et al., 1997). The entire section sampled at the reference site was also penetrated as the underthrust section at Sites 1043 and 1040. In April 1987, a multichannel seismic (MCS) survey was conducted to image the 3-D structural geometry of the continental margin off the Nicoya Peninsula of Costa Rica (Stoffa et al., 1991; Shipley et al., 199). The 3-D seismic imaging maps the main subsurfaces (stratigraphic boundaries). The velocity profile is a key for the production of a correct subsurface image and for the description of the physical properties of sediments and rocks at the lower trench slope. Therefore, my new inversion method will be used to estimate velocities of sedimentary section at the lower trench slope area.

2.3.2 Brief data description

Three drilling locations, Sites 1039, 1043 and 1040, are distributed along MCS

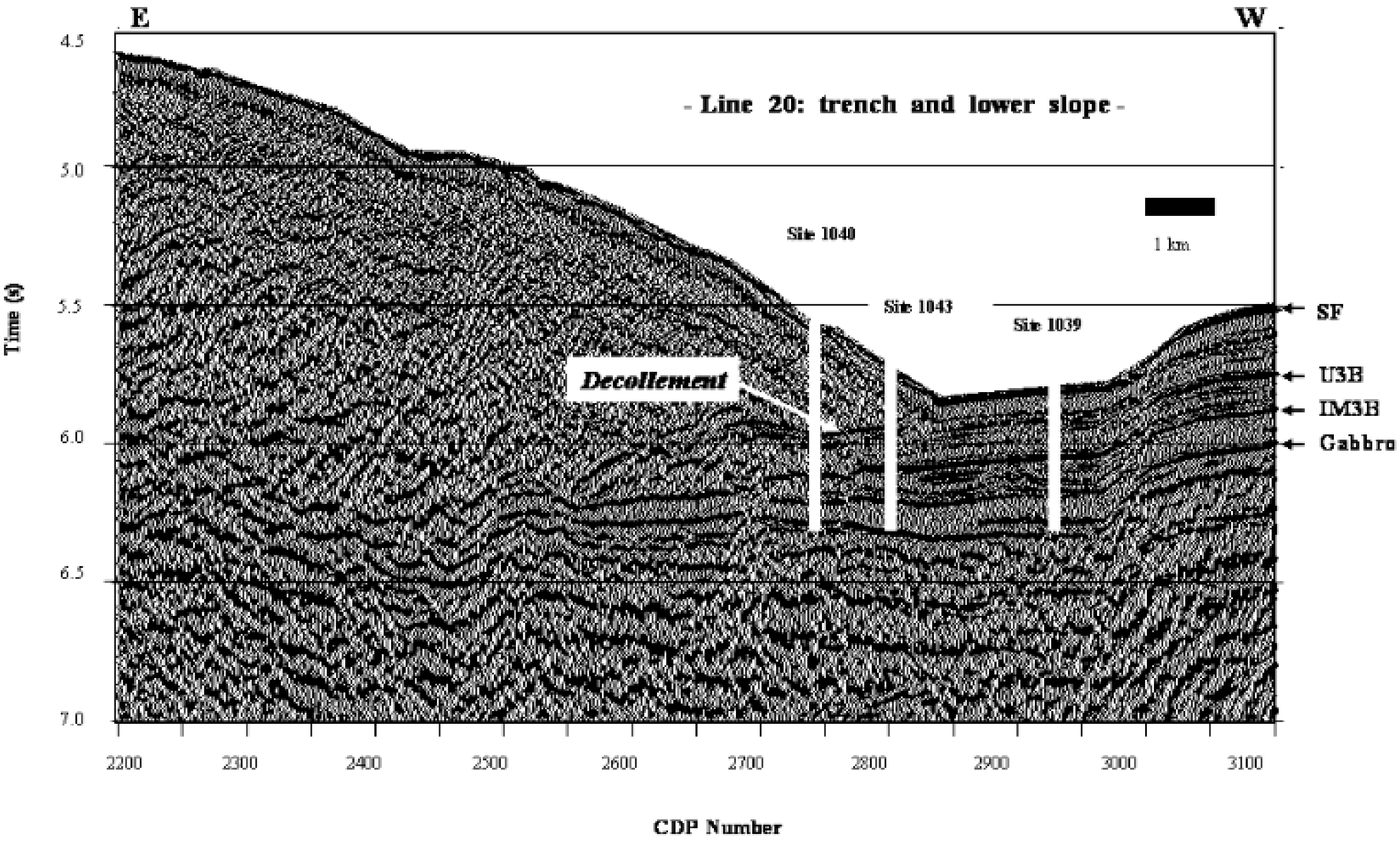

Fig.2.2. Part of post-stack time-migrated section of Multi-channel seismic (MCS) Line 20 showing trench and lower slope off the Nicoya Penisula, Costa Rica. Three seaward drill sites of Leg 170 transect are marked. Site 1039 is the reference site on Cosos Plate while sites 1043 and 1040 cross the toe of the upper plate and the underthrust sedimentary section. All three holes penetrated to the basement of the Cocos Plate, here consisting of Gabbro sills.

Line 20 (Fig.2.2). All three boreholes penetrated to sedimentary basement on the Cocos Plate consisting of gabbroic sills. Fig.2.2 displays the post-stack time-migrated section of MCS Line 20 across the trench and the lower slope with drill sites indicated. From the seismic section we can see the Cocos plate stratigraphy, including the hemipelagic/pelagic boundary (~6 s at Site 1039) and the gabbroic intrusion at the basement of the sedimentary section. The landward decollement is also demonstrated by a phase-reversed reflection (relative to seafloor). Borehole data include the borehole-compensated density logs recorded by the logging while drilling (LWD) tool, which is a high fidelity record of the vertical density variations. At sites 1039 and 1043, LWD logs were obtained from seafloor to the basement, but at site 1040 LWD logs were recorded only from the seafloor to a depth near the decollement. In addition, the seismic wavelet, derived by stacking a large number of traces windowed to include only an uncomplicated portion of the seafloor reflection, and rough estimates of P-wave velocities were obtained by McIntosh and Sen's work (2000).

Therefore, in this experiment, I have the following initial data:

(1) the stacked seismic traces along Line 20 ,
(2) the relatively accurate but sparse density data from borehole logs at selected locations along a 2D seismic line, and
(3) preliminary estimates of P-wave velocities.

My objective is to obtain better, more precise P-wave velocity estimates. Traditionally, the seismic traces (observed data) are first transformed into pseudoreflection-coefficient time series, and then converted into relative acoustic impedance variations using a recursive algorithm. The corresponding P-wave velocities can be derived from the acoustic impedance variations and the given density profile. To obtain better velocity estimates, an iterative process can be used to find the impedance distribution directly which minimizes the misfit between synthetic and observed seismograms.

2.3.3 New approach: Determination of covariance matrices $\mathbf{C_D}$ and $\mathbf{C_M}$

I assume that the data are uncorrelated and all observation values have equal variance, then the diagonal elements of the data covariance matrix are constant, and the n×n matrix is defined as:

$$\mathbf{C}_D = \sigma_d^2 \mathbf{I}, \tag{2.6}$$

where **I** is the n×n identity matrix and σ_d^2 the variance of the elements of the seismic data vector.

For the determination of $\mathbf{C}_M$, two cases should be distinguished: data fitting and model (velocity) smoothing. For data fitting I define the n×n matrices as:

$$\mathbf{C}_M^{-1} = \sigma_m^{-2}\mathbf{I} \quad \text{and} \quad \mathbf{C}_M = \sigma_m^2 \mathbf{I}, \tag{2.7}$$

where **I** is the identity matrix, σ_m^2 the variance of the elements of the *a priori* model vector.

A smoothing solution can be quantified by the second derivative, and hence the n×n matrix is defined by:

$$\mathbf{C}_M^{-1} = \sigma_m^{-2}[\mathbf{D}^\mathbf{T}\mathbf{D}] \quad \text{and} \quad \mathbf{C}_M = \sigma_m^2[\mathbf{D}^\mathbf{T}\mathbf{D}]^{-1}, \tag{2.8}$$

where the n×n matrix **D** is given by:

$$D = \begin{bmatrix} -1 & 1 & & & & \\ & -1 & 1 & & & \\ & & \cdot & \cdot & & \\ & & & \cdot & \cdot & \\ & & & & -1 & 1 \\ & & & & & -1 \end{bmatrix}_{n \times n} .$$

and superscript T denotes transpose of a matrix. The matrix $\mathbf{D}^T\mathbf{D}$ can be interpreted as a weighting factor that enters into the calculation of the length of the model parameter vector **m**.

In practice, the m-element vector $\boldsymbol{\sigma}_\mathbf{d}$ and the n-element vector $\boldsymbol{\sigma}_\mathbf{m}$ are generated based on exponential function (10^x) scale with an equal interval Δx to form a 2-dimensional space in which the best pair of (σ_d, σ_m) is sought for the best data fitting. For example, given $\Delta x = 0.1$, we may have x = -2.0, -2.1, -2.2, …, -4.0 with 21 values of x, which produces a 21-element vector = $10^{-2.0}$, $10^{-2.1}$, $10^{-2.2}$, …, $10^{-4.0}$.

2.3.4 Implementation of the inversion algorithm

The original starting model (rough estimates of velocities) needs first to be smoothed to generate a more manageable starting model for data fitting. Therefore I place some measure of smoothness on the model parameters, and hence have two routines for implementation of the nonlinear inversion algorithm;

- Routine 1 for model parameter smoothing with diagonal matrices C_D and C_M,
- Routine 2 for data fitting with a diagonal matrix C_D and weighting matrix C_M.

To complete the whole inversion algorithm, I develop a two-step procedure:

- First, smooth the starting model parameters (velocities). For this I search for the best pair of (σ_d, σ_m) in a given 2-demensional space for the minimization of the cost function using routine 1 with the original starting model (rough estimates of P-wave velocities we have). While the best pair of (σ_d, σ_m) is sought I also obtain a smoothed model parameters (velocities) corresponding the best pair, and determine optimal values of variances σ_d^2 and σ_m^2.
- Second, using the smoothed model parameters as a new starting model and diagonal matrices C_D and C_M produced by the obtained best pair of (σ_d, σ_m), I run routine 2 for data fitting, and finally obtain the best estimates of model parameters (velocities) when the best data fitting takes place.

The first step is time-consuming because we are seeking (σ_d, σ_m) in a relatively large sample space, but the second step is very fast.

2.3.4.1 The first step: searching for the best pair of (σ_d, σ_m) and a smooth model

Given a pair of (σ_d, σ_m), routine 1 iteratively calculates the cost function and, if convergence exists, finally determine a local minimum of the cost function value in less than 6 iterations. Obviously different values of (σ_d, σ_m) will generate different final cost function values. If we keep σ_m the same and only change σ_d in orders of magnitude (namely, increase 10, 100, 1000 times, etc.), the cost function changes with same order of magnitude accordingly, then the ratio of final cost function to the initial cost function retains the same magnitude. Therefore, we choose the final cost function to original cost function ratio as a standardized cost function to compare the results with different pairs of

(σ_d, σ_m). To obtain the best estimates of model parameters (here the desired velocity vector), we need first to search for the best pair of (σ_d, σ_m) which minimizes the cost function in a given (σ_d, σ_m) sample space using routine 1 for model parameter smoothing. Notice that for the model smoothing case, the best pair of (σ_d, σ_m) obtained by routine 1 does not produce the best data fitting as a whole but generates the best model smoothness. However, the best pair of (σ_d, σ_m) is also the best one for the next step, i.e., data fitting. Figures 2.3 and 2.4 show the cost function (normalized) as a function of σ_d and σ_m and the pair of (σ_d, σ_m) that minimize the cost function.

For the given data set at site 1039, I used a vector $\boldsymbol{\sigma_d} = [10^x;\ x=-1.5, -1.6, -1.7, \ldots, -4.0\ ]$ and a vector $\boldsymbol{\sigma_m}$, $= [10^x;\ x=-2.0, -2.1, -2.3, \ldots, -4.5]$ to form a 26×26 matrix of (σ_d, σ_m) sample space. By searching for the best pair of (σ_d, σ_m) in the given sample space, I get the best values: $\sigma_d = 10^{-2.7} = 1.995262\text{E-}3$ and $\sigma_m = 10^{-2.1} = 7.943284\text{E-}4$ (Fig. 2.3).

For the given data set at site 1040, I produce a series $[10^x;\ x=-1.5, -1.6, -1.7, \ldots, -4.0]$ for both vectors $\boldsymbol{\sigma_d}$ and $\boldsymbol{\sigma_m}$, and also form a 26×26 matrix of (σ_d, σ_m) sample space. By searching for the best pair of (σ_d, σ_m) in the given space, I get the best values: $\sigma_d = 10^{-2.3} = 5.011873\text{E-}3$ and $\sigma_m = 10^{-3.9} = 1.2589252\text{E-}4$ (Fig. 2.4).

However, the given sample space, n×n (here 26×26) matrix, is fairly large and hence computation is time-consuming. Fortunately, Figs. 2.3 and 2.4 demonstrate an excellent relationship between σ_d and σ_m and show that there always is at least one low area of value of the cost function between the two straight lines in $\sigma_d\sigma_m$ plane:

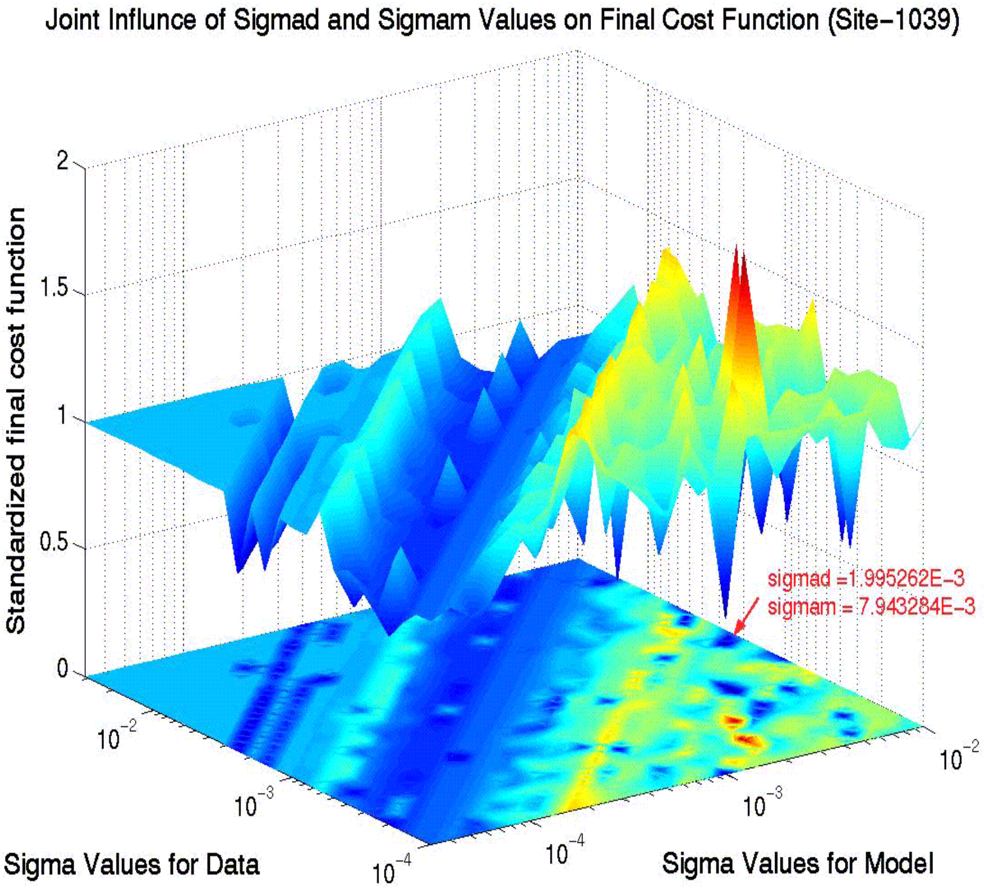

Fig.2.3. Joint influence of σ_d (standard deviation of the elements of data vector) and σ_m (standard deviation of the element of model parameter vector) on final cost function for Site 1039. The upper is surface plotted, and the lower is contoured. Here the cost function is shown by standardization, a ratio of final cost function to initial cost function. The minimum cost function is found when σ_d =1.995262E-3 and σ_m = 7.943284E-4. The area of low cost function values lies between lines $\log_{10}\sigma_d = \log_{10}\sigma_m + 0.5$ and $\log_{10}\sigma_d = \log_{10}\sigma_m + 1.2$ and along line $\log_{10}\sigma_d = \log_{10}\sigma_m + 2.0$.

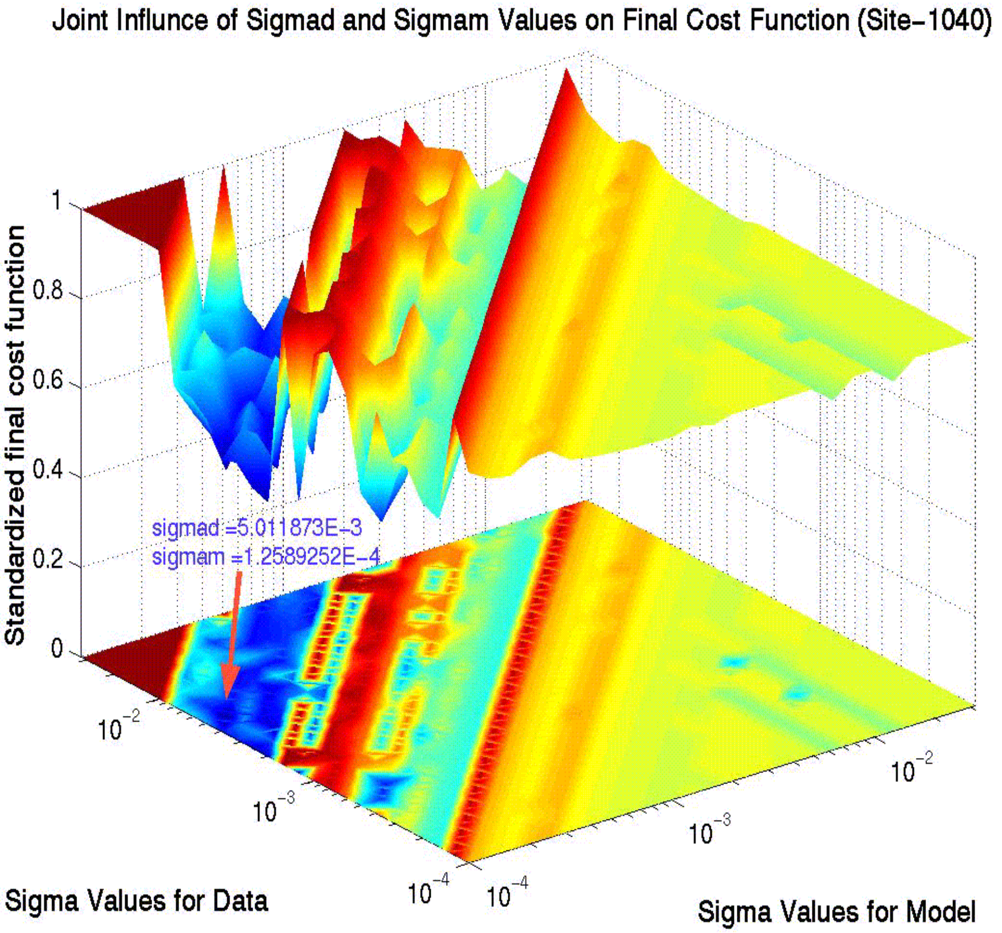

Fig. 2.4. Joint influence of σ_d (standard deviation of the elements of data vector) and σ_m (standard deviation of the element of model parameter vector) on final cost function for Site 1040. The upper is surface plotted, and the lower is contoured. Here the cost function is shown by standardization, a ratio of final cost function to initial cost function. The minimum cost function is found when σ_d =5.011873E-3 and σ_m = 1.2589252E-4. The area of low cost function values lies between lines $\log_{10}\sigma_d = \log_{10}\sigma_m + 1.2$ and $\log_{10}\sigma_d = \log_{10}\sigma_m + 1.9$.

- At site-1039, the area lies between the lines $\log_{10}\sigma_d = \log_{10}\sigma_m + 0.5$ and $\log_{10}\sigma_d = \log_{10}\sigma_m + 1.2$. In addition, there are also low cost function values along the line $\log_{10}\sigma_d = \log_{10}\sigma_m + 2.0$.
- At site-1040, the area of low values of the cost function lies between the lines $\log_{10}\sigma_d = \log_{10}\sigma_m + 1.2$ and $\log_{10}\sigma_d = \log_{10}\sigma_m + 1.9$.

In general, we find that

> *the area of low cost function values lie between the lines* $log_{10}\sigma_d = log_{10}\sigma_m + 0.5$ *and* $log_{10}\sigma_d = log_{10}\sigma_m + 2.0$.

Any cost function value in this area is very close to the minimum cost function, and thus any (σ_d, σ_m) value from within this region is adequate. Given a value of σ_m, we can get a range of σ_d values possibly with low cost function. Therefore, we can reduce a large space (say 26×26) for (σ_d, σ_m) to a reduced vector across the area (say only $\boldsymbol{\sigma_d}$ vector if σ_m is constant). For instance, in our experiments, we can choose:

> $[\boldsymbol{\sigma_d} = 10^x; x=-2.0, -2.1, -2,2, ..., -3.5 \,||\, \boldsymbol{\sigma_m} = 10^{-4.0}]$ *for both sites 1039 and 1040,*

which is a 16-element vector for $\boldsymbol{\sigma_d}$, but a single valued scalar for$\boldsymbol{\sigma_m}$. In this reduced sample space, we can easily find an optimal (σ_d, σ_m) value, and then obtain a final result with good data fitting.

2.3.4.2 The second step: final data fitting and model parameters

After obtaining the best pair of (σ_d, σ_m) with smoothed model parameters, I use the smoothed model as my new starting model and an optimal pair of values of (σ_d, σ_m), and then run routine 2 for data fitting to obtain final model parameters (velocities) and final synthetic data that fit the observed data. In general, the number of iterations used is less than 8. Note that the best pair of (σ_d, σ_m) is sought in a 26×26 matrix of (σ_d, σ_m) sample space, or simply in a vector sample space, at the first step. The inversion results of site 1039 and 1040 are shown in Figs. 2.5 and 2.6 respectively, where (a) shows the initial starting and smoothed models, (b) shows the new starting model (the smoothed models) and the final model, and (c) time response shows observed, starting and final data. From each (c) we can see excellent data fitting.

2.3.4.3 Velocity interpolation and extrapolation

To estimate the velocity profiles away from the drill locations, I interpolate and extrapolate the starting velocities. Density logs are also extended to the selected CDP sites along the MCS Line 20. I also undertake 1-D waveform inversion at each interpolated or extrapolated common depth point (CDP) location along the seismic profile.

Between sites 1043 (CDP 2805) and 1039 (CDP 2930) of the stacked seismic section, we picked 12 CDPs beginning with CDP 2810 and ending with CDP 2920 as the observed seismic data. At the corresponding CDP sites, I linearly interpolated densities and initial rough estimates of velocities following the structure defined by density and velocity functions at sites 1043 and 1039. The wavelet is assumed to be the same along the entire profile. According to our empirical relationships between vectors $\boldsymbol{\sigma}_\mathbf{d}$ and $\boldsymbol{\sigma}_\mathbf{m}$**,** we set up a small sample space, a 16-element vector of [$\boldsymbol{\sigma}_\mathbf{d} = 10^x$; x=-2.0, -2.1, -2,2, …,

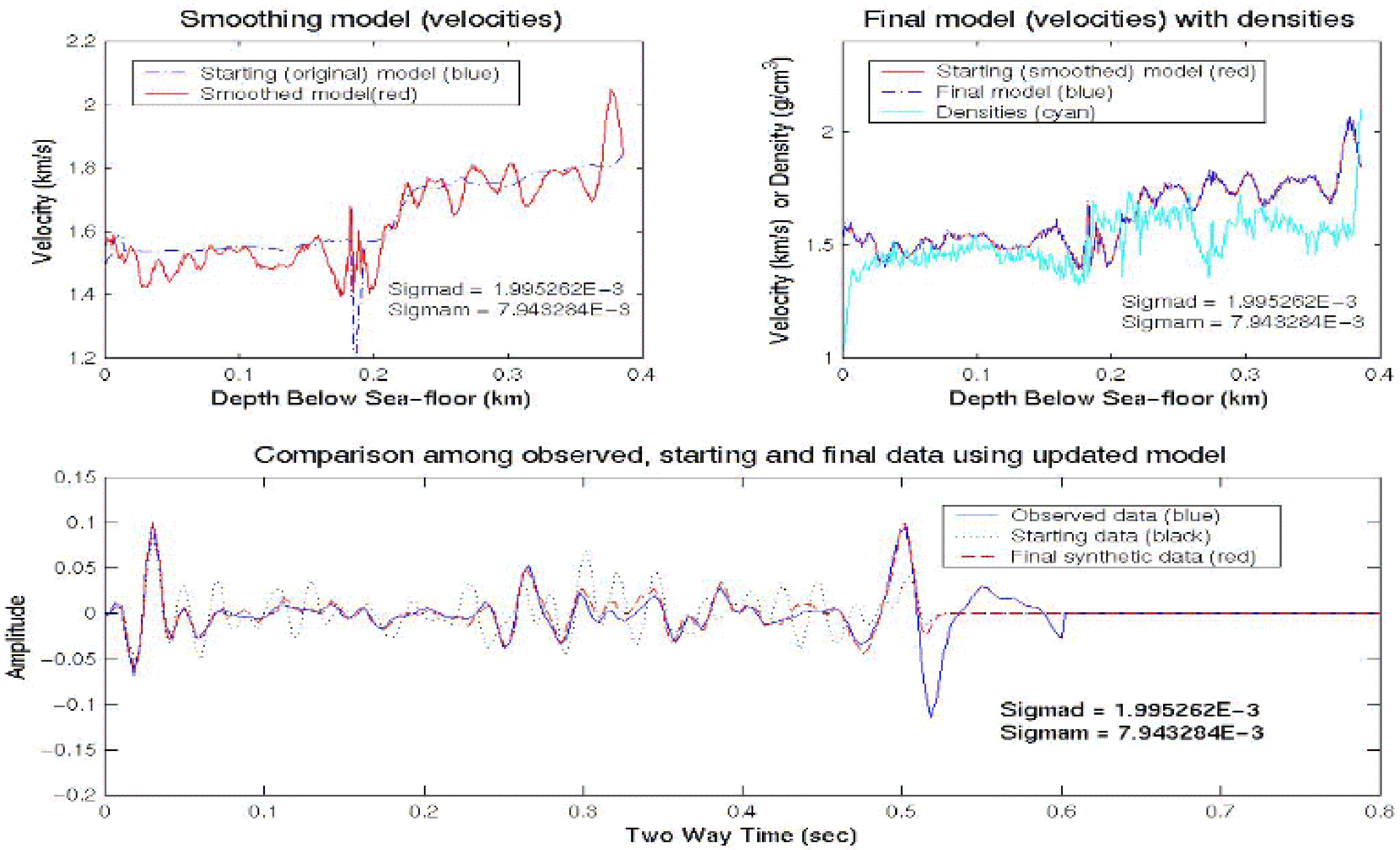

Fig. 2.5 Model smoothing and final inversion results for Site 1039. (1) Smoothing model (velocities) using original starting velocities at the first step of the whole inversion process. The second step of the process, using smoothed model as new starting model and the best pair of σ_d and σ_m generating matrices C_D and C_M produces two results: (2) final model (velocities) being the best of estimates of model, and (3) best data fitting.

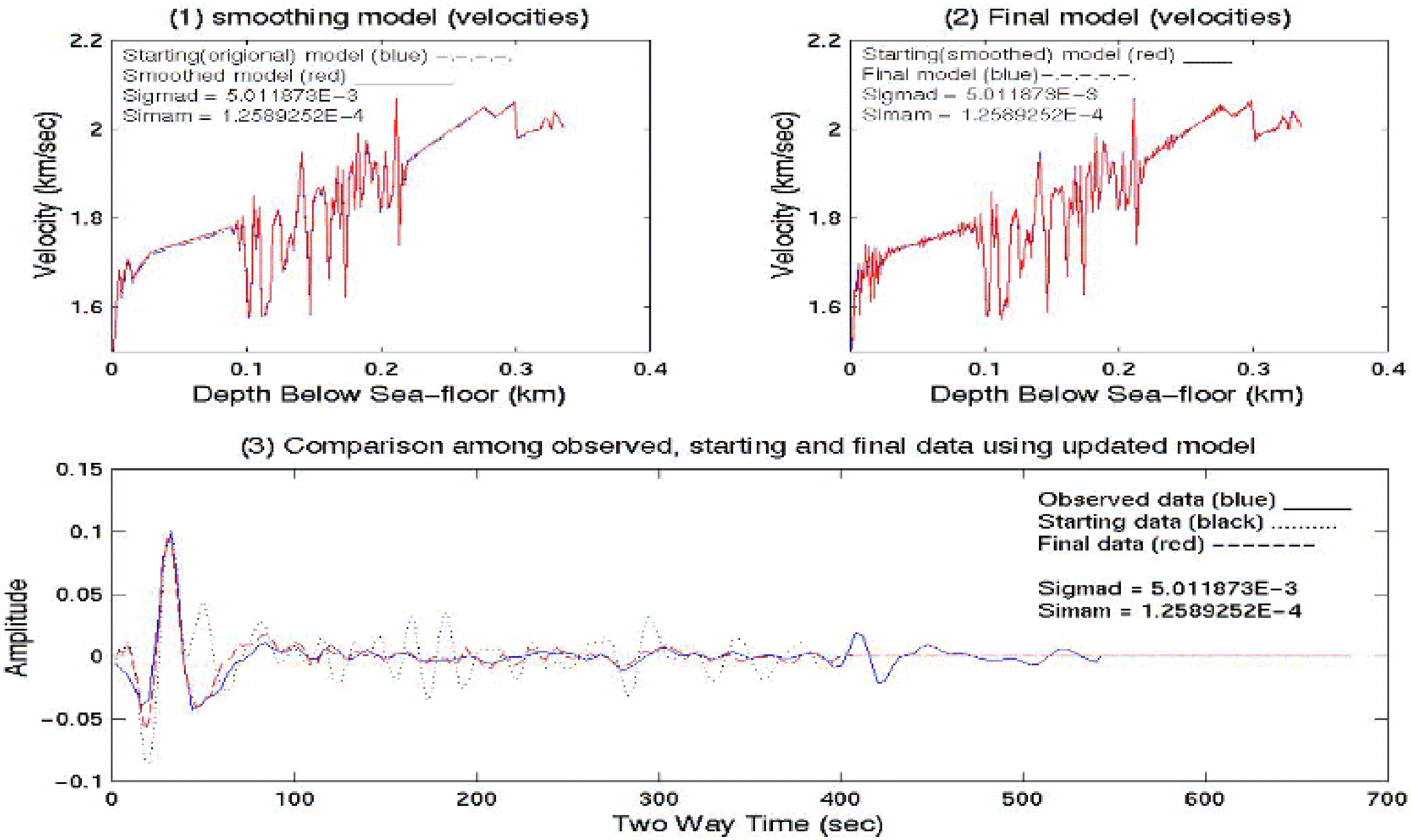

Fig.2.6. Model smoothing and final inversion results for Site 1040. (1) Model (velocities) smooth using original starting velocities at the first step of the whole inversion process. The second step of the process, using smoothed model as new starting model and the best pair of σ_d and σ_m generating matrices C_D and C_M produces two results: (2) final model (velocities) being the best of estimates of model, and (3) best data fitting.

-3.5 || $\sigma_m = 10^{-4.0}$] for all 14 CDP sites, including CDPs 2805 and 2930, to search for the best pair of (σ_d, σ_m) for determining matrices C_D and C_M. After the two steps of inversion for velocity estimates, the final acoustic impedance and velocity estimates of all 14 CDPs are shown in Fig. 2.7(a), where density profiles are also displayed. The corresponding data fit between observed seismic data and the final synthetic calculated from the inversion results is also shown in Fig. 2.7(b). Prominent seismic reflectors representing major stratigraphic boundaries are marked.

Seaward beyond site 1039 (CDP 2930), I picked 5 CDPs (about every 50 CDPs) from the stacked seismic section as the observed seismic data. Density function of each of the 5 CDP sites is viewed as the same as that of site 1039. Using each set of final model parameters (velocities) of a CDP site as the new starting model for next CDP site beginning with site 1039 (CDP 2930), I continuously ran routine 2 to estimate velocities at each CDP site directly by data fitting. The results are shown in Figs. 2.8(a) and 2.8(b) (right 5 CDPs).

Similarly, landward beyond site 1040 (CDP 2740), I picked 14 CDPs (very 50 CDPs) from the seismic section as the observed data. Only the part of densities overlying the decolloment is extended to other CDP sites. I use each set of final model parameters (velocities) of a CDP site as a new starting model for the next CDP beginning with site 1040. Finally, I obtain the estimated velocity profiles shown in Fig. 2.8(a) and corresponding data fittings are shown in Fig. 2.8(b) (left 14 CDPs).

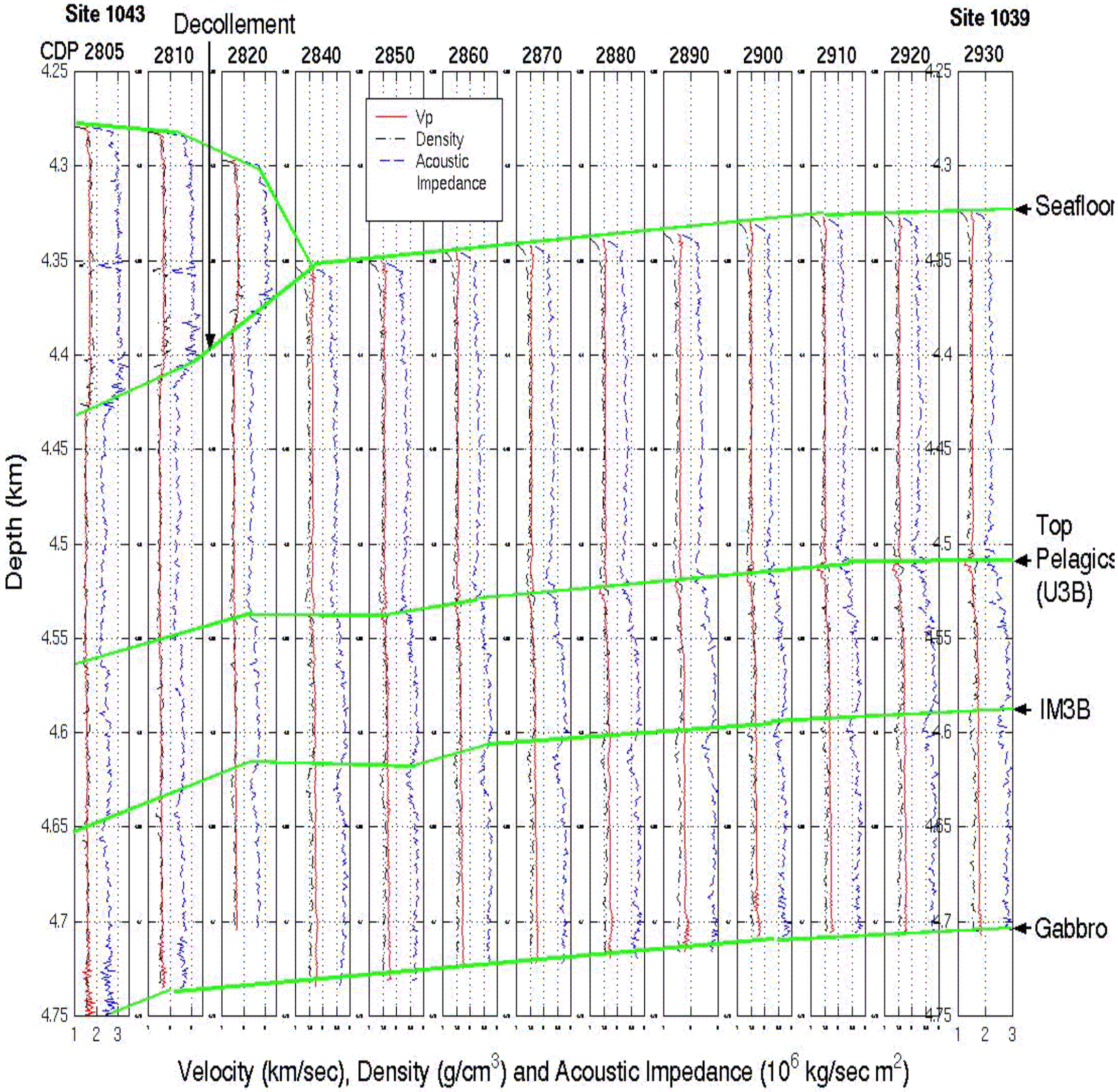

2.7a

(To be continued)

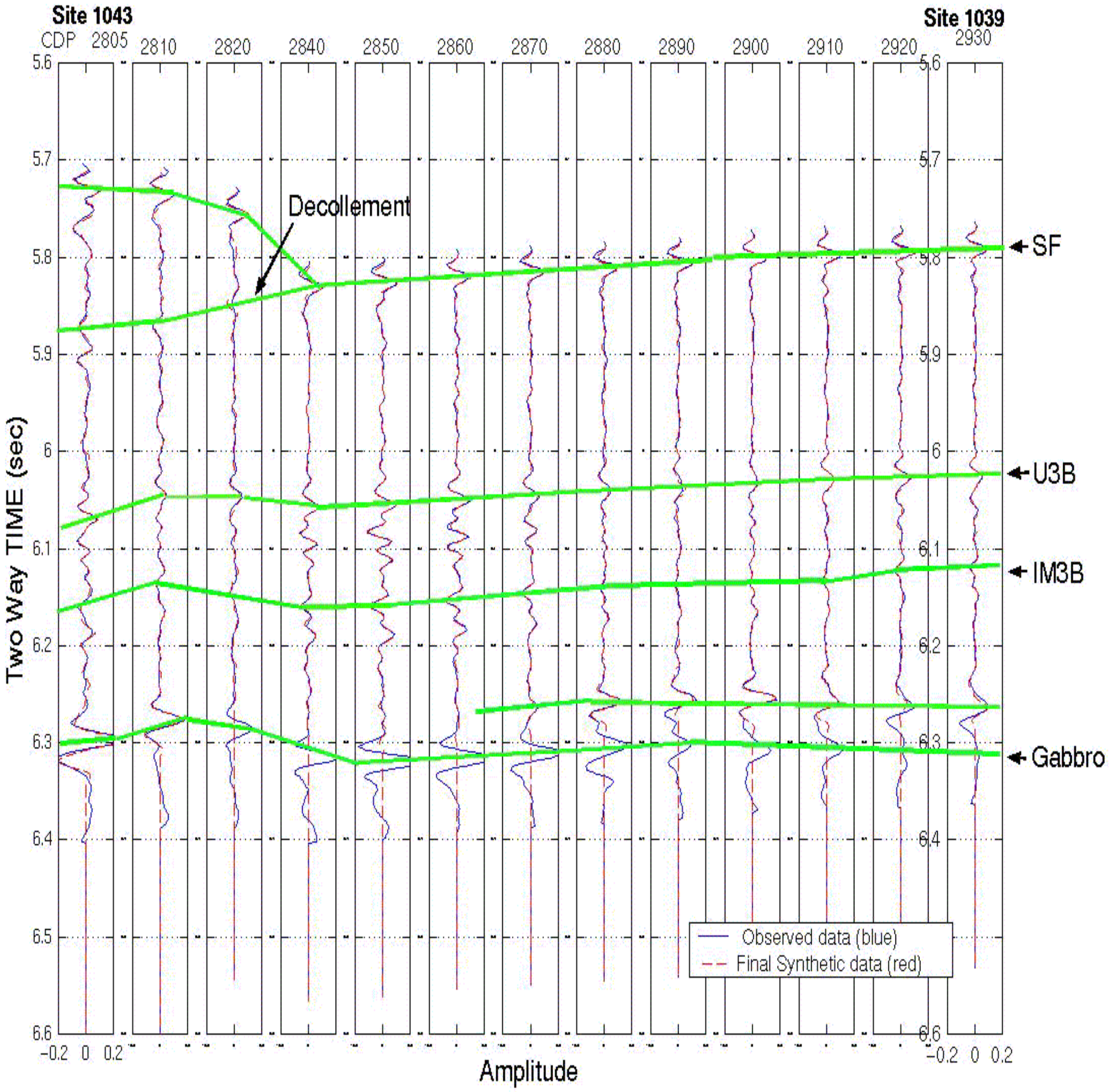

2.7b

Fig. 2.7. Estimated velocity, density and acoustic impedance functions and corresponding data fitting between sites 1043 and 1039 with geological interpretation. (a) The inverted velocity, density and acoustic impedance profiles with marks of major stratigraphic surfaces. (b) The seismic data fitting on seismic section consisting of 13 picked CDPs, showing marks of prominent reflectors. See the text in detail.

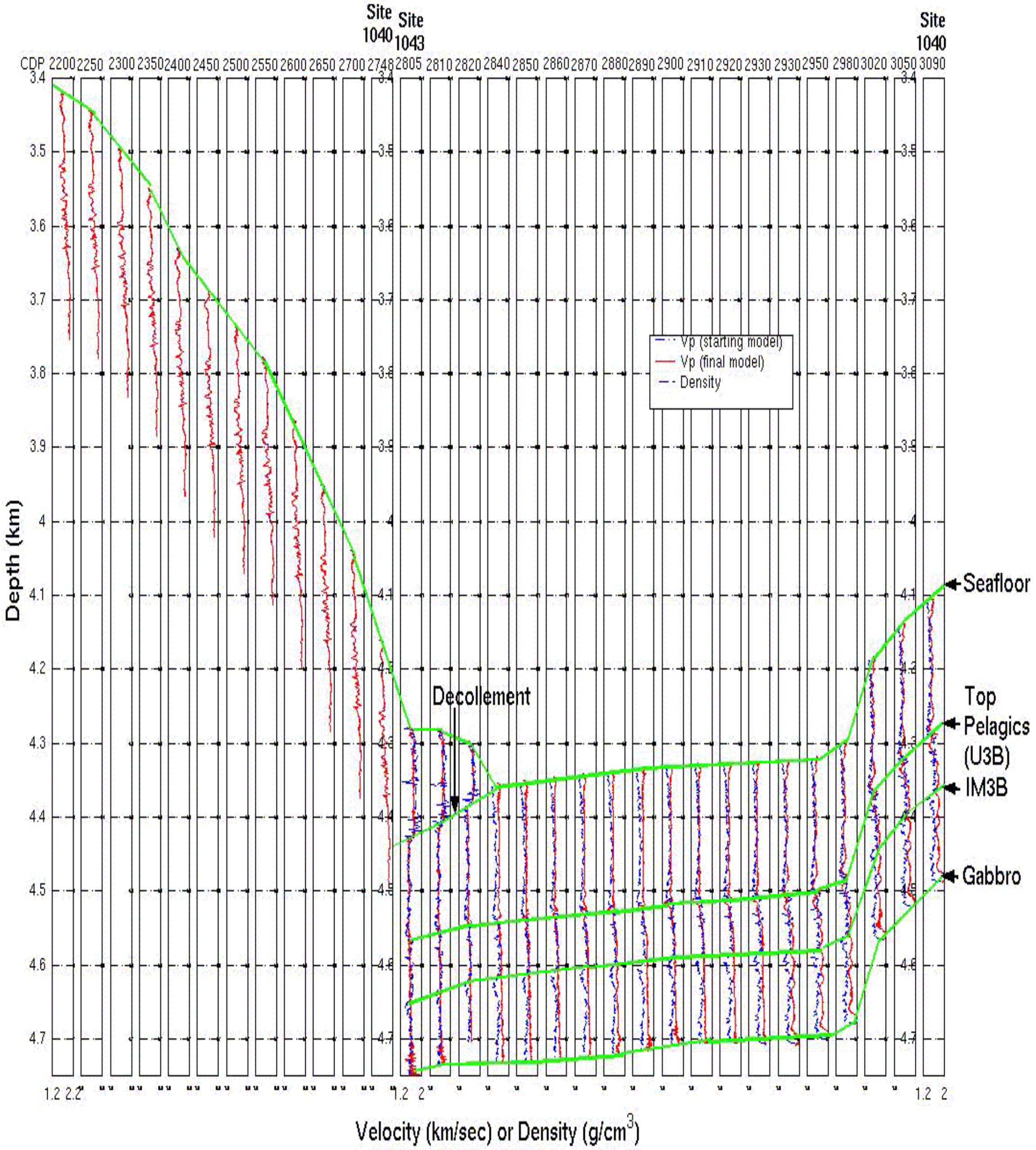

2.8a

(To be continued)

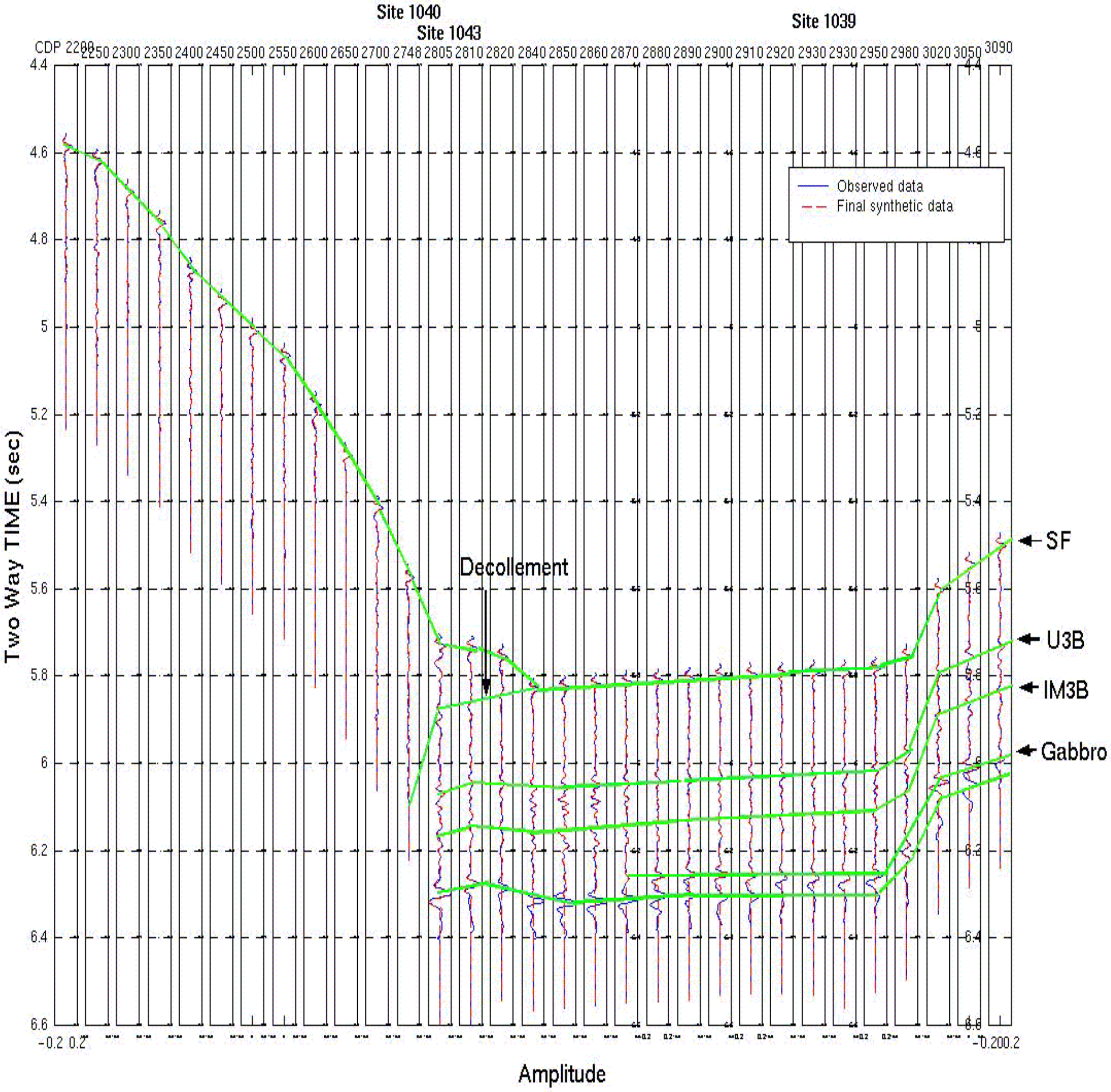

2.8b

Fig. 2.8. Estimated velocity and density functions and corresponding data fitting between sites 1043 and 1039 and extrapolation of velocities beyond the two sites. Geological interpretation is included. (a) The inverted velocity and density profiles with marks of major stratigraphic surfaces. (b) The seismic data fitting on seismic section consisting of picked CDPs, showing marks of prominent reflectors. See the text in detail. Note that CDPs picked at different interval for three segments, beyond site 1043 landward, between sites 1043 and 1039, and beyond site 1039 seaward. See text in detail.

2.3.5 Geological interpretation

Because the stratigraphy of the subducting Cocos Plate is quite consistent in the study area (Kimura et al., 1997, McIntosh and Sen, 2000), I can identify prominent reflectors representing major stratigraphic boundaries on the seismic sections consisting of picked CDPs (Figs. 2.7b and 2.8b) and the profiles of densities and the inverted impedances and velocities (Figs. 2.7a and 2.8a) following the stratigraphic identifiers of Kimura et al. (1997). Beginning with the trench axis toward land, the decollement is well marked by a phase-reversed (relative to the seafloor) reflection on the seismic section and by significant decreases both in densities and calculated velocities, which are shown by CDPs 2805, 2810 and 2830 in Figs. 2.7 and 2.8. Landward above the decollement, no major stratigraphic units are marked due to un-availability of detailed density and velocity data. On the subducting Cocos Plate, the first major reflector below the seafloor represents the boundary between hemipelagic and pelagic and is marked by a major peak in amplitude at about 6.05 s near trench axis on the seismic section and by increase in both densities and in velocities, thus an increase in impedances. Notice that near the top of pelagic I derived a low velocity layer. In general, velocities of the pelagic sediments increase with depth down to the basement. The densities of these pelagic sediments, however, demonstrate a significant drop and a corresponding decrease in acoustic impedance around 0.27 km below the seafloor, which produces a major trough in the seismic section. The largest reflection peak around 6.3 seconds in the seismic section indicates the top of basement Gabbro. This boundary is shown by both density log recorded by LWD at Site 1039 (i.e., CDP 2930) and by velocity profile in Figs. 2.7 and 2.8.

2.4 Summary

The best estimates of model parameters using nonlinear least-squares techniques can be obtained by minimizing a cost function which is a function of the data covariance matrix C_D and the a priori model covariance matrix C_M. Based on a least-squares approach with the preconditioned conjugate gradient for nonlinear inversion problem, I have developed effective methods to determine the two matrices for use in the 1-D waveform inversion of post-stack data.

To determine the two matrices for obtaining the best estimates of the model parameters with the best data fittings, I need to place some necessary prior information onto the data and model parameters. I assume that the observed data are uncorrelated, and both the matrix C_D and the matrix C_M are diagonal; thus the matrix C_D is defined only by the standard deviation σ_d of the elements of data vector, and the matrix C_M is defined only by the standard deviation σ_m of the elements of model vector. I also consider the model smoothness issue for real stacked seismic data. In this case, a first derivative weighting factor is used to define the matrix $\mathbf{C}_M^{-1}$. Thus, the cost function becomes a function of σ_d and σ_m. Once the best pair of values of σ_d and σ_m, which minimizes the cost function, is mapped in a given 2-dimensional sample space, the pair of values of σ_d and σ_m corresponding to low (minimum) of the cost function is our optimal choice.

My inversion process includes two steps: a search for optimal (σ_d, σ_m) values followed by optimal data fitting. Searching for the optimal pair of (σ_d, σ_m) minimizing the cost function in a given 2-dimensioanl sample space is thecomputationally time-consuming part of my inversion. Fortunately, the experiment demonstrates that there is always an area on the $\sigma_d\sigma_m$ plane in which the low cost function values lie, and hence a wide 2-dimensioanl search space can be reduced to a much smaller region. This will lead to the easy application of this inversion method. Note that the best pair of (σ_d, σ_m) does not generate best data fitting but the best smoothed model for the first step. However, the best pair of (σ_d, σ_m) will be the best one for data fitting at the second step. Using the smoothed model as new starting model, I can finally obtain the best estimates of model parameters (velocities) with the best data fitting.

In summary, I have developed an inversion method with the following 2-step procedure:

- first step — model smoothing
    - Apply inversion for several possible values of (σ_d, σ_m) with smooth starting model for a fixed number of iterations.
    - Error surface as a function of (σ_d, σ_m) is examined and the region of the error surface where it reaches very small value is chosen to be optimal (σ_d, σ_m).
    - Any value of (σ_d, σ_m) from within that region generally produces good data fit along with realistic smooth model.
- Second step — data fitting

- Use the optimal (σ_d, σ_m) to determine matrices C_D and C_M, and use the resulting model from the first step as the starting model;
- Apply inversion with no smoothness constraint to get final model and corresponding data fit. This further improves data fitting and includes realistic high frequency variations in the final model.

This experiment shows that almost every identified reflector of seismic data is matched very well by the final synthetic data, which means that my estimates of velocities are internally consistent. Density logs were extended to the selected CDP sites along the MCS Line 20 by interpolation and extrapolation, and combined with selected MCS CDP traces to estimate velocity profiles of the entire section. Combination of density and calculated velocity profiles can allow the identification of major stratigraphic boundaries such as the surfaces of top pelagic and Gabrro.

Chapter 3: Analysis of OBS and MCS data offshore Oregon – estimation of elastic properties of gas hydrates

3.1 Introduction

Since their natural occurrences were reported in the early 1970s, gas hydrates have become a new focus of international research. This is because gas hydrates may represent: (1) major future energy sources, (2) a potential source of an important greenhouse gas, and (3) a possible cause of submarine geohazard (Kvenvolden, 1993). Natural gas hydrates occur worldwide in marine, permafrost, and lake environments. Crucial issues concerning gas hydrates, such as their origin and potential gas recovery, are still poorly understood. A 3-D multi-channel and Ocean-Bottom Seismometer (OBS) survey was carried out in the Central Oregon Continental Margin to address some of these fundamental issues. In this chapter, I report results from analysis of some of these seismic data sets. In particular, I derive estimates of *in-situ* elastic properties of gas hydrates and define the distribution of gas hydrates under the southern summit of the Hydrate Ridge using ocean-bottom seismometers (OBS) and multi-channel seismic (MCS) data.

3.1.1 Gas hydrates

Gas hydrates are ice-like crystalline substances composed of water and gas in which a solid-water lattice accommodates guest gas molecules (largely methane) in a cage-like structure, also called clathrate (Sloan, 1990). Without chemical bonds to water molecules, the gas molecules are free to move about within the cages (one in each cage) even though they are securely trapped inside (McIver, 1982). A significant fraction of the cavities must be occupied with gas molecules to ensure stability of the hydrates.

Three clathrate structures are known to occur in natural environments (Sloan, 1997). In structure I (Fig. 3.1), the most common form of clathrates in natural settings, the cages are arranged in body-centered packing and are large enough to include methane and ethane. In structure II, diamond packing is present, resulting in some cages being large enough to include not only methane and ethane but also larger gas molecules such as propane and isobutane. Structure H is of the hexagonal space.

The maximum amount of methane that can occur in a methane hydrate is fixed by the clathrate geometry. In a fully saturated structure I methane hydrate, one molecule of methane is present for every $5\frac{3}{4}$ molecules of water, which means that 1 m^3 of methane hydrate can contain up to 164 m^3 of methane gas at standard P-T conditions.

3.1.2 Formation of gas hydrates

The formation and occurrence of natural gas hydrates need appropriate thermodynamic stability conditions for methane-hydrate and adequate supplies of gas (mainly methane) and water. The primary factors affecting the stability of natural gas hydrates are temperature and pressure, and the secondary factors include gas chemistry, pore fluid salinity, and the grain size of the host sedimentary material. The factors

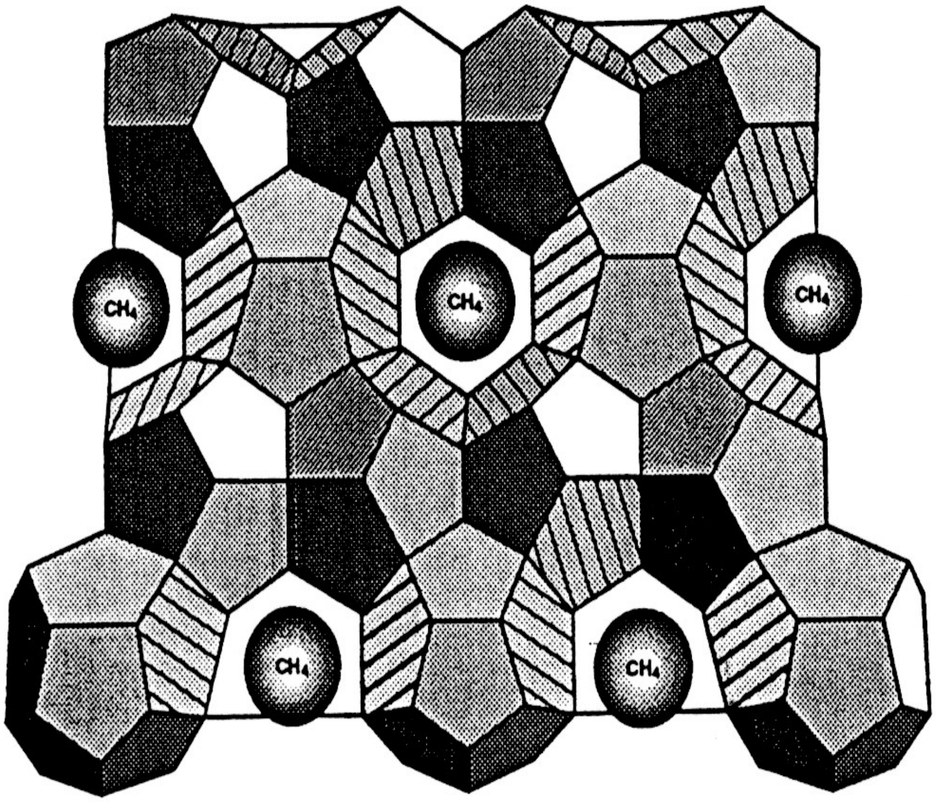

Fig. 3.1. Gas hydrate. In the structure I Methane hydrate the rigid cages are composed of hydrogen-bonded water molecules, and each cage contains a methane molecule. (Modified from Hitchon, 1974)

affecting the supply of gas and water include the availability of gas and water, and gas and water migration pathways in the stratigraphic section (Collett, 1995).

3.1.2.1 Appropriate P-T conditions for methane-hydrate stability

The pressure-temperature stability condition for methane hydrate is defined by a three-phase (methane-hydrate-water) equilibrium relation (Kvenvolden, 1988, 1993; Sloan, 1998; Buffett, 2000), the so-called the phase boundary, which depends both on gas composition and pore fluid salinity (e.g., Hyndman et al., 1992; Kastner et al., 1995; Dickens and Quinby-Hunt, 1997). This particular equilibrium state occurs at temperature $T_3(P)$, which is solely a function of pressure P, usually expressed as an equivalent depth. Methane hydrate is stable when the temperature is less than or equal to $T_3(P)$ at a given depth. Gas hydrates most commonly occur in deep oceanic sediments or in areas of thick permafrost where appropriate P-T conditions for methane-hydrate stability exist.

In continental permafrost, the zone of methane hydrate stability occurs between two intersections of the temperature profiles with the temperature for three-phase equilibrium (Fig. 3.2a). Below the base of the clathrate stability zone, liquid water and free methane gas are anticipated. In marine sediments along deep continental margins, the pressure-temperature condition at the seafloor is available to stabilize methane hydrates. Therefore the zone of methane hydrate stability occurs between the seafloor and the intersection of the temperature profile with the temperature for three-phase equilibrium if the abundance of gas is sufficient (Fig. 3.2b).

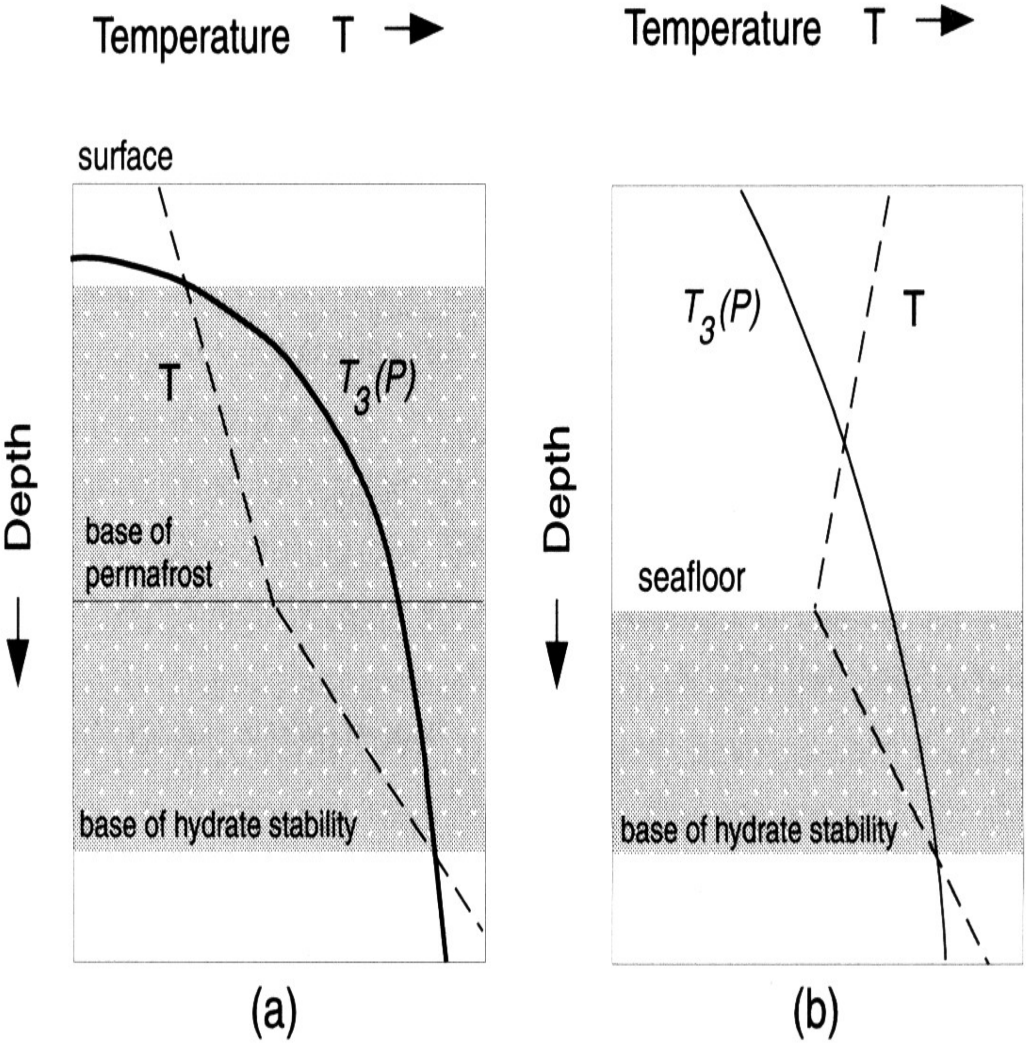

Fig. 3.2. A schematic profile of temperature T in (a) continental permafrost, and (b) marine sediments. Hydrate stability in the sediments (shaded region) is limited to depths where $T<T3$(P). $T3(P)$ defines the temperature of three-phase equilibrium between gas, hydrate and seawater at hydrostatic pressure P proportional to depth. (After Buffett, 2000)

In the shallower sediments, clathrate coexists with seawater in a two-phase equilibrium, whereas at greater depths below the base of the stability zone, we expect to find seawater in equilibrium with gas bubbles. An increase in methane content of gas mixture (methane, ethane and propane) will decrease $T_3(P)$ at a given depth, and hence shift the methane-hydrate-water curve leftward and reduce the thickness of the gas hydrate stability zone (Fig. 3.3) (Holder et al., 1987). Salt, such as NaCl, when added to a gas hydrate system, lowers the temperature at which gas hydrates form. Therefore increase in pore-water salinity would shift the gas hydrate stability curves to the left and reduce the thickness of the gas hydrate stability zone (Collett, 2002).

3.1.2.2 Adequate supplies of gas (primarily methane) and water

The supply of large quantities of hydrocarbon gas is an important factor controlling the formation and distribution of natural gas hydrates (Kvenvolden, 1988; Collett, 1993). Most naturally occurring gas hydrates are characterized by two crystal structures (structure I and structure II). The ideal gas/water ratio (by number of molecules) of structure I gas hydrate is 8/46, whereas the ideal gas/water ratio of structure II gas hydrate is 24/136. These high gas and water concentrations demonstrate that the formation of significant gas hydrate accumulations requires a large source of both gas and water. Additional factors controlling the supply of gas and water are geologic controls, such as rock permeability and the faults, on fluid migration paths.

The methane is considered to be mainly microbial in origin and partly thermogenic. Biogenic methane may be formed within the hydrate stability zones

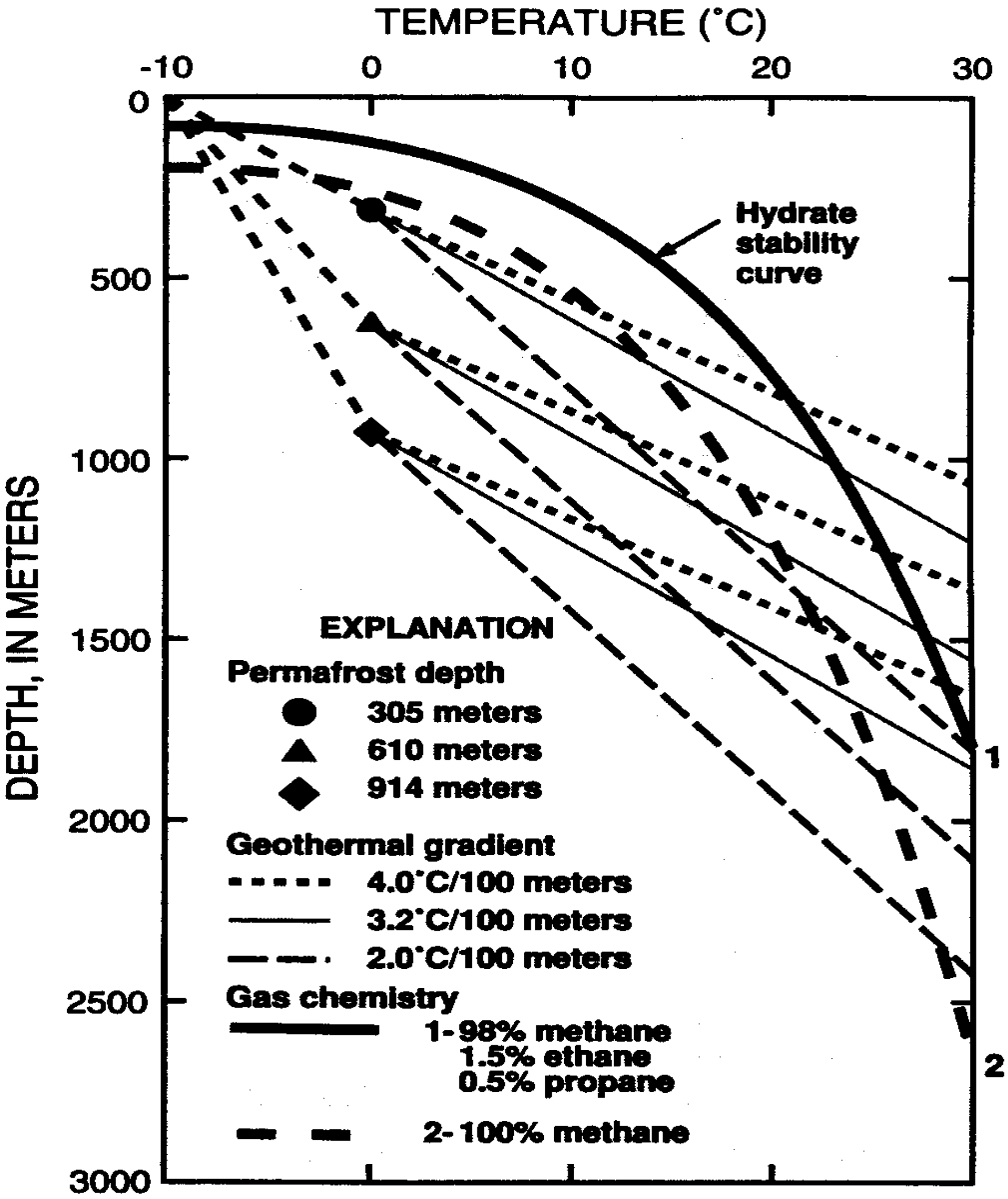

Fig. 3.3. Graph showing the depth-temperature zone in which gas hydrates are stable in a permafrost region (assuming a 9.795 kPa/m pore-pressure gradient) (modified from Holder et al., 1987).

(Claypool and Kaplan, 1974), but more commonly it may be formed below the stability zones, with subsequent upward migration of dissolved methane in rising pore fluids and extraction of methane as pore fluids enter the hydrate stability zone (Hyndman and Davis, 1992,). Thermogenic methane may be formed at greater depths, followed by migration into the hydrate stability zone (Kvenvolden and McDonald, 1985). Because layers of hydrated sediments with a low permeability could act as gas traps, free gas may be accumulated at and below the base of the stability zone.

Hyndman and Davis (1992) developed a model for a positive continental margin in which hydrate is formed through removal of methane from upward-migrating pore fluids as they pass into the hydrate stability field. The overall accretionary process results in rapid shortening and tectonic thickening of the wedge and the sediments are transported to greater depth with only little porosity loss. The resulting underconsolidated section re-establishes an equilibrium porosity-depth relation through consolidation and fluid expulsion. Fluid expulsion rates that reach about 1 mm/year appear sufficient to carry enough methane upward to form the observed hydrate saturation over a thickness of about 100m.

3.1.3. Physical properties of gas hydrate-bearing sediments

The dominant effect of gas hydrate on the elastic properties of gas hydrate-bearing sediments is as a pore-filling constituent. The presence of gas hydrate changes the physical properties of sediment by replacing pore-space water and/or gas with a solid, thereby reducing the effective pore space and permeability, and significantly increasing the elastic velocity. Compared to pore-filling fluids such as water, gas hydrates have relatively high elastic velocities (both P- and S- wave velocities) and hence increase the velocity of the gas hydrate-bearing sediments (Stoll, 1974; Tucholke et al., 1977). Seismic attributes are strongly affected by hydrates in the pore space of sediments. The most readily observable change in sediment physical properties resulting from the formation of gas hydrate is an increase in seismic velocity and a strong seismic reflection at the base of the hydrate zone.

Many velocity models for gas hydrate-bearing sediments, such as Wyllie's time-average equation (e.g., Timur, 1968; Pearson et al., 1983), Wood equation (Wood, 1941) and three-phase weighted equation (Lee et al., 1996), have been developed to describe velocity-porosity relation, which may be used to estimate the velocity of gas hydrate-bearing sediment given rock physical parameters or to estimate the amount of gas hydrate or free gas directly from seismic velocities.

3.1.4 Geochemistry of gas hydrate-bearing sediments

Sources of methane. The methane is considered to be mainly microbial in origin based on geochemical investigations of recovered gas hydrates and of hydrocarbon gases from gas hydrate-bearing sediments. These investigations have shown that the molecular compositions of the hydrocarbon gases and isotopic compositions of methane are consistent with results expected from microbial gas generation processes. In most locations, methane constitutes more than 99% of the hydrocarbon gas mixtures, and the isotopic composition of methane ($\delta^{13}C$) is normally lighter than –60‰ relative to the

Peedee Belemnite (PDB) standard (Claypool and Kvenvolden, 1983). By comparison, thermal conversion of organic matter into hydrocarbon gases at temperatures in excess of 80˚C produces larger quantities of ethane and propane, and the isotopic composition of carbon is relatively heavy. Differences in the composition of the gas supply should be reflected in the composition of the hydrate.

Estimation of the hydrate abundance. Measurements of chemical components and isotopic tracers of pore fluids extracted from sediment cores provide a wealth of information about hydrate occurrences. The most commonly reported observation is the chlorinity of the pore fluid. During gas hydrate formation, water molecules crystallize into a cubic lattice structure, and the hydrate crystals exclude salt ions from the crystal structure. Measurements of chlorinity of samples of gas hydrate water recovered offshore from Guatemala ranged from 0.51 to 3.2‰ (Kvenvolden and McDonald, 1985) and from 1.8 to 8.2‰ for samples from offshore Peru (Kvenvolden and Kastner, 1990). These samples had chlorinity values much less than average seawater chlorinity of 19.8‰. Measurements of the isotopic composition of oxygen in water ($\delta^{18}O$ relative to Standard Mean Ocean Water) provide another means of estimating the hydrate abundance. Oxygen isotopic fractionation of pore water apparently takes place during gas hydrate formation, leading to ^{18}O enrichment with depth in pore fluids recovered after gas hydrate dissociation.

3.1.5 Seismic signature in the continental margin: Bottom Simulating Reflector (BSR)

On seismic sections from continental margins, gas hydrates can be detected mainly by the occurrence of a bottom-simulating reflector (BSR) which is believed to represent the base of the gas hydrate stability zone, marking the transition between hydrate-bearing sediments above and the presence of free gas or water below the surface (Shipley et al., 1979; Stoll and Bryan, 1979; Kvenvolden and Barnard, 1983, Hyndman and Spence, 1992). This lower boundary of solid gas hydrates is present from ~100 to 1100 m below sea floor (Kvenvolden, 1993). A BSR mimics the relief of the sea floor because the base of the gas hydrate stability zone, controlled primarily by temperature, follows isotherms concordant with the sea-floor bathymetry. Seismic attributes are strongly affected by hydrates in the pore space of sediments. Because pure hydrates have a compressional wave velocity in the range 3.3-3.8 km/s (Whalley, 1980; Sloan, 1990), much higher than normal oceanic sediments in the depth range of the hydrate stability field, the hydrated sediments have an anomalously high compressional and shear wave velocity (Pearson et al., 1983; Lee et al., 1996; Jakoberson et al., 2000). On the contrary, the presence of even a small amount of gas in the fluid-filled pore spaces causes a dramatic decrease in compressional wave velocity (Domenico, 1977). In water-saturated sediments, the presence of either hydrate or small amounts of free gas will lower the density slightly. Thus, large acoustic impedance contrasts between sediments containing gas hydrate above and sediments with free gas below cause the BSR to act as strong seismic reflector with negative polarity.

3.1.6 Gas hydrates of the Oregon continental margin

The continental slope of the Oregon accretionary margin, the southern part of the Cascadia accrettionary margin, is one of the areas of comprehensive studies of submarine gas hydrates in the world, including multichannel seismic surveys and ODP leg 146. A multichannel seismic (MCS) reflection survey on the Oregon continental margin conducted in 1989 (Fig. 3.4a) demonstrates the widespread presence of gas hydrate beneath the middle and lower slope of this accretionary margin (Trehu et al., 1995, 1999). Solid gas hydrates have been obtained on the central Oregon continental margin. At Ocean Drilling Program (ODP) Site 892 drilled at the northern summit of the second ridge, the Hydrate Ridge, in 1992 (Fig. 3.4a), gas hydrate was recovered close to the sediment-water interface at 2-19 m below the seafloor at 670 m water depth (Kastner et al., 1995; Kastner, et al., 1998). Massive gas hydrate was recovered from the seafloor at the southern summit of Hydrate Ridge in 1996 using a large video-guided grab samples (Bohrmann et el., 1998; Suess et al., 1999). The latest (July 2002) drilling at the southern summit confirms the presence of subsurface gas hydrates and free gas.

At the Hydrate Ridge area, previous research has documented active venting of fluids and gases and exposures of methane hydrates at the seafloor (Linke et al., 1994; Bohrmann et al., 1998; Torres et al., 1998, Trehu et al., 1999; Suess et al., 2001), which allow an understanding of gas hydrate dynamics.

The regional geological setting provided basic conditions for the generation of gas hydrates in the Cascadia accretionary margin. The oceanic Juan de Fuca plate is

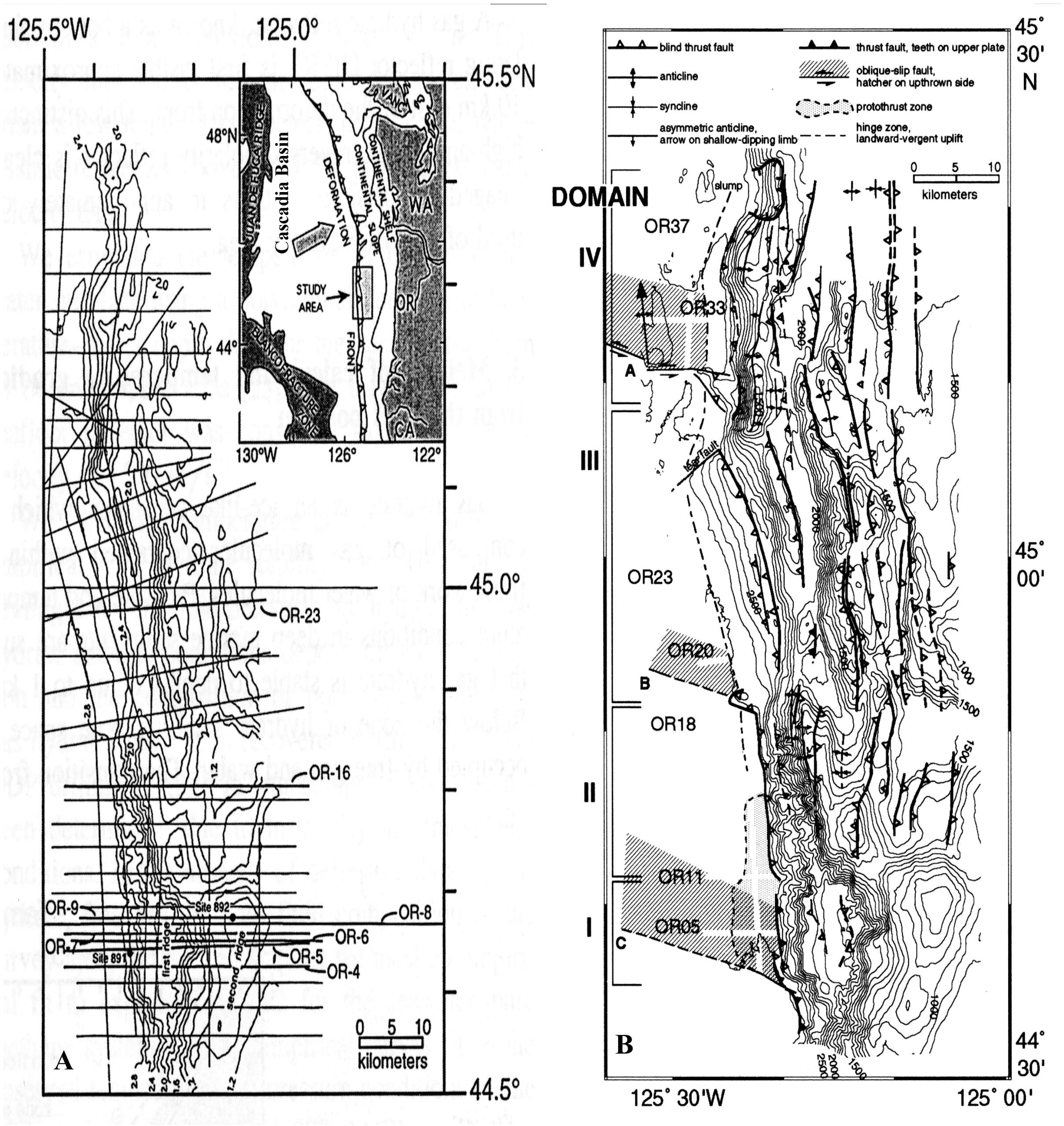

Fig. 3.4. (Left, from Zwart et al., 1996) Bathymetric map of the multi-channel seismic survey area showing location of seismic lines. Contour interval is 0.2 km. Inset shows regional tectonic setting. Black dots are locations of ODP drill sites. (Right, from MacKay, 1995) Structural interpretation of MCS data overlying contoured Sea Beam bathymetry (100-m contour interval).

subducted beneath the continental North America at a rate of about 4.5 cm/yr, which builds a series of subparallel accretionary ridges along the Cascadia margin, offshore northwestern United States and southwestern Canada (Fig. 3.4b,). Most of the sediments on the subducting plate, which contains large volumes of sandy and silty turbidites deposited on the deep seafloor of the Cascadia basin, are scraped off to form anticlinal ridges accreted to the continental margin (MacKay, 1995; Chapman et al., 2002). Terrigenous sediments were deposited rapidly on the continental slope in local basins and troughs formed by folding and faulting of underlying accreted sediments (Westbrook et al., 1994). The currently active accretionary wedge off Oregon is composed of folded thrust slice of Pliocene-Pleistocene age (Westbrook et al., 1994). Upward advection of fluids rich in CH_4 with minor amounts of ethane, which originate in underthrust sediments and ascend along an inclined fault, is probably responsible for the presence of gas hydrate here like in many other active accretionary complexes (Kastner et al., 1998; Trehu et al., 1999). Hydrates are formed through removal of methane from upward-migrating pore fluids as they pass into the hydrate stability field (Riedel et al., 2001).

3.1.7 Objectives

Based on the observation on 1989 multi-channel seismic data that a BSR is ubiquitous beneath the Hydrate Ridge and that the evidence for hydrate and free gas was found, a new seismic survey comprising 3-D multi-channel seismic (MCS) streamer and Ocean Bottom seismometers (OBS) surveys, aimed at imaging the structures controlling the migration of methane-rich fluid and free gas and characterizing the gas hydrates of the southern part of the Hydrate Ridge, was conducted in the Summer of 2000 (Fig. 3.5).

The objectives of my research are as follows:

1) Velocity analysis of Vp and Vs from OBS data,
2) Pre-stack waveform inversion for Vp in τ-p domain from streamer data,
3) Detection of the distribution of gas hydrates and free gas, and
4) Interpretation of the formation of gas hydrates.

3.2 The Central Oregon Continental Margin Experiment

In the summer of 2000, scientists from UTIG (Bangs, Nakamura) and University of Oregon (Trehu) conducted 3-D MCS (towed streamer) and OBS surveys in the Hydrate Ridge and vicinity area of the Oregon continental margin. The map of the survey area and lines are shown in Fig. 3.5. The stated goals of the Oregon continental margin experiment, focusing on the southern summit area of the Hydrate Ridge, were to

(1) image structures controlling the migration of methane-rich fluid and free gas in this high-fluid-flux convergent margin setting,
(2) study the gas-hydrate distribution, and
(3) estimate free gas content of shallow sediments in the area.

A volume of 3-D seismic reflection data, covering a 4×11 km^2 area across the top of southern Hydrate Ridge 10 km south of ODP Site 892, was acquired with the Lamont-Doherty Earth Observatory portable high-resolution seismic acquisition system on board the R/V Thompson. The 3D Survey comprised eighty one 11-km-long profiles spaced 50

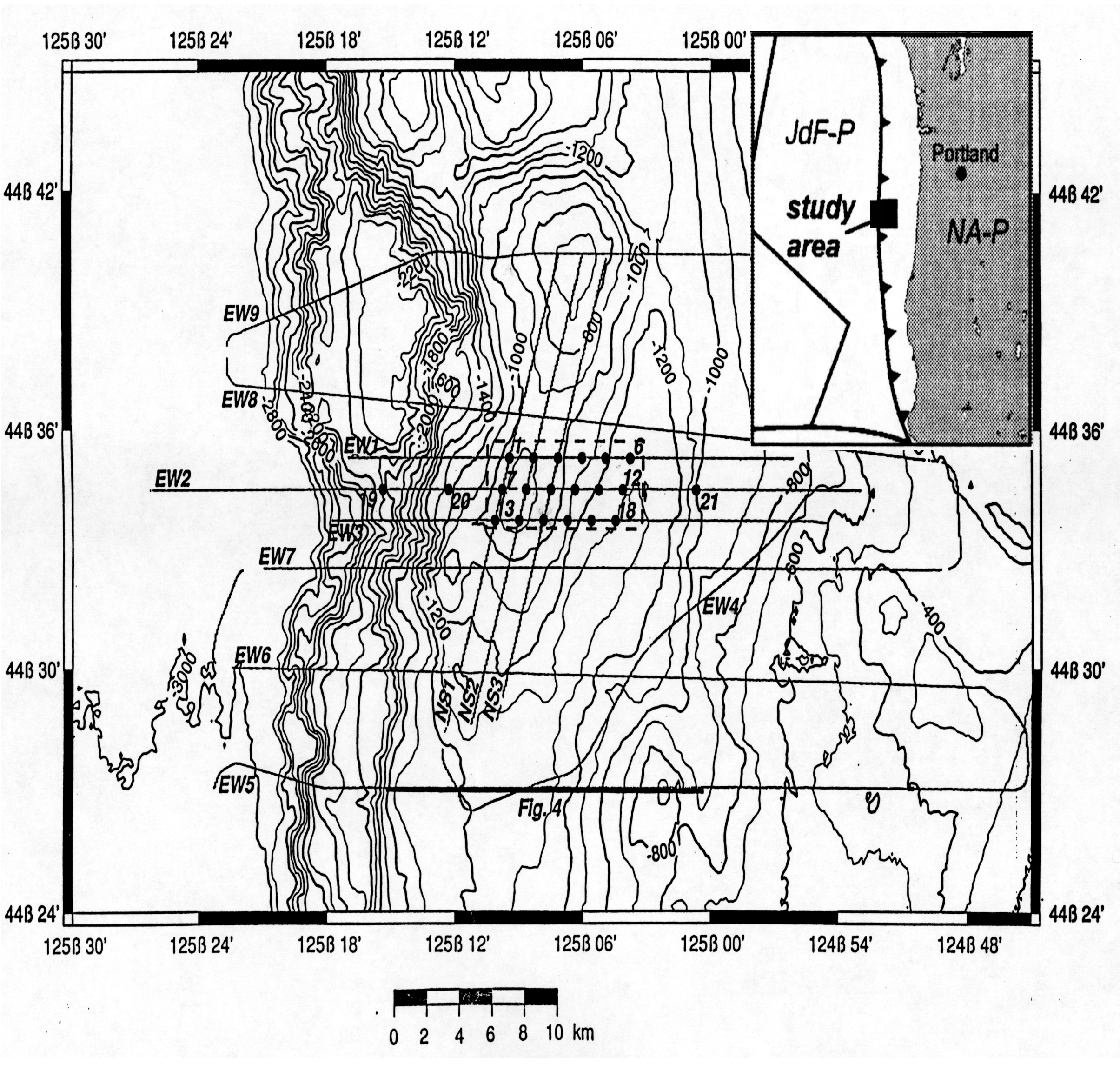

Fig. 3.5. Bathymetric map showing regional lines, OBS locations (numbered dots), and the location of the 3D seismic survey (dashed box). Inset shows regional tectonic setting and location of study area.

m apart, with a shot spacing of 15 m and a record length of 4 seconds. Shots from 2 GI airguns were recorded simultaneously by a 600-m-long 48-channel streamer. The system recorded reflections between 30-200 Hz with a vertical resolution of approximately 5 m. With an array of twenty one 4-component ocean bottom seismometers deployed on the seafloor, the OBS survey was carried out across the Hydrate Ridge to record airgun shots and obtain wide-aperture refraction data.

In a previous seismic survey on the Oregon continental margin, only MCS data were used to identify the presence of gas hydrates and to map their distribution; OBS first arrival data were only used to estimate background velocities for producing a preliminary stacked seismic section (Trehu et al., 1995). In my work, OBS and MCS data obtained from the central Oregon continental margin experiment will be combined to identify main reflecting horizons and estimate physical properties of individual layers, including the character of the hydrates.

3.3 Application of MCS and OBS Data in Detecting Gas Hydrates

Marine multichannel seismic (MCS) technology is one of the principal tools used to image the structures of the subsurface, and Ocean bottom seismometer (OBS) technology can produce more precise estimates of physical properties of individual layers. Since the mid-1970’s MCS technology has been one of major tools for detecting Earth’s shallow structure and evolution. MCS technology uses marine towed streamers as receivers, which are one-component systems, use only hydrophones and record directly only P-waves. This technology was first used for 2-D seismic surveys and recently extended to 3-D seismic survey. 2-D or 3-D MCS datasets allow us to image the subsurface for locating important structures and major stratigraphic sequence, to estimate physical properties of individual layers for identifying lithology, and further to detect hydrocarbons. Currently the high-resolution multichannel seismic surveys have been widely carried out to investigate deep-sea gas hydrates. In isotropic media three parameters describing the earth are required, usually Vp, Vs and density, whose information aids in the discrimination of pore filling fluids and is crucial for hydrocarbon detection. However, only P-wave velocity can be directly obtained while S-wave velocity and density cannot be accurately resolved from MCS data.

In the late-1970's academic institutions began to use the ocean bottom seismometers deployed on seafloor in marine seismic surveys. OBS technology uses four-component (4-C) sensors, each of them is equipped with a single hydrophone (pressure detector) plus a three-component (3-C) geophone (particle velocity detector). Although OBSs record all four components, only the hydrophone and vertical geophone data have been routinely used. Recently the development of ocean-bottom multicomponent recording technology, especially ocean-bottom cable (OBC) technology, can provide high quality P- and S-wave data for hydrocarbon detection. Unlike OBS surveys, where only a sparse set of receivers is used in a typical study, OBC surveys deploy 4-C sensors on the seafloor at dense spatial sampling (typically 25 m) along a cable to record converted waves, also called C waves (Thomsen, 1999). The essence of the newly developed OBS and OBC technologies is recording of converted S-waves, in addition to conventional P-waves, on the seafloor with 4-C sensors. The 3-C geophone records the full three-dimensional ground motion via one vertical component and two orthogonal horizontal components. The main applications of 4-C seismic data by combination of PP and PS data for hydrocarbon exploration include imaging through gas clouds, direct hydrocarbon detection, lithology and fluid prediction, and estimation of fracture parameters (Tatham, 2002). In the case of OBS data, PS surveys can provide more detailed reflection information and more accurate S-wave velocity profiles, but it is difficult to obtain detailed images of the structure of sub-sea because of sparse coverage.

In general, MCS data can provide the images of the sub-sea structure, and P-wave velocity files; and OBS data can be used to derive high-resolution P-wave and S-wave velocity profiles at sparse locations. Although OBSs record all four components (pressure and vertical, radial and transverse grand motion), only the hydrophone and vertical geophone data have been routinely used. The combined use of P- and S-wave OBS data can generate better estimates of P- and S-wave velocities. Therefore, the combination of MCS survey and OBS survey in the Hydrate Ridge area will help to (1) detect the structures of the subsurface, (2) map the distribution of the gas hydrates, (3) estimate physical properties of gas hydrate-bearing sediments, and (4) interpret the formation of gas hydrates.

3.4 Processing of OBS Data

The initial step of data analysis includes generation of a structural image by migration of the MCS data. The objectives of processing the OBS data include: (1) correlating OBS data with MCS data, (2) obtaining the true amplitudes of the reflected

PP-, PS- and PSS-waves, and (3) estimating Vp and Vs from the seismic data. The flowchart for the OBS data processing is shown in (Fig. 3.6). In my study, only the hydrophone and radial component geophone data are processed. To suppress noise, such as source generated bubble pulses, a band-pass filter is applied to the common receiver gathers of both hydrophone and radial component geophone data. The bandwidth of the filter, chosen for displaying the main reflectors by emphasizing the useful signals, is usually 15 to 75 Hz. Fig. 3.7 shows a comparison between the raw data and filtered data for hydrophone component of OBS102ns, along with its corresponding spectrum analyses, and Fig. 3.8 shows the radial component geophone gather of OBS102ns without and with filter. After low frequencies were removed, major reflectors are clearly visible. Because the original OBS data having some missing and bad traces, some traces need to be interpolated into the common receiver gathers to obtain the re-sampled equal interval (say 20 m, originally 37.5 m) gathers. The interpolation must be carefully done without amplitude distorting AGC processes so as to obtain high quality τ-p transform with true amplitude.

To match OBS hydrophone gathers with the processed multichannel streamer data, gain recovery is used to keep similar trends in amplitude change in the two datasets. Near offset traces from OBSs 101ns, 102ns, 103ns and 106ew are superimposed on the 2-D mulichannel Line 206 (originally Line 103) as displayed in Fig. 3.9; we see an excellent match of seafloor and BSR between the two datasets. Many reflections can be reliably correlated between the two data sets.

Another aim of OBS data processing is to extract the true amplitudes of the

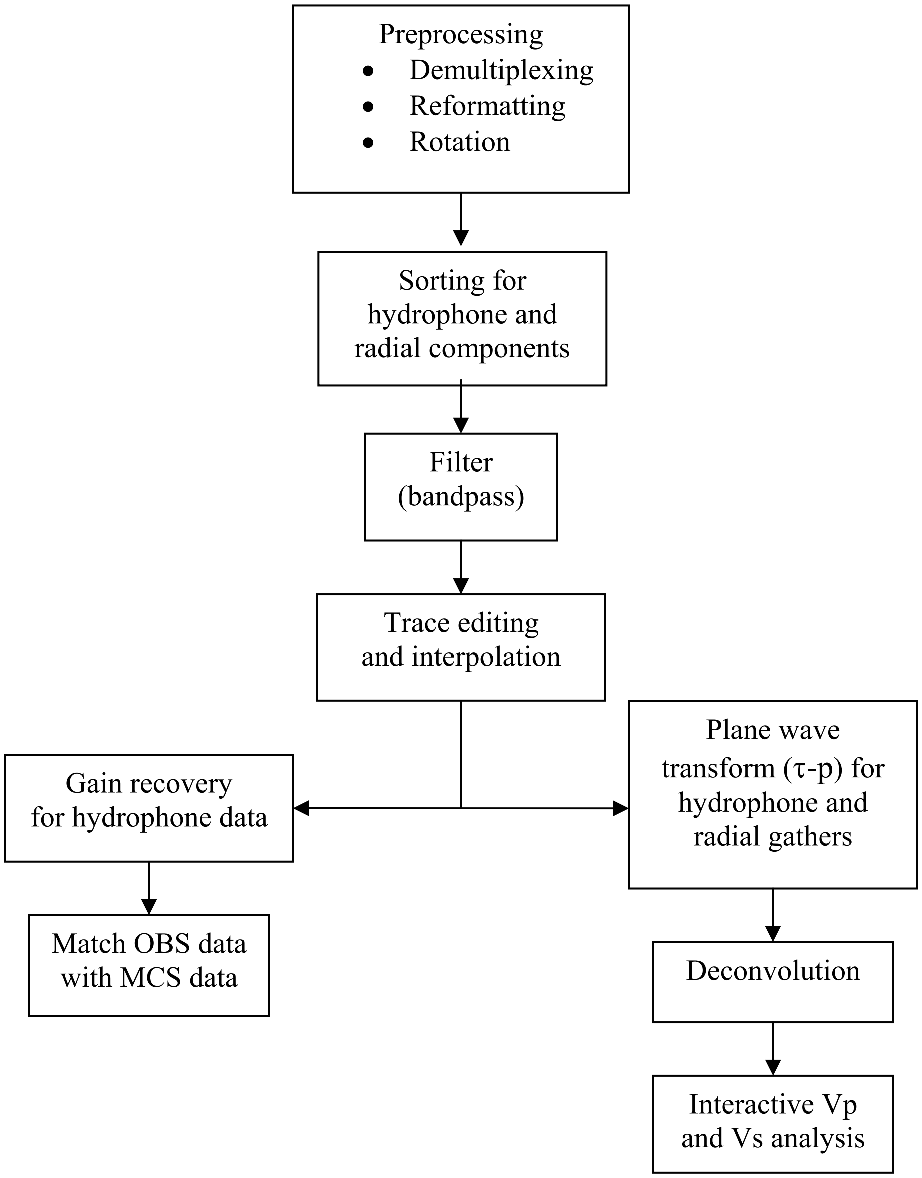

Fig. 3.6. Data processing flowchart

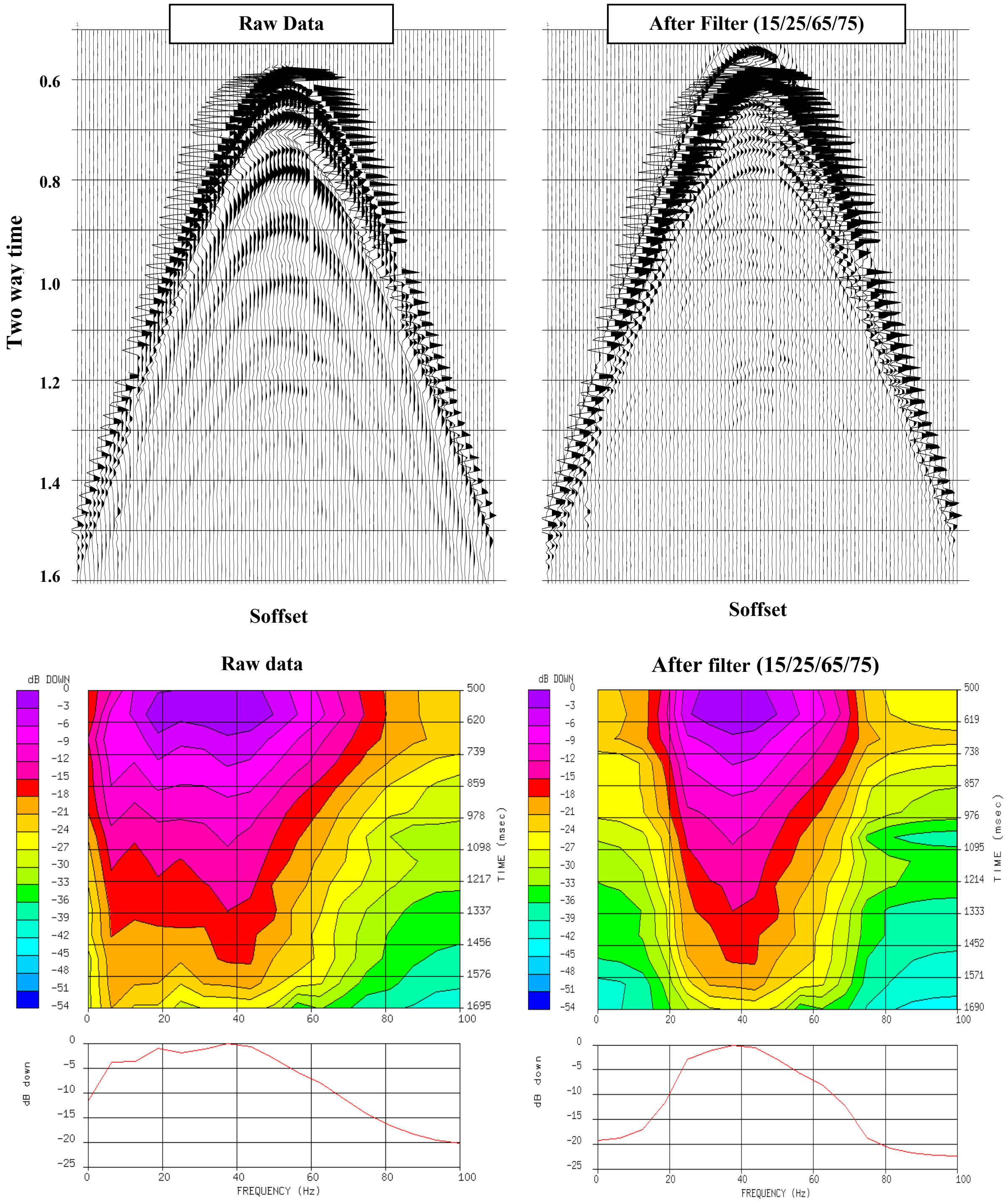

Fig. 3.7. (Upper) OBS l02NS-4 (hydrophone) display. (Left upper panel) Raw data: major reflectors between 0.6 and 0.8 s at near offset are unclear. (Right upper panel) After filtering: major reflectors between 0.6 and 0.8 s at near offset clearly appear. (Lower) OBS l02NS-4 (hydrophone) spectral analyses. (Left lower panel) Raw data. (Right lower panel) After filtering.

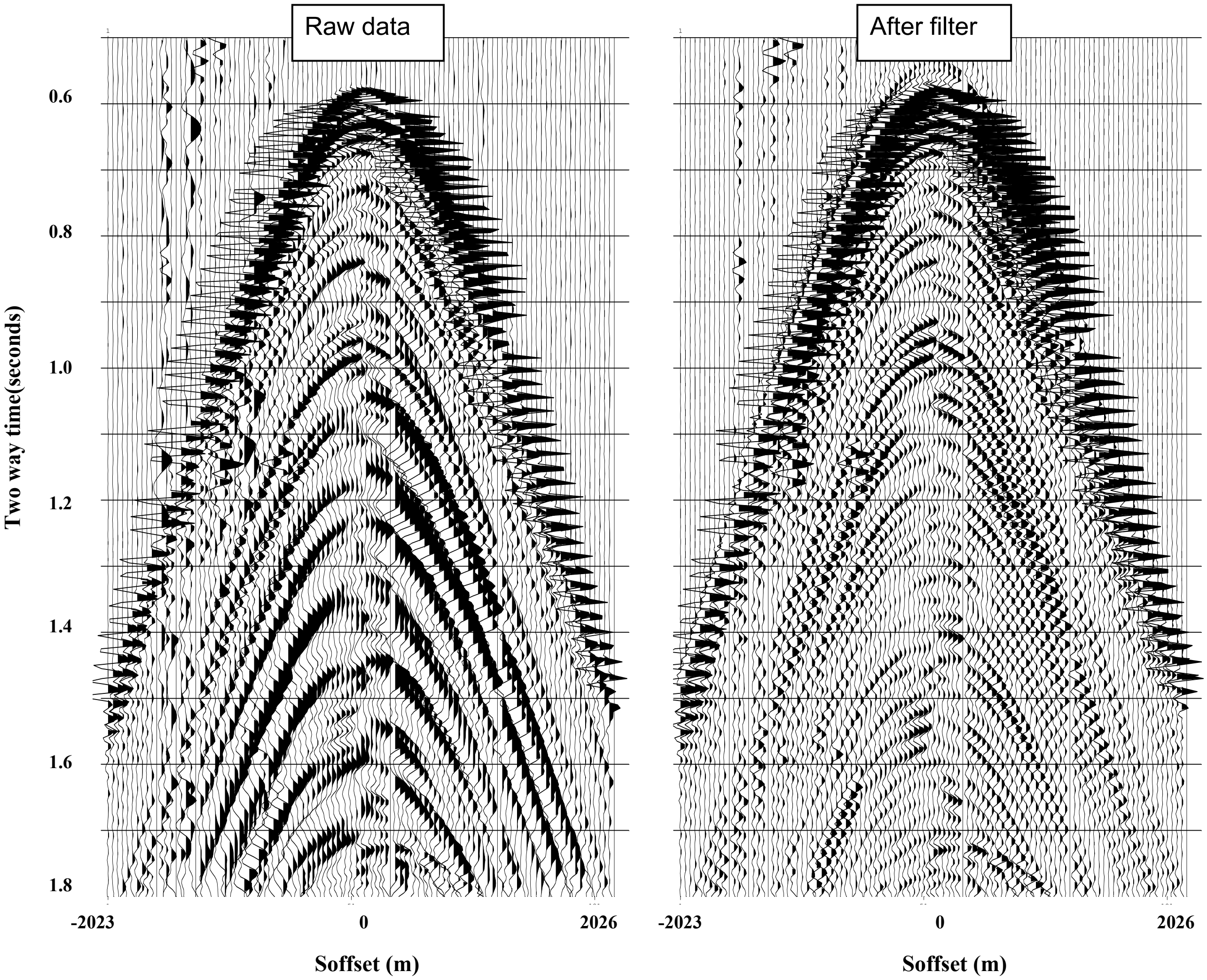

Fig. 3.8. OBS l02NS-2 (radial component) display. (Left panel) Raw data: major reflectors between 0.6 and 1.2 s at near offset are unclear. (Right panel) After filtering: major reflectors between 0.6 and 1.2 s at near offset clearly appear.

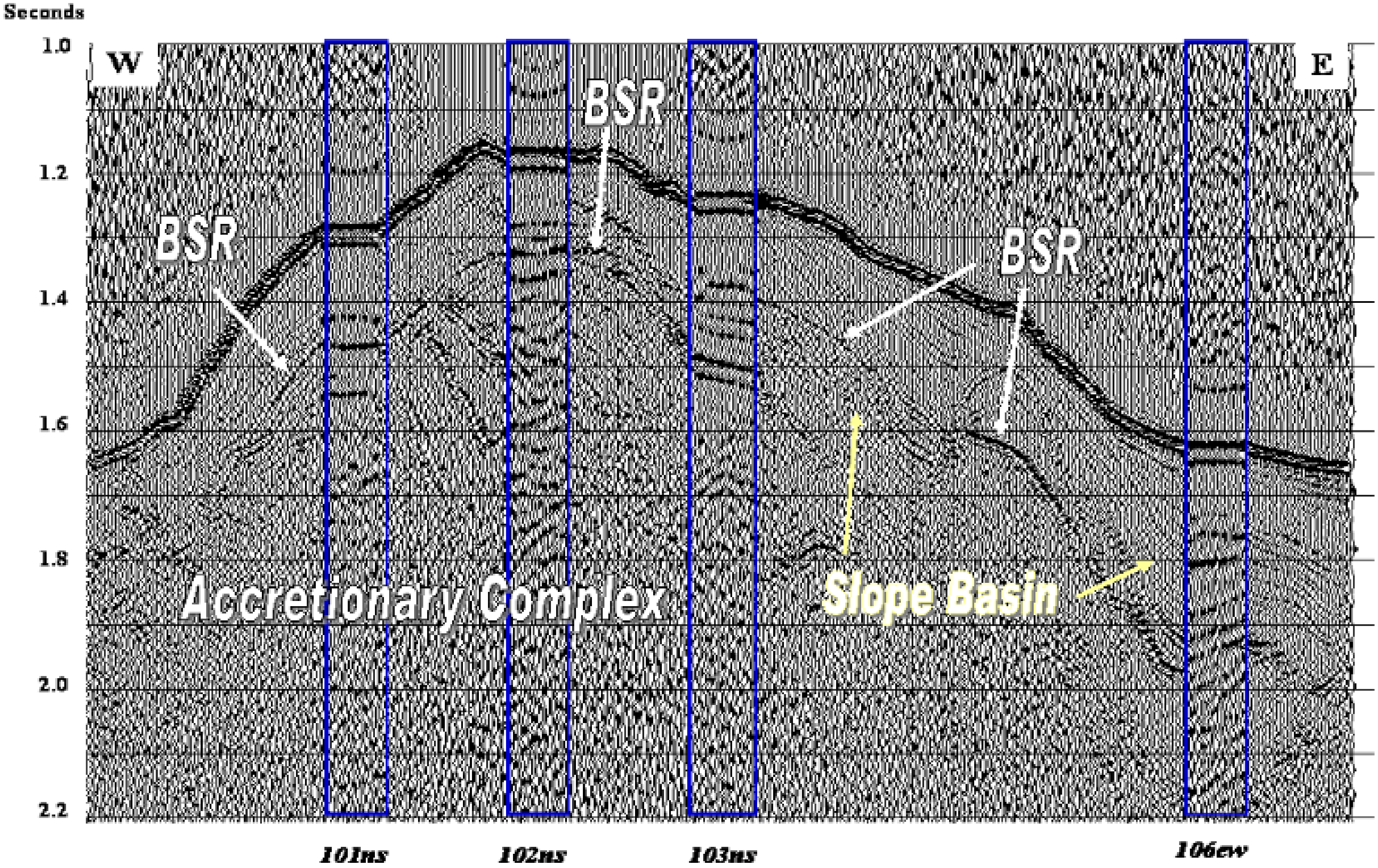

Fig. 3.9. OBS data superimposed within multi-channel Line 206 (original 103, close to EW1 in Fig. 3.5). BSR can be identified clearly in two datasets and can also be matched very well between two datasets.

reflected PP- and PS-waves, and the robust estimates of P- and S-wave velocities. In our study, a τ-p moveout technique is used to estimate preliminary P-wave and S-wave velocities. To do this, the necessary processing include: plane wave (τ-p) transform, deconvolution and interactive Vp and Vs analysis.

3.5 Vp and Vs Analysis: τ-p Moveout

The use of both P- and S-wave reflections in the OBS data can help in robust estimates of P- and S-wave velocities. After the necessary plane wave processing of the OBS data, the interactive P- and S-wave velocity analysis in the τ-p domain is used to estimate P- and S-wave velocities. The estimated preliminary Vp and Vs profiles as well as densities obtained from regional data are used as an initial model for waveform modeling and inversion for Vp from streamer data.

3.5.1 P- and S-wave velocity analysis

P-wave rms (root mean square) velocity can be routinely obtained from normal moveout of hydrophone common mid-point (CMP) gathers. However, the procedure for estimation of S-wave velocity from P-SV reflection is slightly different. The general procedure for obtaining the estimate of S-wave velocity inlcudes:

- Estimate the Vp/Vs ratio γ from normal incidence PP and PS times.
- Use γ to compute conversion points and sort CMP PS gathers into common coversion point (CCP) gathers.

- Apply an rms stacking velocity analysis (with non-hyperbolic terms) of CCP gathers.

Here I employ τ-p interactive PS velocity analysis of common receiver gathers along strike line (nearly 1D structure) to obtain Vs interval velocity. The advantages of analysis in the τ-*p* (intercept time-ray parameter) domain compared to that in the *X*-*T* (distance-time) have been shown by many studies (e.g., Bessonova et al., 1974; Henry et al., 1980; Stoffa et al., 1981; Kappus et al, 1990; Sen, 2001). In the case of a 1-D structure, one advantage is that along each ray path the ray parameter is a constant so that each trace in the τ-*p* domain represents a different plane wave component; difficulties caused by *X*-*T* domain triplications are avoided because τ is a single-valued, monotonically decreasing function of *p*. The τ-*p* trajectory of the PP-waves and the converted PS-waves are given respectively by:

$$\tau_{pp}(p) = 2\, q_p \Delta z, \tag{3.1}$$

$$\tau_{ps}(p) = \Delta z\, (\, q_p + q_s), \tag{3.2}$$

where Δz is the layer thickness, and q_p and q_s the vertical slownesses of the P- and S-waves respectively. For an isotropic medium, we have:

$$\tau_{pp}(p) = 2\tau_p^0\, (1 - p^2 v_p^2)^{1/2}\,, \tag{3.3}$$

$$\tau_{ps}(p) = \tau_p^0\, (1 - p^2 v_p^2)^{1/2} + \tau_s^0\, (1 - p^2 v_s^2)^{1/2}, \tag{3.4}$$

where equation 3.3 is for PP-wave, and equation 3.4 is for converted PS-wave and τ_p^0 and τ_s^0 are one-way vertical (zero offset) delay times for P- and S-waves respectively.

The radial component geophone is designed to record S-wave particle motion. In the OBS case, the incident wave is a P-wave, and the converted waves arriving at the receiving station may be generated in two ways: (1) down-going P-wave is converted into up-going S-wave being reflected at a reflector (denoted as Rps), and (2) down-going P-wave is converted into down-going S-wave during transmission at a conversion surface and then is reflected as up-going S-wave at a lower reflector (denoted as Rpss) (Fig. 3.10).

For the Rps case, suppose there are n layers of isotropic media, then we have cummulative (total) τ:

$$\begin{aligned} \tau_{ps}(p) &= \sum_{i=1}^{n} \Delta z_i (q_{pi} + q_{si}) \\ &= \sum_{i=1}^{n} [\tau_{pi}^{0} (1 - p^2 v_{pi}^2)^{1/2} + \tau_{si}^{0} (1 - p^2 v_{si}^2)^{1/2}], \end{aligned} \tag{3.5}$$

where Δz_i is the *i*th layer thickness, q_{pi} and q_{si} the vertical slownesses of the P- and S-waves for *i*th layer respectively, τ_{pi}^{0} and τ_{si}^{0} are the one-way delay time for *i*th layer for P- and S-wave at p = 0 respectively, and V_{pi} and V_{si} the velocities of the P-wave and S-wave for *i*th layer respectively.

For the Rpss case, suppose that there are n layers of isotropic media and conversion takes place at the reflector between the *k*th and (*k*+1)th layers, then we have cumulative (total) τ:

$$\begin{aligned} \tau_{pss}(p) &= \sum_{i=1}^{k} \Delta z_i (q_{pi} + q_{si}) + \sum_{i=k}^{n} 2 q_{si} \Delta z_i \\ &= \sum_{i=1}^{k} [\tau_{pi}^{0} (1 - p^2 v_{pi}^2)^{1/2} + \tau_{si}^{0} (1 - p^2 v_{si}^2)^{1/2}] + \sum_{i=k}^{n} 2\tau_{si}^{0} (1 - p^2 v_{si}^2)^{1/2}. \end{aligned} \tag{3.6}$$

We estimate the P and S wave velocities in the τ-p domain by interactively fitting trajectories for different trial V_p and V_s reflections and examining the NMO corrected

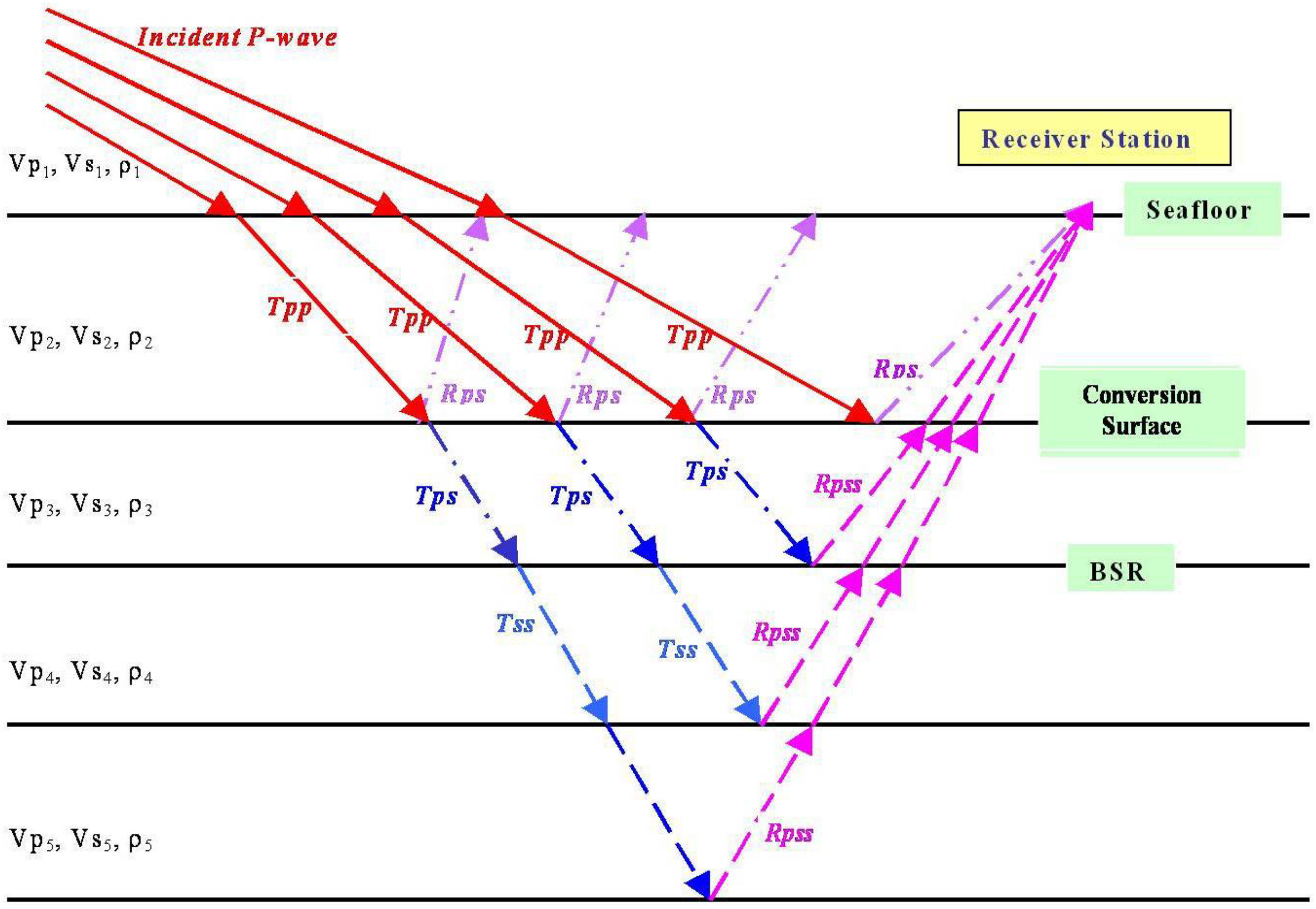

Fig. 3.10. Ray path and PS conversion.

data. The main steps are described below:

- Determine interval V_p by interactive delay-time ananlysis of hydrophone OBS gathers in plane wave domain. Given the V_p and two way time, I can also estimate the layer thickness $\Delta \boldsymbol{z}$.
- Given a series of the possible V_s values for each layer defined by the hydrophone gathers, use equations (3.5) and (3.6) to generate a table of the $\tau_{ps}(0)$ and $\tau_{pss}(0)$ values for the Rps and Rpss cases respectively based on the obtained $\boldsymbol{\tau_p}(0)$ and $\Delta \boldsymbol{z}$ vectors, which will be useful in identifying the types of converted waves.
- Estimate V_s from τ-p domain delay-time moveout fitting of radial component OBS gathers with *a priori* information of $\Delta \boldsymbol{z}$ and $\boldsymbol{V_p}$ vectors. This procedure results in $\boldsymbol{\tau_{ps}}(0)$ and interval velocity $\boldsymbol{V_s}$ vectors. After Vp is estimated, the table produced by equations (3.5) and (3.6) is used to predict the $\tau_{ps}(0)$ and $\tau_{pss}(0)$ of events interpreted in the S-wave data so as to correctly correlate them with those in P-wave data.
- Note that once reflectors are identified, Δz in both equations (3.1) and (3.2) or Δz in both equations (3.5) and (3.6) are identical. If the radial component record represents the converted-wave of Rps type, the correlation of the events identified from the radial component OBS gather with those from the hydrophone OBS gather requires that the equations (3.5) must be satisfied. This may be determined by checking whether the events will be flat in τ-p domain after NMO correction. If the converted wave of Rpss type takes place, equation (3.6) must be used.

3.5.2 Identification of the PS conversion surface and the BSR

The interactive V_p and V_s analysis of the OBS data in the τ-p domain allow identification of two types of converted-waves (Rps and Rpss) and a conversion surface (Fig. 3.10**)**, separating a layer with low P-wave velocity overlying a layer with high P-wave velocity. An incident P-wave converts into a transmitted S-wave at this interface. The conversion surface is identified at the second major reflector below the seafloor with a lower V_p in the overlying layer and a high V_p in the underlying layer. We are able to match the moveout of reflection events in the radial OBS, only if we assume that the reflected waves directly from the conversion surface and the reflector above it belong to type Rps, and the reflected waves from reflectors below it belong to type Rpss.

Figs. 3.11 and 3.12 show the major reflectors, such as the seafloor, the conversion surface and the BSR, and their correlation at the hydrophone and radial component gathers of OBS 101ns and 102ns respectively in τ-p domain. Notice that the top of conversion surface is characterized by a fairly strong positive amplitude reflection but the BSR has a strong negative amplitude in the hydrophone component data. Because the changes in density may not be large, the large positive amplitude reflects a positive contrast at this surface, and the negative amplitude represents a sharp P-wave velocity drop from high velocity (gas hydrate) above the reflector to a low velocity (free gas) below.

3.5.3 Vp, Vs and Poisson's ratio profiles

The interactive *Vp* and *Vs* analysis of the OBS data produces the Vp and Vs profiles. Poisson's ratio, an important indicator of hydrocarbon, is defined as the negative

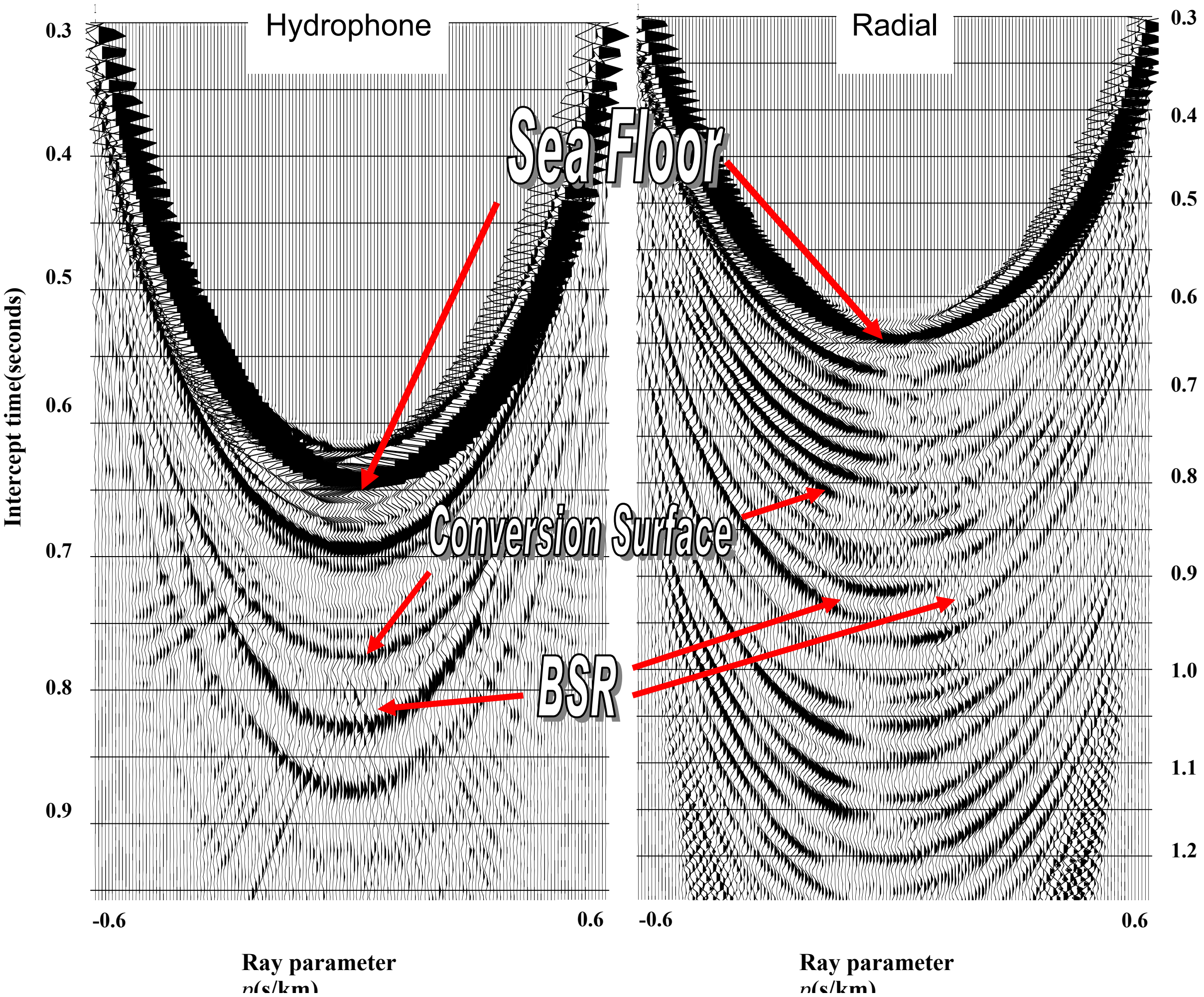

Fig. 3.11. OBS 101 gathers: major reflectors in τ-p domain. Left panel: hydrophone. Right panel: radial component. Notice the different time scales for hydrophone and radial components.

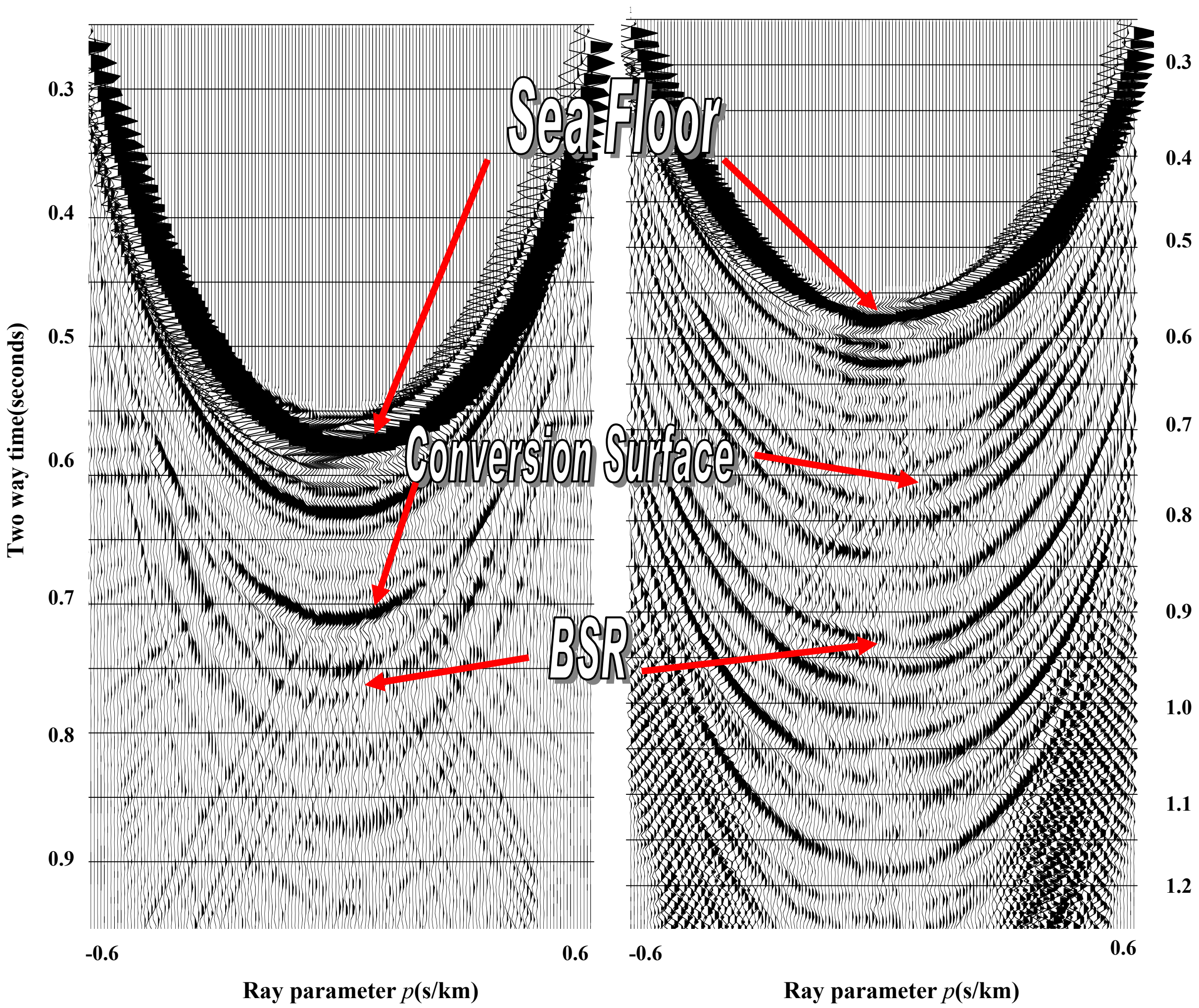

Fig. 3.12. OBS 102 gathers: major reflectors in τ-p domain. Left panel: hydrophone. Right panel: radial component. Notice the different time scales for hydrophone and radial components.

fractional change in width divided by the fractural change in length (ratio of transverse to axial strain) when the material is subjected to stress. Poisson's ratio may be directly related to the Vp/Vs ratio by

$$\sigma = \frac{0.5(V_p / V_s)^2 - 1}{(V_p / V_s)^2 - 1}. \tag{3.7}$$

The results of the interactive analysis of OBS 101ns and 102ns are shown in Figs. 3.13 and 3.14 respectively, where V_p, V_s and Poisson's ratio profiles are displayed in the left panel; hydrophone gathers with NMO correction (middle panel) are for V_p analysis and radial component gathers with NMO correction are for V_s analysis. A low value of Poisson's ratio seems to indicate the presence of free gas between the seafloor and the conversion surface as well as below the BSR.

Fig. 3.15 shows *Vp*, *Vs* and Poisson's ratio profiles of Line EW1, from which similar structures of *Vp*, *Vs* and Poisson's ratio can be observed among different OBS locations. The estimated *Vp* and Vs profiles, as well as density profile from the regional data, can be used as initial model for waveform inversion.

3.6 Pre-stack Waveform Modeling and Inversion of Streamer Data

Preservation of the true amplitude in the seismic data is key to the success of waveform modeling and inversion. Since OBS data are recorded only at sparse locations and recovery of true vector amplitude may not be reliable, we made use of large offset streamer data in our modeling and inversion.

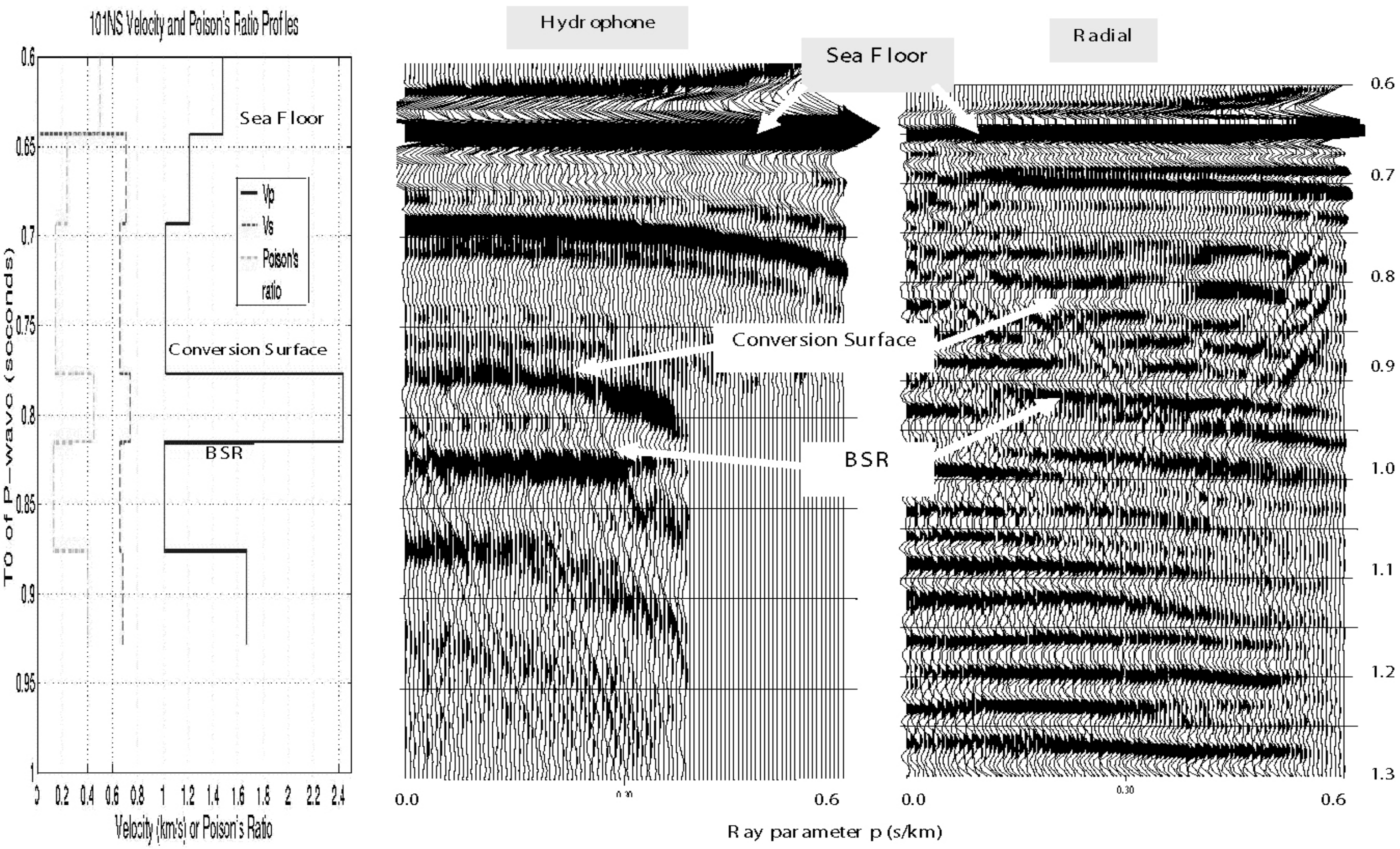

Fig. 3.13. Interactive moveout analysis in τ-p domain for OBS 101 gather. Left panel: derived Vp (−) and Vs (--), and poisson’s Ratio (−·). Middel panel: Hydrophone gather with NMO correction. Right panel: Radial component gather with NMO correction.

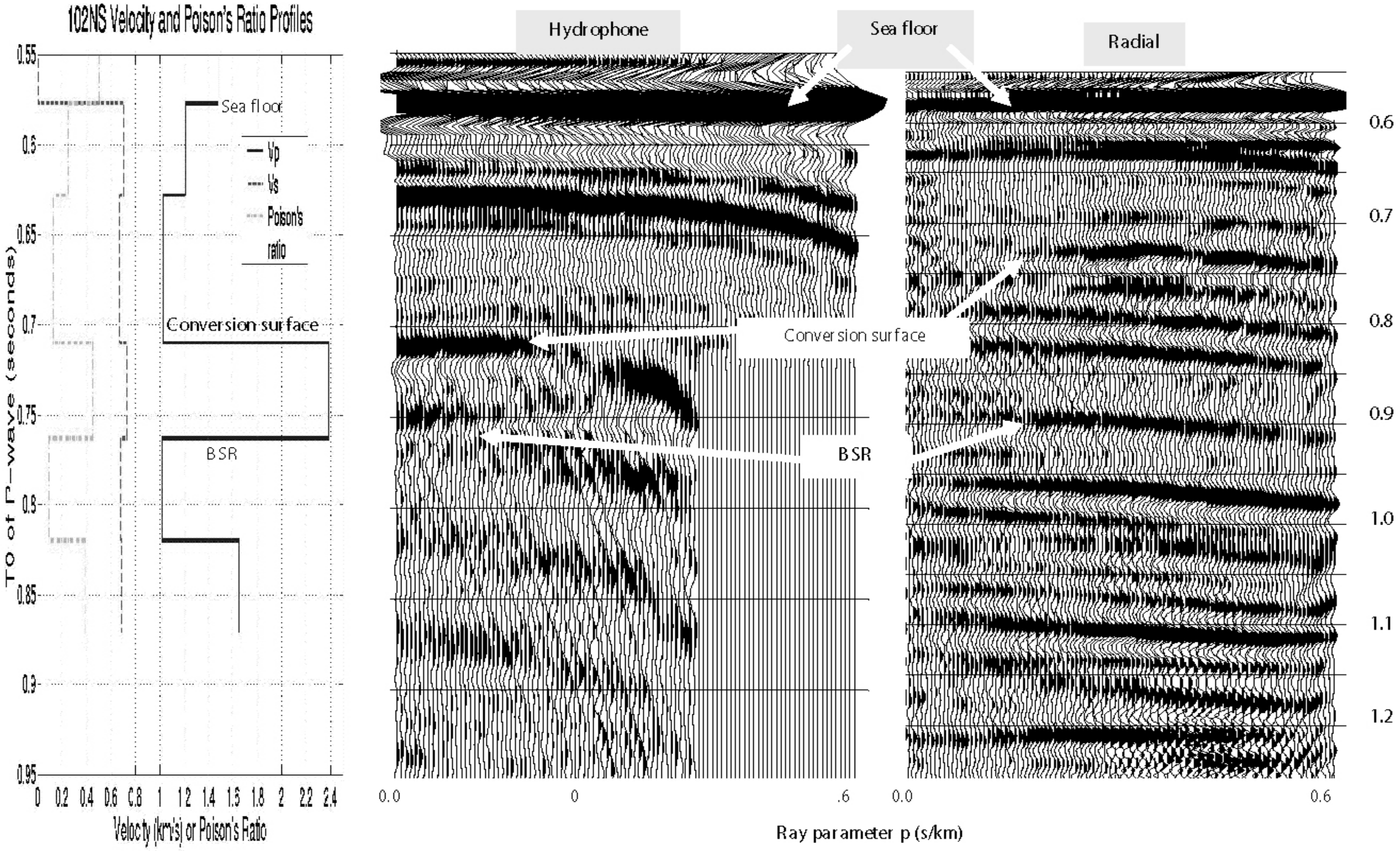

Fig. 3.14. Interactive moveout analysis in τ-p domain for OBS 102 gather. Left panel: derived Vp (−) and Vs (--), and poisson's Ratio (−·). Middel panel: Hydrophone gather with NMO correction. Right panel: Radial component gather with NMO correction.

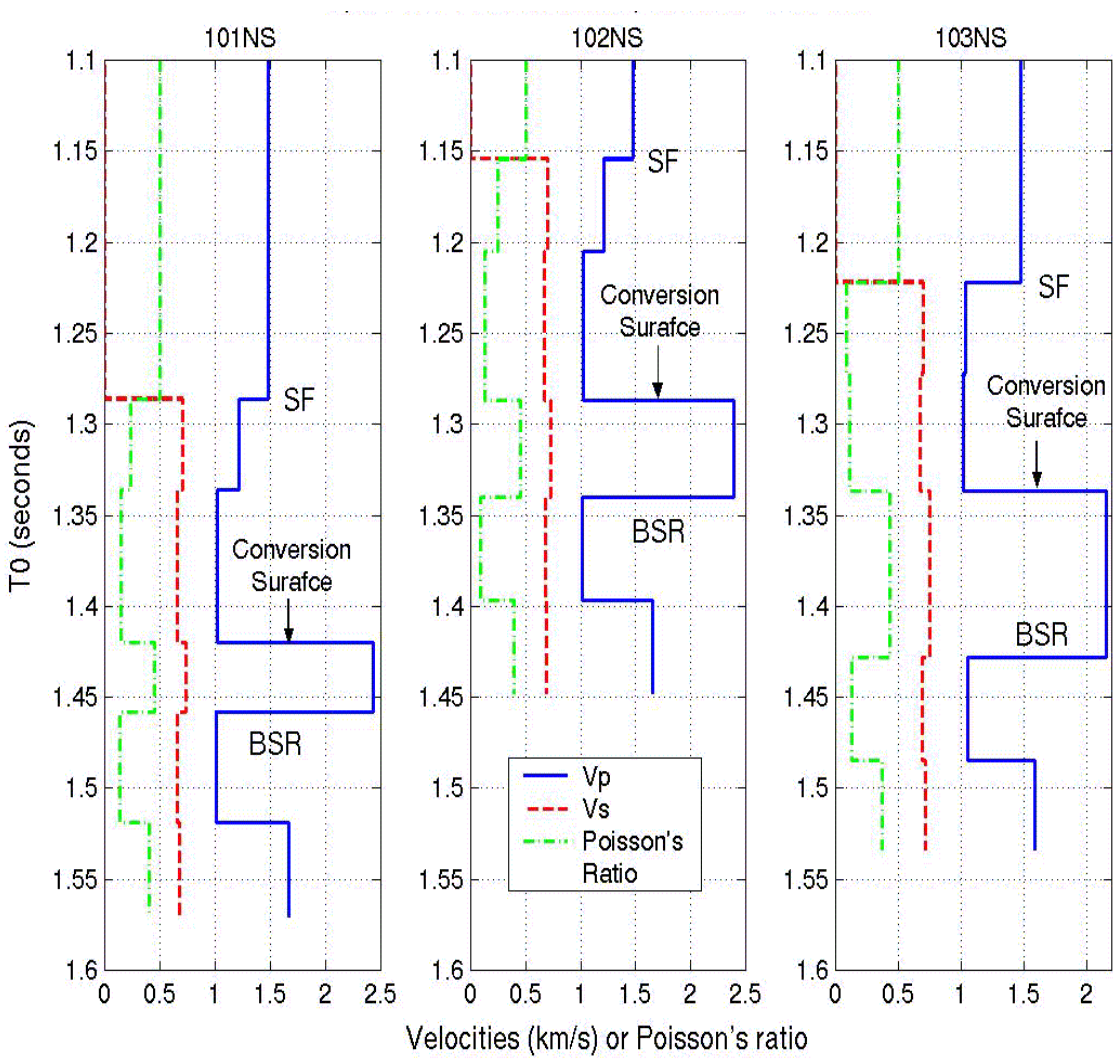

Fig. 3.l5. Vp, Vs and Poisson's ratio profiles of Line EW1 at three OBS locations derived from interactive analysis.

3.6.1 Forward modeling

The reflectivity method has been used extensively to model seismic data (e.g., Kennett, 1983). The reflection formulation, computing a complete seismic response that includes mode conversions and multiple reflections, can be modified to obtain primary reflection (PP- and PS- waves) energy only, or primary PP-wave energy only. The reflectivity method is a good choice for generating synthetic PP- and PS-wave seismograms with multiple offsets in a 1-D model because it is unconditionally stable. For this application I made use of synthetic seismograms for P-wave primary only.

Let us consider an isotropic stratified elastic medium which consists of a stack of thin homogeneous layers less than ½ or ¼ of the shortest wavelength of interest. An isotropic elastic earth model is described by three parameters: density, P- and S-wave velocities. Fig. 3.16 illustrates such an isotropic medium with n layers. I first construct the synthetics in frequency-ray parameter domain, and then use an inverse temporal Fourier transform to obtain (τ,p) seismograms. For each reflector, the *P-P* reflection coefficient can be calculated by using the exact formula which is expressed in terms of the ray parameter *p* (Aki and Richards, 1980). Therefore, we can obtain a reflection coefficient vector for the n reflectors using the exact equation:

$$\boldsymbol{r} = [r_1, r_2, \ldots, r_n]. \qquad (3.8)$$

The travel time corresponding to each reflection event corresponds to the vertical delay time τ which is a function of the ray-parameter p.

Considering a source wavelet vector ***w***, the synthetic seismograms can be obtained by convolution of vector ***r*** and vector ***w***:

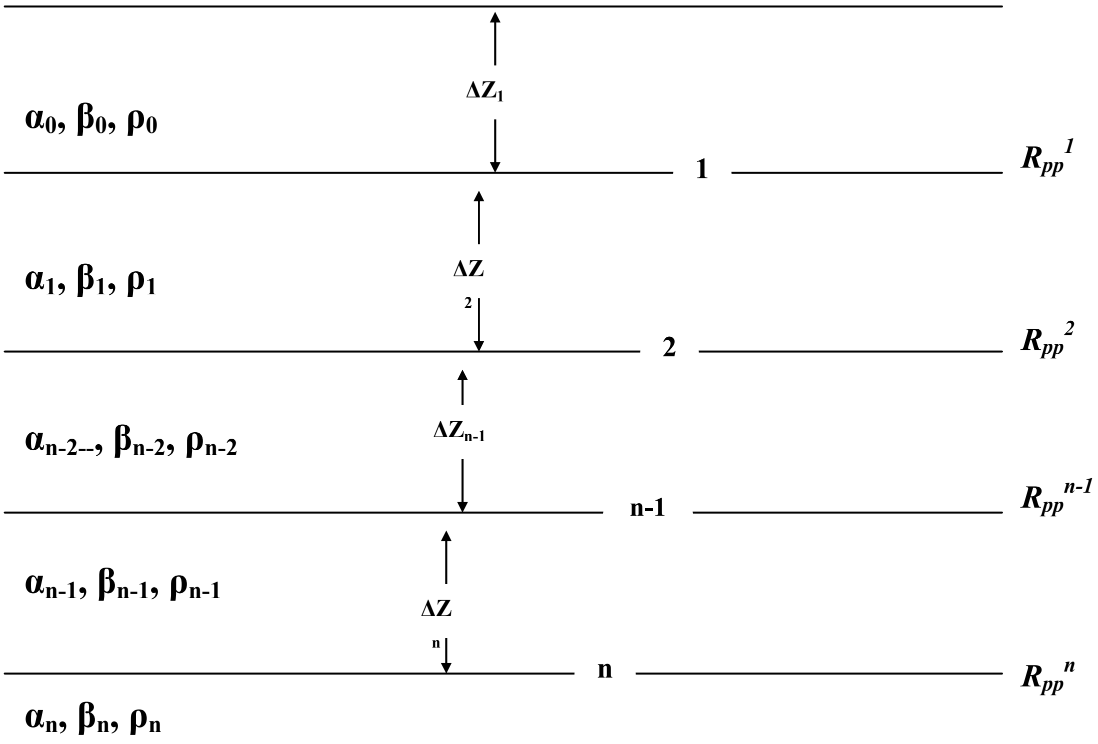

Fig. 3.16. General model describing n layers of the isotopic media.

$$s(t, p) = r(t, p)*w(t), \qquad (3.9)$$

Considering post-critical angles, both sides of equation (3.9) are complex. Therefore, we need to use the Hilbert transform to describe the imaginary part of the complex values in the (ω,p) domain. Now let us take temporal Fourier transforms on to both sides of equation (3.9), and then we have:

$$S(\omega, p) = R(\omega, p)W(\omega, p). \qquad (3.10)$$

In practice, we do not calculate the convolution of vectors ***r*** and ***w*** in the (τ, p) domain, but apply simple multiplication in the (ω, p) domain. By an inverse temporal Fourier transform, we go back to the (τ, p) domain to obtain the synthetic seismograms. The inversion and optimization algorithms are identical to those described in Chapter 2.

3.6.2 Pre-stack data for inversion

Since the OBS data were recorded only at some sparse spatial locations, I used large offset streamer data in this inversion. Due to its close proximity to the OBS 102ns, I first inverted CMP 1820 followed by several CMP gathers along the line which were inverted. The data processing steps mainly include band-pass filtering and plane-wave transformation.

I applied pre-stack (multi-offset) waveform inversion for *Vp*, impedance, and Poisson's ratio with an assumption that the medium is isotropic and is described solely by *Vp*, *Vs* and density. The *Vp* and *Vs* profiles obtained by the interactive travel-time analysis from OBS 101ns and 102ns were used as the starting model. The initial density profile was obtained by estimation based on the regional data.

Note that the key to a successful pre-stack waveform inversion for *Vp* is that the arrival times and moveouts of major reflectors in the final synthetic data are precisely matched with those in the observed data. Density and S-wave velocity influence only amplitude rather than moveout. In other words, the nonlinearity in the inversion is caused by the low frequency component of *Vp* and the low frequency component needs to be estimated accurately for use in the pre-stack inversion.

The inverted Vp profile of CMP 1820 is shown in Fig. 3.17, and the observed data and final synthetic data are shown in Fig. 3.18. The inverted Vp gradient is different from the conventional Vp gradients involving gas hydrates. In most regions, the Vp curve over gas hydrate-bearing sediments gradually increase with depth below the seafloor, attaining high values corresponding to the velocity of normal gas hydrate, and then sharply drops at the base of gas hydrate (Fig. 3.19). Contrary to this, the inverted Vp profile from seismic data obtained in the Hydrate Ridge area shows that there is a low-velocity layer with increasing Vp gradient between the seafloor and normal gas hydrate (Fig. 3.17). As explained later, this lower velocity layer exists under the summit area from CMP 1820 to CMP 2200 sites along Line 103. The comparisons between the observed and final synthetic data in the τ-p domain for different p values (here is 0.12, 0.20 and 0.3) are shown in Figs. 3.20, 3.21 and 3.22. We can see that the main reflectors are matched very well. The good match of the two data sets demonstrates that the estimated P-wave velocity estimates are reliable.

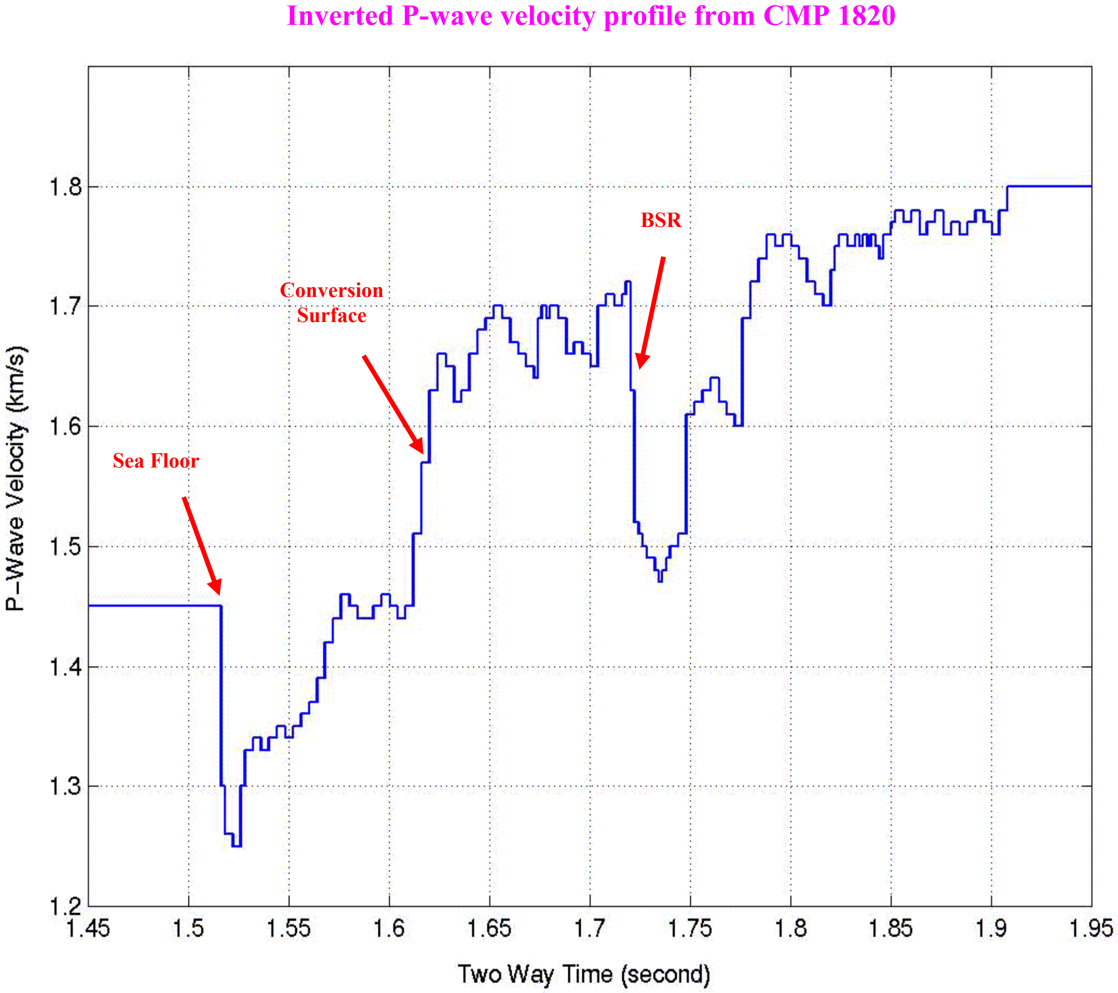

Fig. 3.17. Inverted P-wave velocity profile from CMP 1820. Major reflectors such as seafloor, conversion surface and BSR can be identified. There is a layer with low velocity right below the sea floor, which is different from conventional Vp profiles. Normal gas hydrates occur between the conversion surface and the BSR.

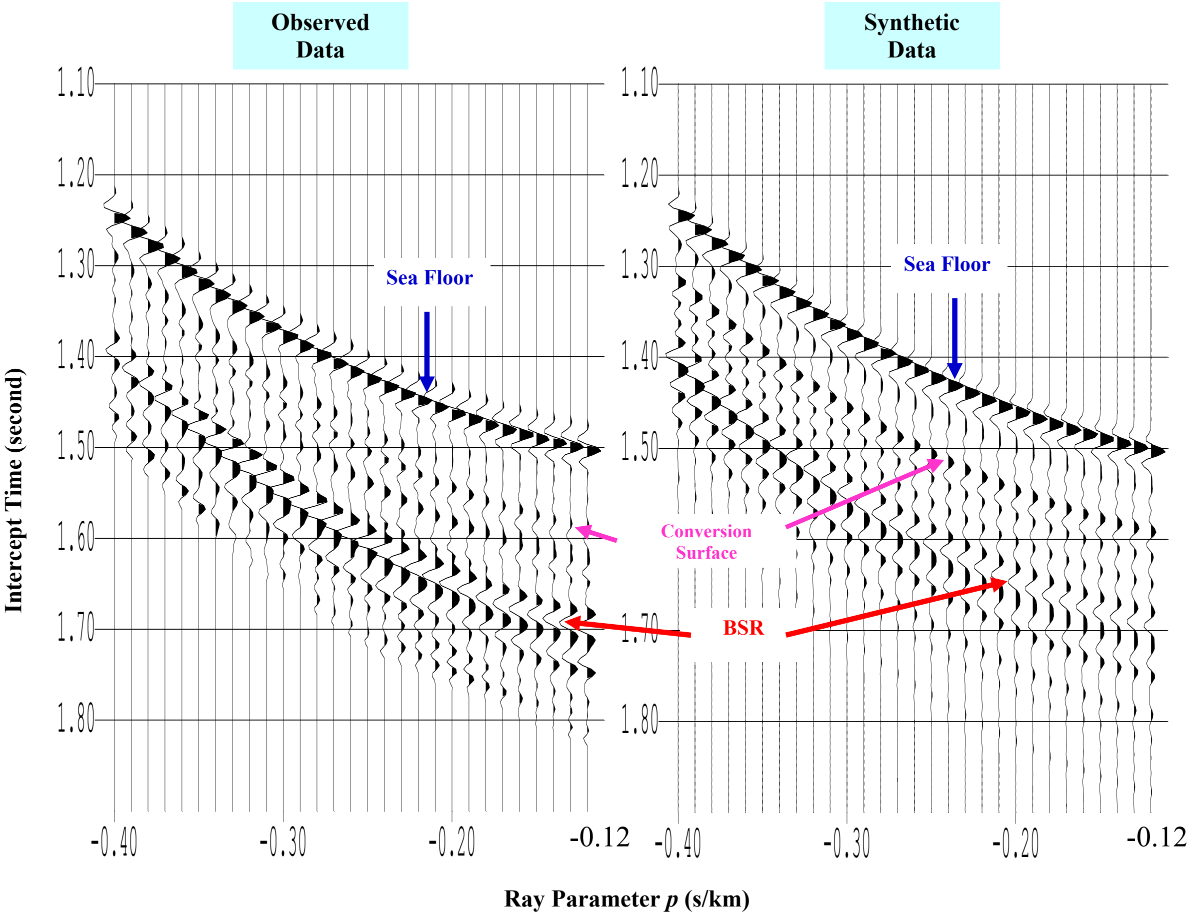

Fig. 3.18. CMP 1820 for inversion: Observed data and final synthetic data in τ-p domain. Notice that move out of major reflectors in the two datasets are precisely matched.

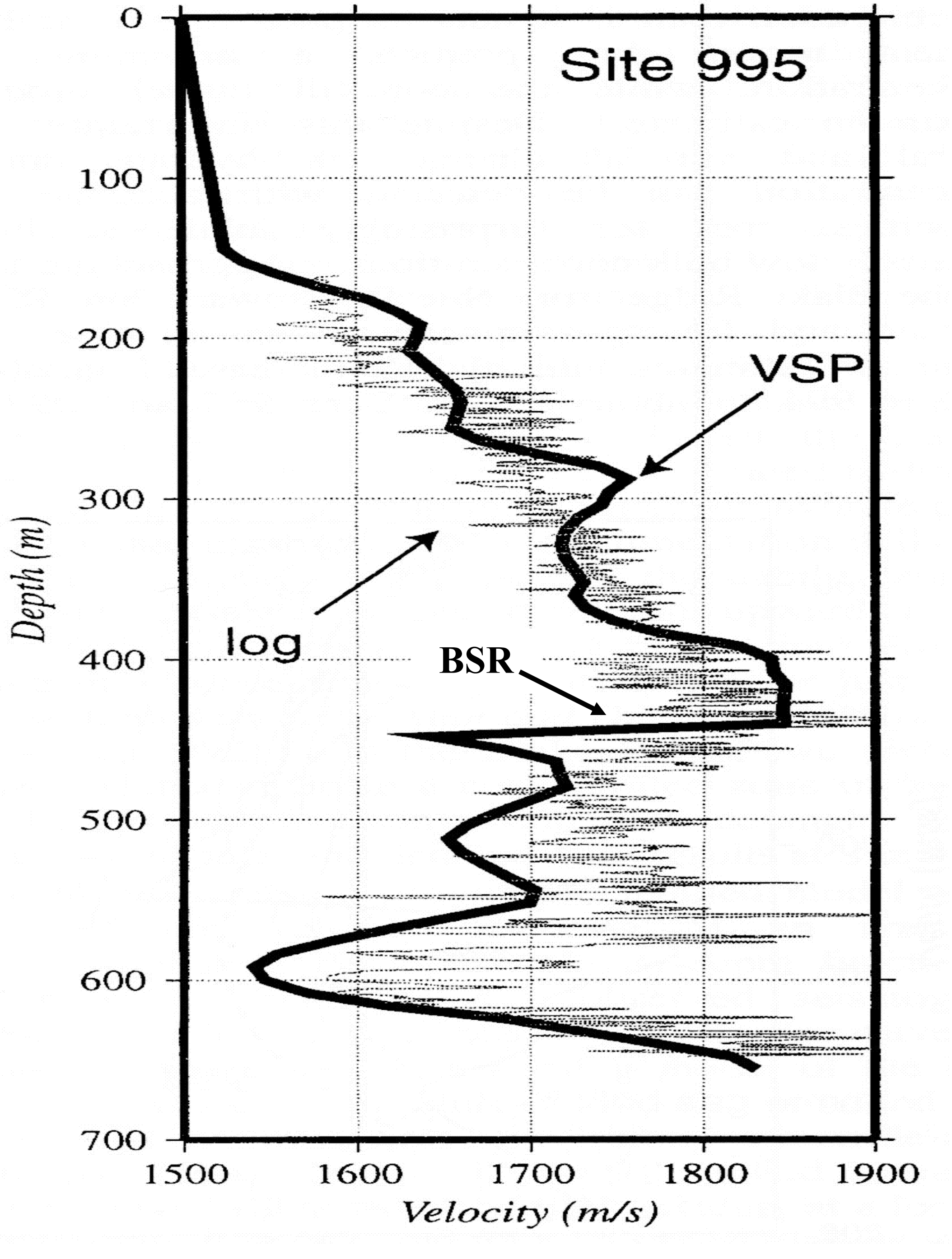

Fig. 3.19. P-wave velocities determined at Site 995 on the Blake Ridge offshore South Carolina from vertical seismic profiles (thick line) and sonic logs (thin dotted lines). (From Holbrook, 2001)

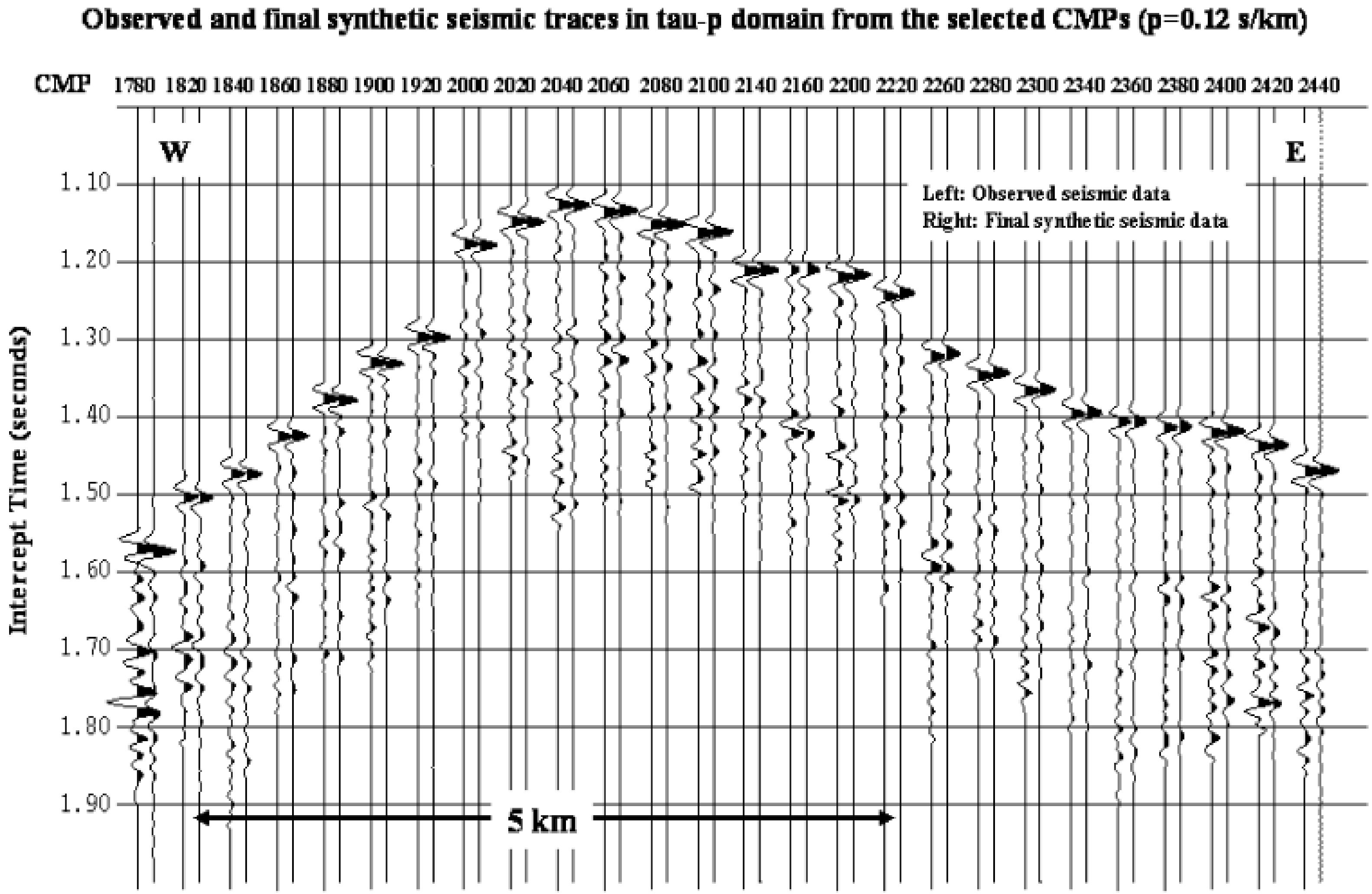

Fig. 3.20. The comparisons between observed and final synthetic traces in the tau-p domain from the elected CMPs for p = 0.12 s/km. The zone of interest between CMP 1820 and 2220 is the summit area over the Hydrate Ridge.

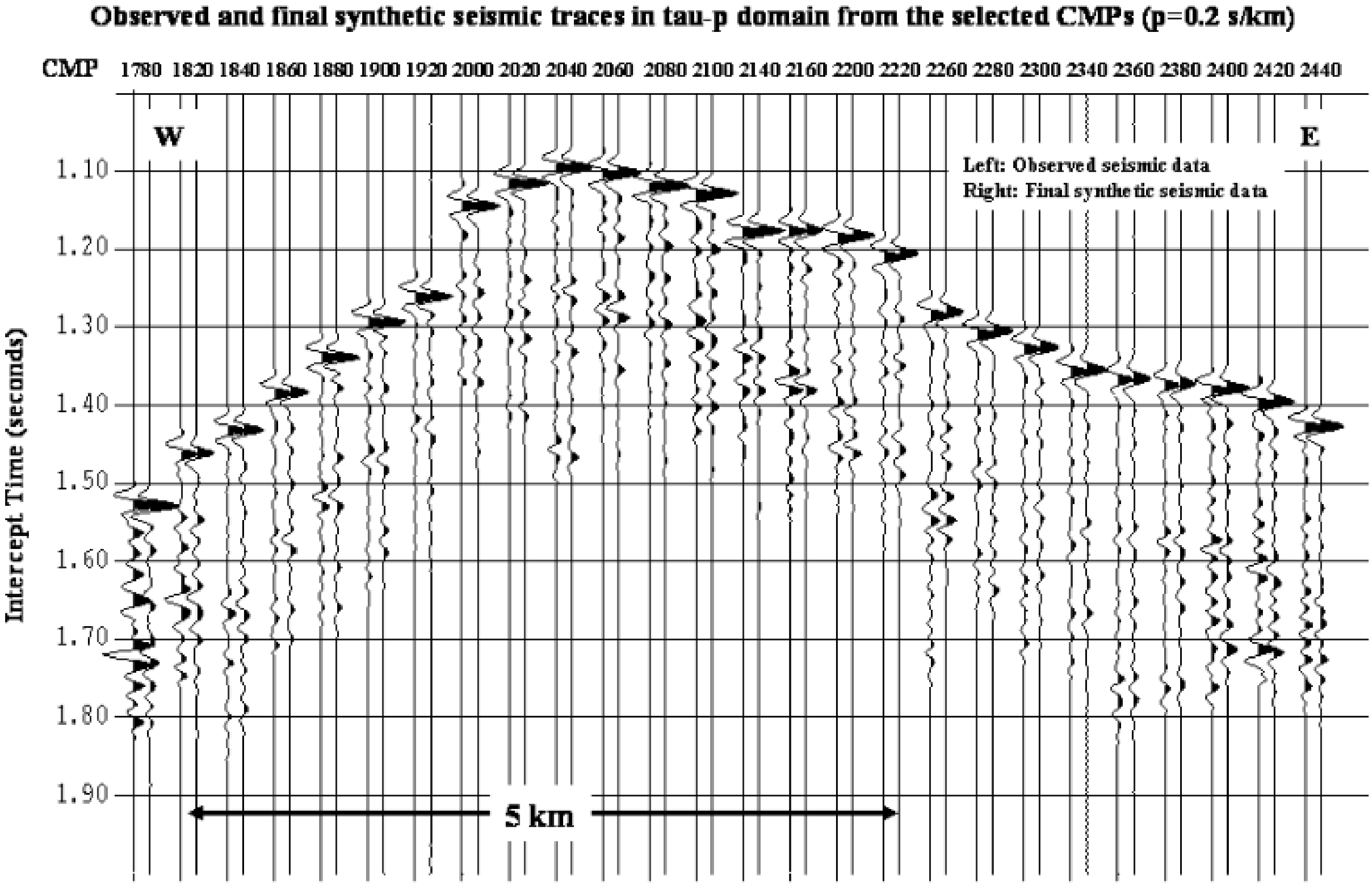

Fig. 3.21. The comparisons between observed and final synthetic traces in the tau-p domain from the elected CMPs for p = 0.20 s/km. The zone of interest between CMP 1820 and 2220 is the summit area over the Hydrate Ridge.

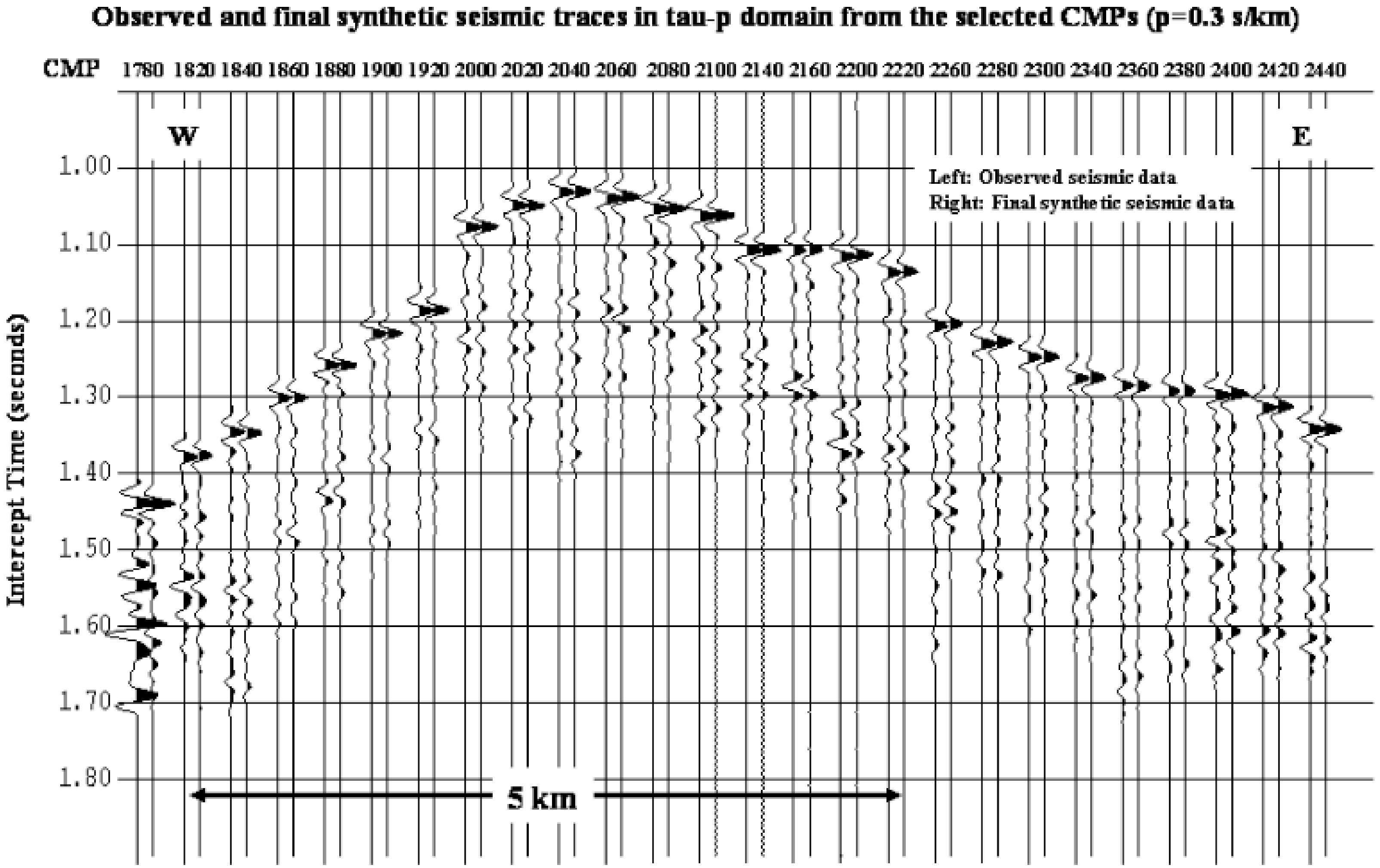

Fig. 3.22. The comparisons between observed and final synthetic traces in tau-p domain from the elected CMPs at p = 0.30 s/km. The zone of interest between CMP 1820 and 2220 is the summit area over the Hydrate Ridge.

3.7 Analysis of the results

The waveform modeling and inversion results are given in horizon maps of compressional wave velocity, impedance and Poisson's ratio, which can be used to infer geological interpretation of the area. In this section I focus primarily on the analysis of results. However, I will first summarize some of some related prior work that I will draw upon.

3.7.1 Review of previous work

In the 3-D survey area two distinct sedimentary sequences, accretionary complex and slope basin sediments, can be identified. Fig. 3.9 shows a preliminary processed profile extracted from the northern end of the 3-D survey volume. The pervasively deformed accreted sediments exhibit very few coherent reflections, whereas the slope-basin sediments exhibit strong, well-defined sedimentary bedding reflections. The migrated seismic section demonstrates a consistently stronger bottom-simulating reflection (BSR) in one of the two sedimentary sequences, indicating the presence of gas hydrates above and accumulation of free gas below. The BSR forming in the accretionary complex is generally 2-4 times larger in amplitude than that forming in the 300-500m thick slope basin sediments. The amplitudes of the reflection beneath the hydrate stability zone in both the accretionary complex and slope basin sediments decrease as they cross the BSR into the hydrate stability zone. Stratigraphic reflections cut across the BSR.

Under the southern crest of the Hydrate Ridge a series of seaward faults, which may serve as good conduits of ascending fluids, are demonstrated on the seismic section shown in Fig. 3.23.

Suess et al. (2001) reported their observations on sea floor methane hydrates in near-surface sediments at the Hydrate Ridge. Their work focused on the biogeochemical processes associated with gas hydrate dynamics and fluid venting at the central offshore Oregon. Combination of interstitial Cl-anomaly pattern and video-guided sampling has revealed that

- the uppermost sediment column contains several distinct layers of gas hydrate which are exposed at the seafloor.
- The gas hydrate fabric is highly variable with porous to massive gradations.
- The Cl-depletion pattern of porous waters is used to estimate amounts of gas hydrate in sediments.

A pavement was imaged on Hydrate Ridge by a deep-towed video survey in 1996. A giant video-guided grab sampler retrieved nearly 50 kg of massive hydrate from the southern summit of the Hydrate Ridge under 785 m of water. Fig. 3.24 demonstrates evidences of fluid venting and acoustic plume and two types of hydrate samples. Observations from the submersible showed methane bubble escaping from the top of the ridge. An acoustic image shows a >200 m high anomaly in the water column emanating from the southern summit, which is confirmed to be caused by vigorous bubbling (Fig. 3.24a). An orifice of venting is imaged in Fig. 3.24b. At Hydrate Ridge, gas hydrate occurs in discrete layers at the sediment water interface only millimeters below the

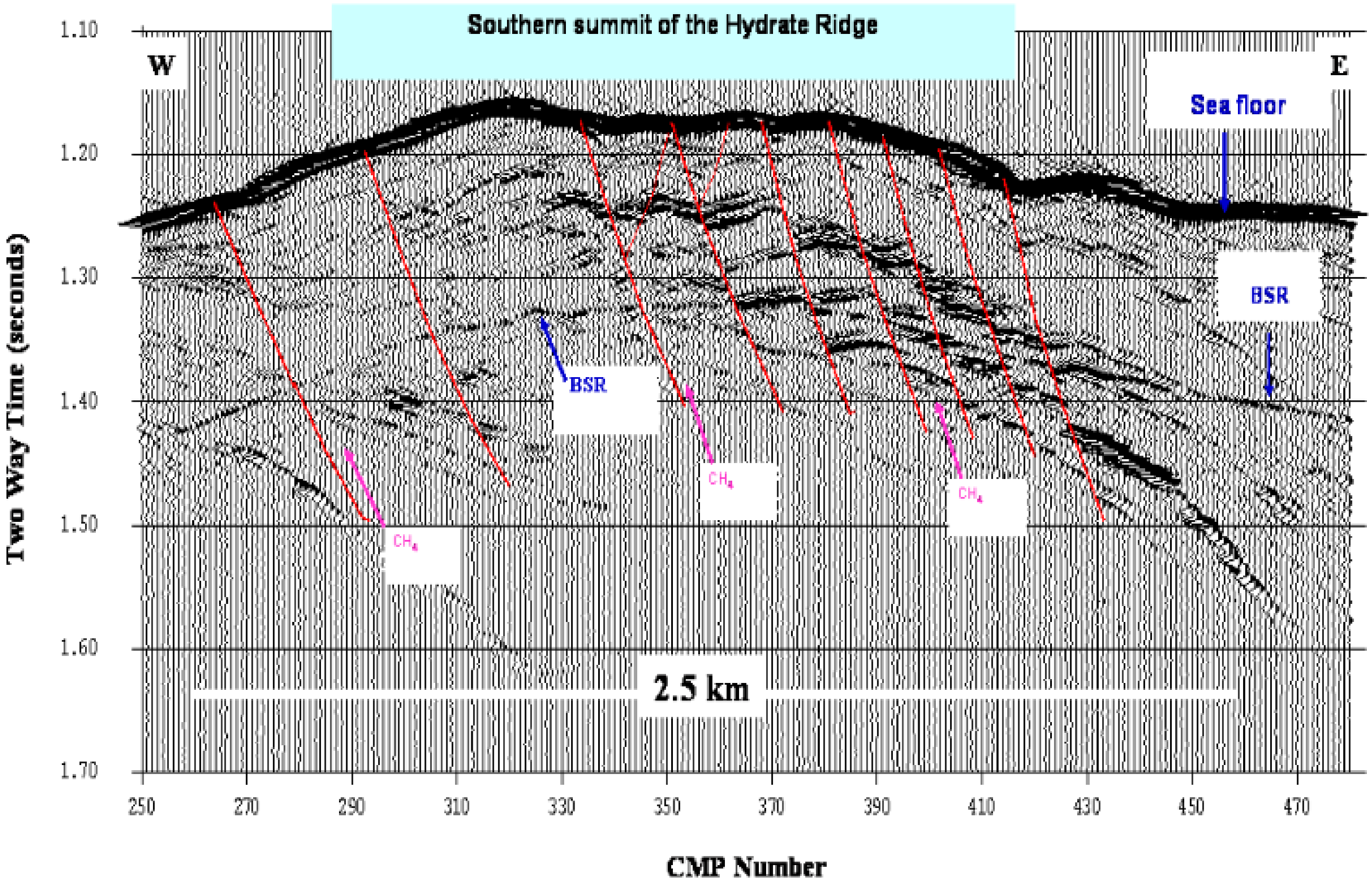

Fig. 3.23. Geological structure of the southern summit area. A series of faults serve as conduits of ascending fluids. The range of CDPs equals to CMPs 1960-2180 in Figs. 3.20-3.22.

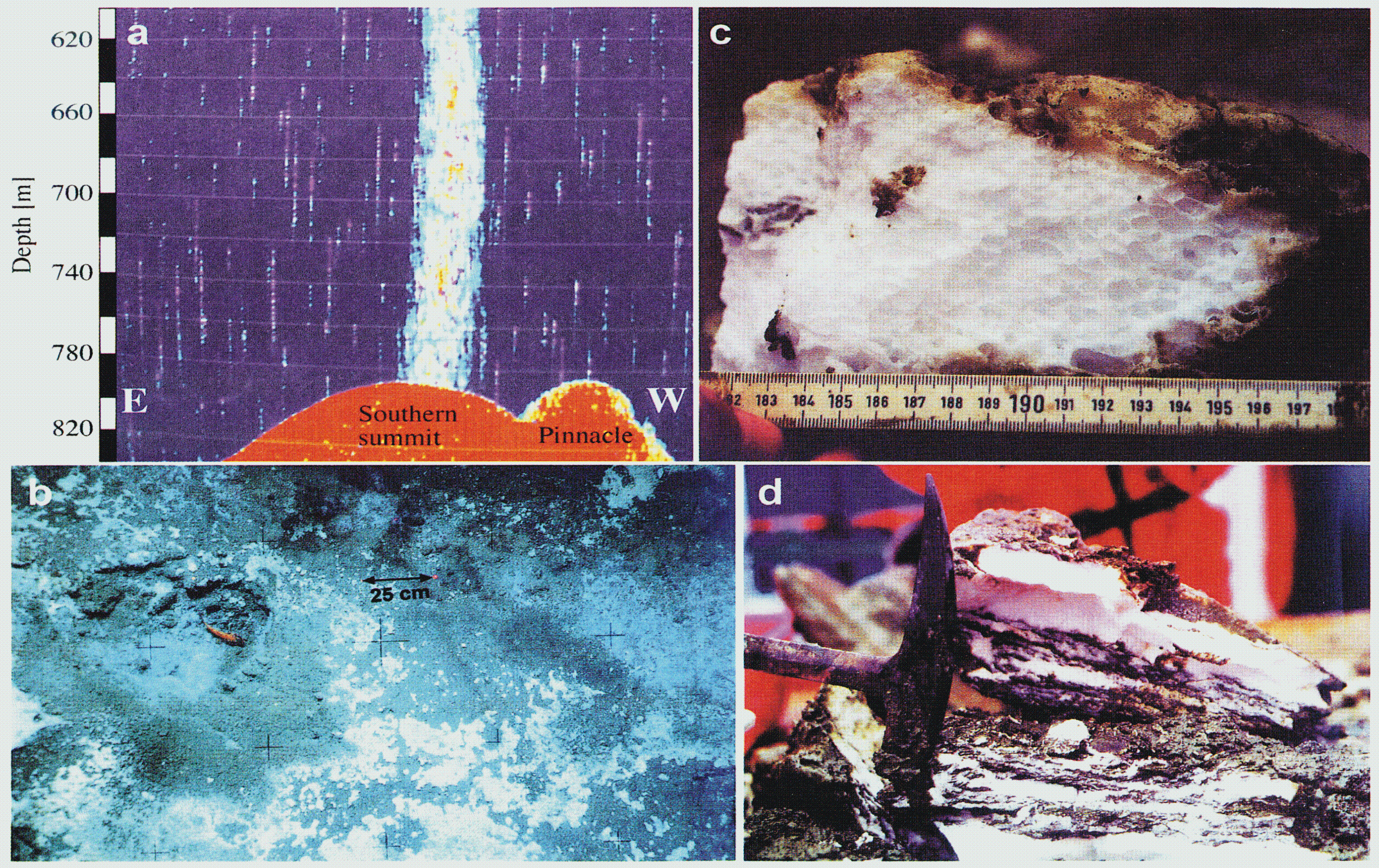

Fig. 3.24. (a) Plume image above southern summit and carbonate pinnacle; (b) Sea floor photo of microbial mat and orifice of vent; (c) Hydrate bubble-fabric; and (d) Massive hydrate fabric. (From Suess et al., 2001)

seafloor as well as in more massive layers at depth. Two types of hydrate fabrics were observed:

- a highly porous fabric with an estimated pore space of approximately 60 vol.-% ((Fig. 3.24c),
- a massive type with no visible pore space ((Fig. 3.24d).

Submersible and deep-towed images showed that the scene at the sea floor of southern summit ((Fig. 3.25) resembles a chaotic landscape dotted with bacterial mats (Fig. 3.25, image a), carbonate pinnacles (Fig. 3.25, image b), methane plumes, clam colonies, and hydrate layers at the seafloor and in the sub-seafloor. Below the sediments surface the porous hydrate fabric was sampled (Fig. 3.25, image c; Fig. 3.24c). This porous hydrate layer is particularly noteworthy in that such a layer contains gas bubbles which may cause significant drop in P-wave velocity. The porous hydrate also has low bulk density, which may cause periodic release of large chunks of hydrate from the sea floor (Fig. 3.25, image d). Such chunks may measure more then 1 meter in diameter. These pieces of floating hydrate constitute an important transport mechanism for methane from the seafloor directly to the atmosphere.

3.7.2 Interpretation of results from waveform inversion

Both OBS and MCS data demonstrate a strong BSR indicating the presence of gas hydrate-sediments beneath the southern summit of the Hydrate Ridge. In the same area gas hydrates were also exposed on the seafloor and two types of hydrate fabrics were clearly observed in samples. The recently acquired well log data provide some

Fig. 3.25. Scene at the sea floor of the southern summit of Hydrate Ridge. (a) Microbial mat; (b) Carbonate pinnacle; (c) Hydrate with bubble-fabric; and (d) Floating hydrate at the sea surface. (From Suess et al., 2001)

background information on P- and S-wave velocities and densities at the Hydrate Ridge area. Combining the result from seismic inversion with the submersible and deep-towed video survey allows interpretation of the inverted Vp profile and distribution of gas hydrates in the study area.

First I can relate the basic feature in the inverted Vp profile to the results of Suess et al. (2001). The inverted (from seismic data) Vp profiles can be interpreted by identifying two types of hydrate fabrics observed by submersible and deep-towed video survey. Fig. 3.26 shows three major zones identified on the inverted Vp profile derived from CMP 1820. The model shows a high velocity hydrate layer sandwiched between two low velocity layers. Immediately below the sea floor the low P-wave velocity (about 1.25-1.5 km/s) may be interpreted as a seismic response to the presence of porous hydrate. The size of pores, as well as the porosity, within the porous hydrate layer gradually decreases downward leading in a positive velocity gradient. High P-wave velocity (1.63-1.72 km/s) below the conversion surface indicates normal massive (non-porous) gas hydrate. The low Vp (1.47-1.62 km/s) layer below this (i.e., below BSR) shows the presence of free gas in the sediment pores. The layer below the free gas zone is likely to be the normal liquid-saturated sedimentary section. The inverted Vp profile suggests that normal gas hydrate occurs at depths of about 65 m below the seafloor. Recent drilling (July 2002) at the southern summit of Hydrate Ridge has confirmed the presence of normal massive gas hydrate at depth that the Vp inversion results suggested. Free gas was encountered below normal massive gas hydrate, but porous hydrate was not found below the sea floor. It is possible that porous hydrate was gradually dissolved, and

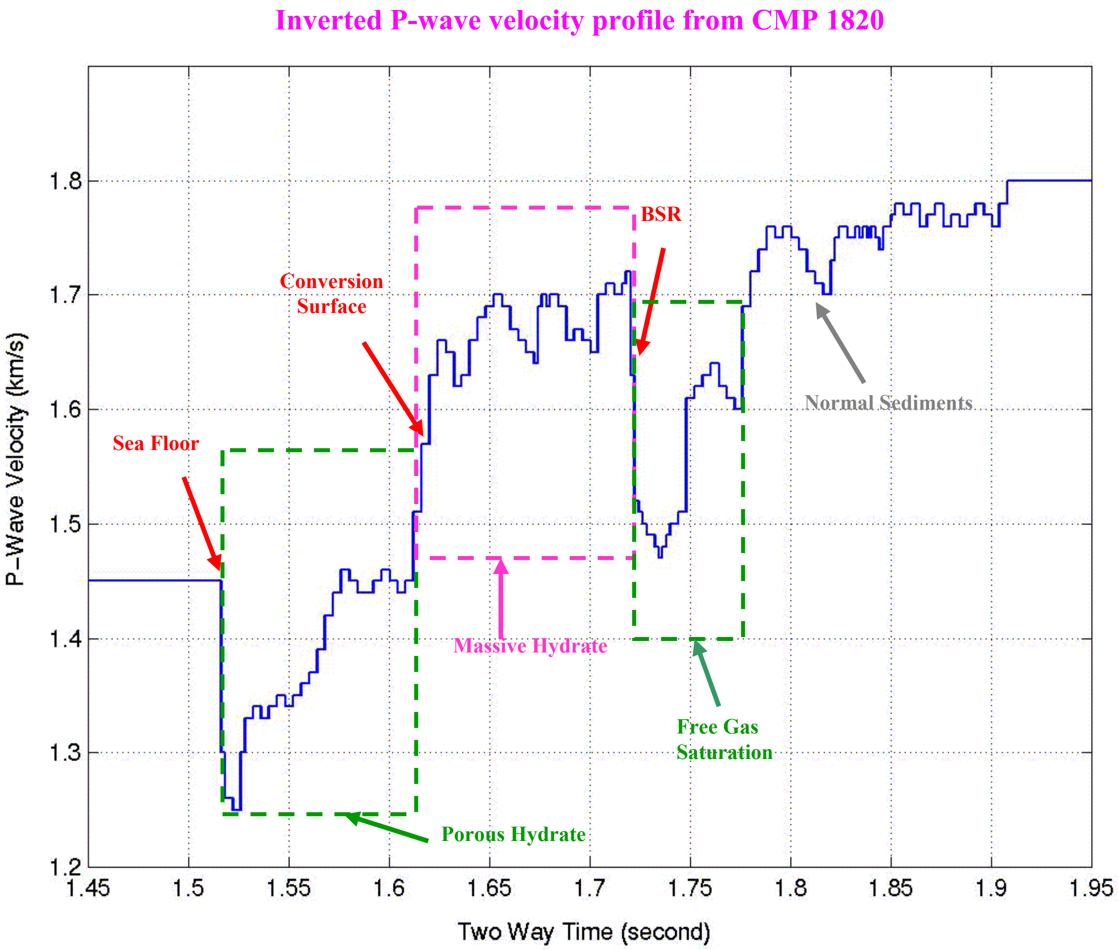

Fig. 3.26. Interpretation of the inverted P-wave velocity profile. Four major layers are identified. Layer 1: Porous hydrate with low P-wave velocity; Layer 2: Normal massive gas hydrate with high P-wave velocity; and Layer 3: Free gas saturation with low P-wave velocity.

small amount of gas in bubble surrounded by thin hydrate skin was gradually mixed into drilling liquids during the actual drilling.

The lateral variations of the identified porous hydrate, massive hydrate and free gas are well defined by the velocity profiles derived from the selected CMP gathers (1780 through 2440) along the Line 103 (Fig. 3.27). Around the ridge, the porous hydrate forms a thicker layer, but it gradually disappears toward land (toward east in the figure) into the slope basin, and disappears seaward from CMP 1800 where a large fault exists. Correspondingly, the normal massive hydrate is not thick, and gradually thickens eastward toward land into the slope basin. Free gas forms a continuous zone below the BSR, and is very thick in the slope basin. A series of faults serve as conduits of ascending fluids and the generous supply of gas controls the distribution of porous hydrate. Free gas rises along the faults to the shallow zone, and spreads laterally to form a steady porous hydrate zone around the ridge where faults are well developed.

Acoustic impedance, the product of bulk density and P-wave velocity, is a tool for identifying lithology. Using the inverted P-wave velocities and background densities, I created acoustic impedance profiles corresponding to the velocity profiles (Fig. 3.28). From Fig. 3.28, we can see a similar distribution and variation of the porous hydrate, massive hydrate and free gas layers as in the Vp-section, but the boundary between porous and massive hydrates is clearer, especially in the slope basin where porous hydrate disappears and massive hydrate dominates.

Poisson's ratio is an excellent indicator of free gas. I used the inverted P-wave velocity profiles as well as the information on S-wave velocity derived from interactive

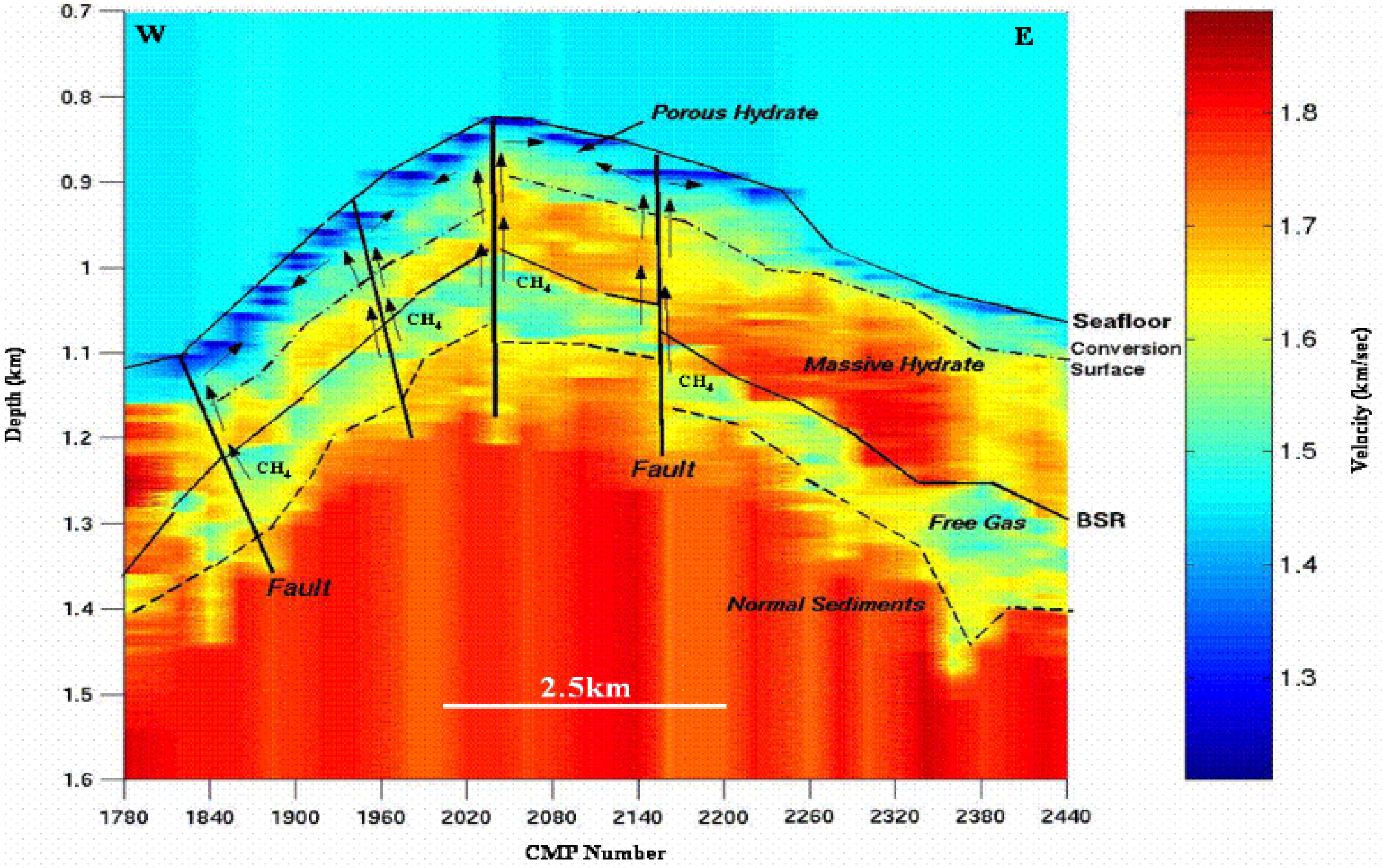

Fig. 3.27. The velocity profiles derived from inversion along the Line 103 across the Hydrate Ridge. Three basic velocity layers are identified below sea floor: Layer 1 — lower velocity, representing porous hydrate; Layer 2 — high velocity, reflecting massive hydrate; Layer 3 — lower velocity, indicating free gas.

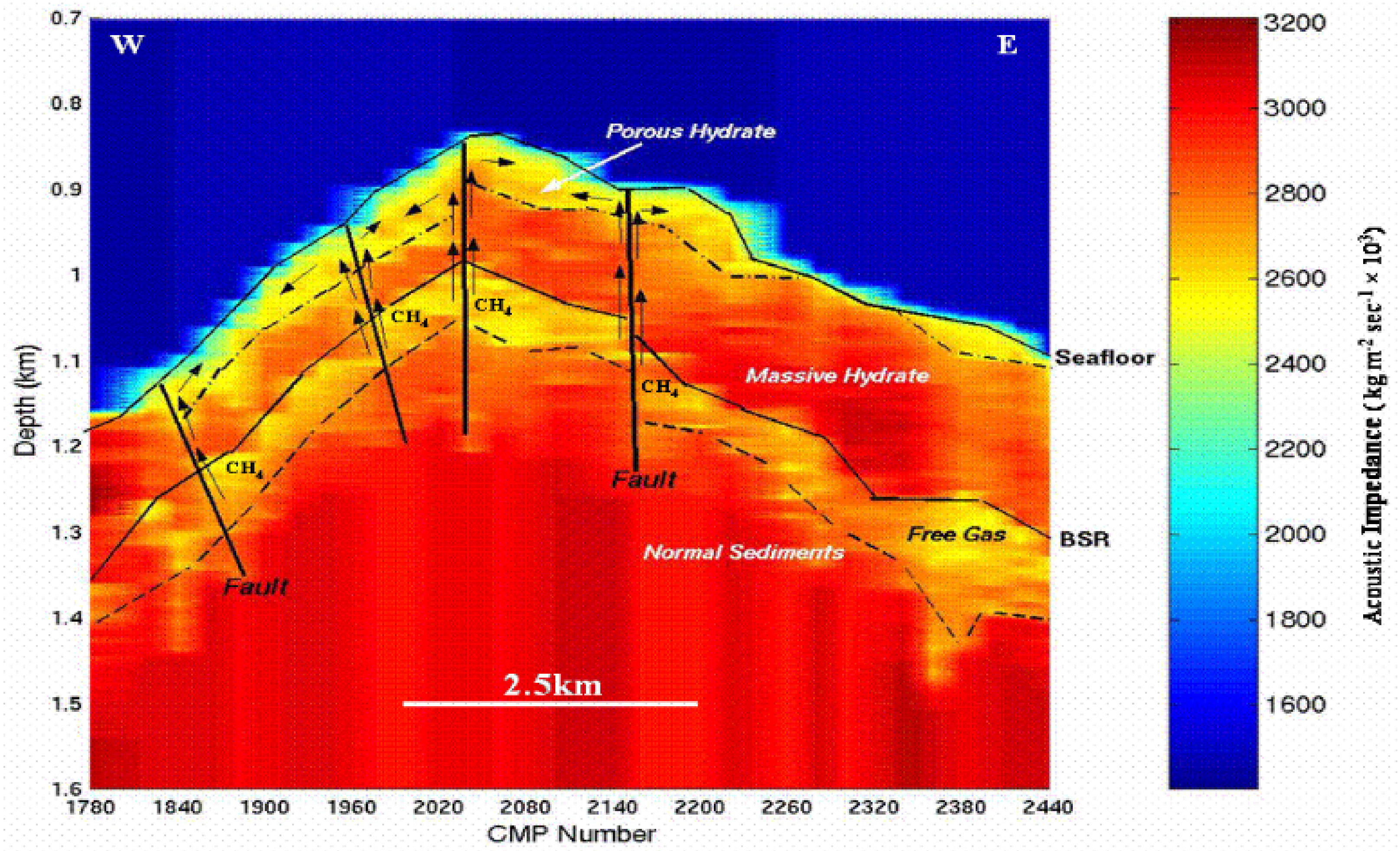

Fig. 3.28. The acoustic impedance profiles produced by given densities (from the guess values of density logs) and estimated velocities from the selected CMP gathers along the Line 103 across the Hydrate Ridge. Three basic layers can be identified below sea floor: Layer 1 — lower velocity, representing porous hydrate; Layer 2 — high velocity, reflecting massive hydrate; Layer 3 — lower velocity, indicating free gas.

travel-time analysis to produce Poisson's ratio profiles shown in Fig. 3.29. The similar trends of the distribution and variation of the three layers shown in Vp and acoustic impedance profiles can still be identified from the Poisson's ratio profiles. The interpreted free gas layer has a very low Poisson's ratio value, less than 0.3 in this area. The normal massive gas hydrate has a Poisson's ratio range of 0.35~0.40. Notice that the lowest values (about 0.2) of Poisson's ratio are found in the shallow porous hydrate layer, especially in the zone close to the seafloor, which may indicate the presence of well-developed porous fabrics saturated with free gas.

3.7.3 Geological interpretation

Comprehensive genetic interpretation of gas hydrates is summarized in Fig. 3.30. A fluid expulsion model for gas hydrate formation has been developed by Hyndman and Davis (1992). The formation of substantial amounts of gas hydrate requires a continuous upward supply of large amounts of methane. Hydrate layers are formed mainly through the removal of methane from upward moving pore fluids as they pass into the hydrate stability field. Fig. 3.30(a**)** is a sketch of accretionary complex showing the methane production, methane removal from upward moving pore fluids, and methane hydrate formation. Original methane is mainly generated in basin sediments. The overall accretion process results in rapid lateral shortening and tectonic vertical thickening of the wedge, and the sediments are transported to greater depth with only minimal porosity loss. Ultimately, the resulting underconsolidated section reestablishes an equilibrium porosity-depth relation through consolidation and fluid expulsion. Fluid

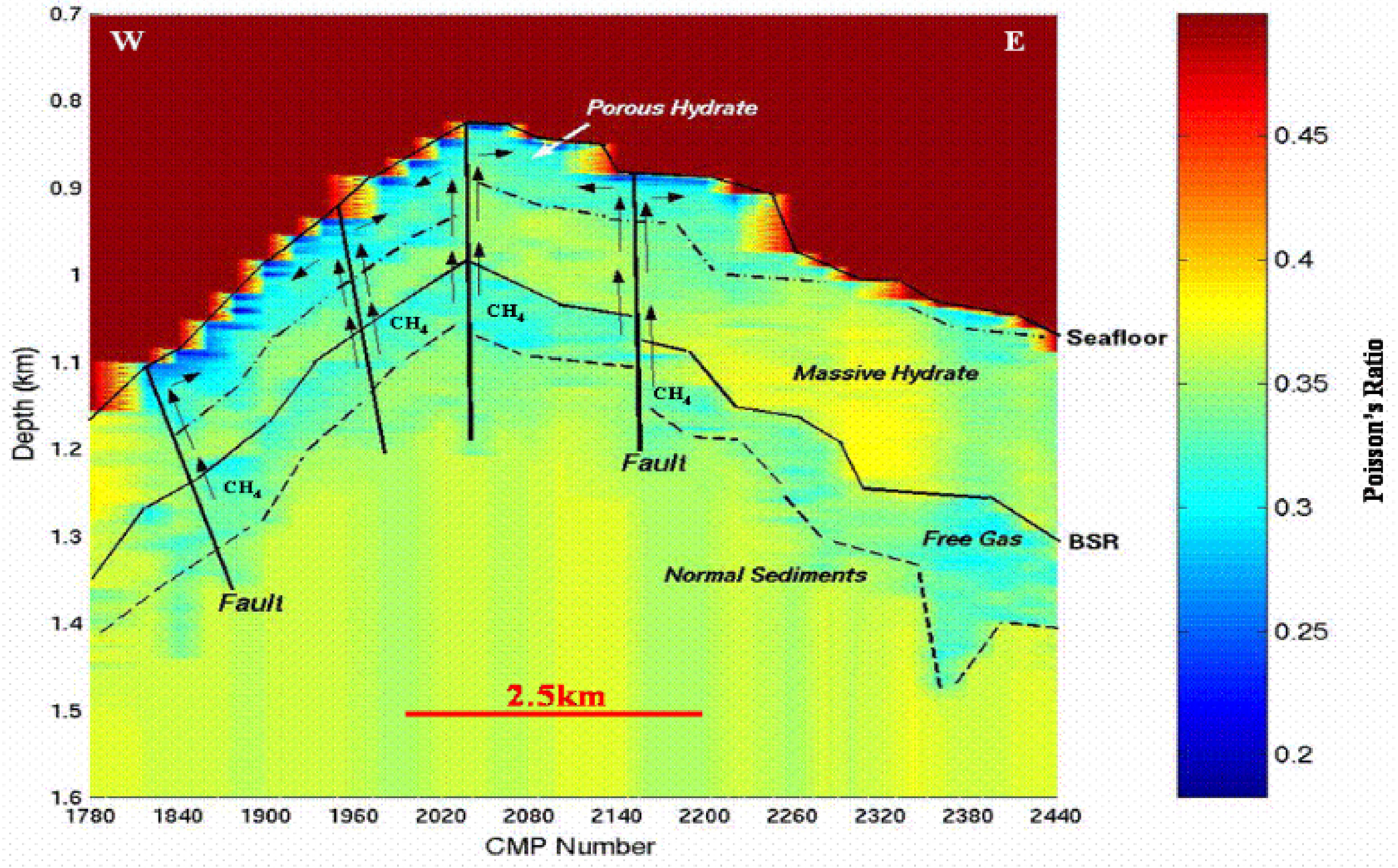

Fig. 3.29. The Poisson's ratio profiles produced by given S-wave velocities and estimated velocities from the selected CMP gathers along the Line 103 across the Hydrate Ridge. Three basic velocity layers are identified below sea floor: Layer 1 — lower velocity, representing porous hydrate; Layer 2 — high velocity, reflecting massive hydrate; Layer 3 — lower velocity, indicating free gas.

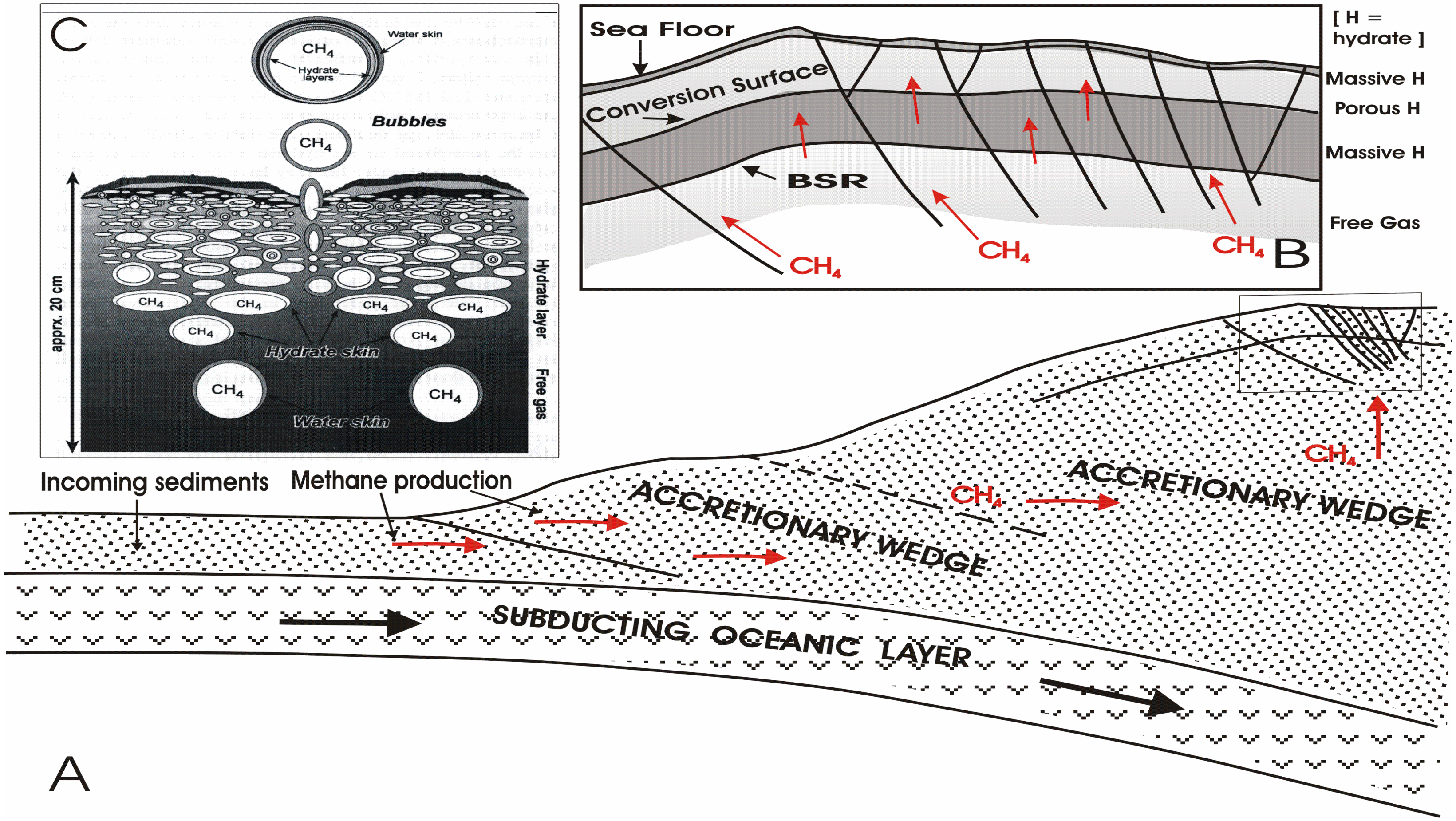

Fig. 3.30. Geological interpretation. A – Sketch of accretionary complex showing production and migration of methane; B – distribution of gas hydrates and free gas at the southern summit of the Hydrate Ridge, two types of gas hydrates: massive hydrate with high velocity, and porous hydrate with low velocity; C – development of bubble fabric and evolution of seafloor hydrate layers (from Suess et al., 2001).

expulsion rates that reach about 1 mm/year (Riedel et al., 2001) appear sufficient to carry enough methane upward to form the observed hydrate saturation over a thickness of about 50 m.

At the southern summit of Hydrate Ridge, the faults related to the evolution and growth of the accretionary complex of Cascadia convergent margin provide the pathways for methane and fluid venting, which have influence on final gas hydrate distribution (Fig. 3.30b). The faults extend through the accreted sediments to below the gas hydrate phase transition. At depth, they tap a fluid reservoir containing free methane. The faults serve as conduits and channel methane up to the near-seafloor where it forms secondary gas hydrates with bubble fabric, or up to the seafloor where it either escapes into the water column or forms secondary gas hydrates with massive fabric. Therefore, thin (less than 0.5 m) massive hydrate, porous hydrate, normal massive hydrate and free gas distribute from the seafloor to below BSR.

Suess et al. (2001) summarized development of bubble fabric and evolution of seafloor hydrate layers at the southern summit (Fig. 3.30c). Hydrate with porous fabric develops from the accumulation of methane bubbles as they become encased in a hydrate skin. Bubbles, rising from the below the seafloor, either escape into the water column or when arrested, turns into hydrate. The porous hydrate fabric consists of macroscopic pores, which are connected by thin veneer of hydrate. Growth of a hydrate skin impedes further reaction between bubble and water. At the seafloor they may form positively buoyant interlayered strata including hydrate, sediments, carbonate, microbial mats, free gas and water.

3.8 Conclusions

The combination of OBS and streamer MCS data allows us to identify the presence of gas hydrate, detect the distribution gas hydrate and interpret the formation of gas hydrate at the Hydrate Ridge offshore Oregon. Some main conclusions are drawn:

- Both 3-D streamer and OBS data show a strong BSR in the sediments under the Hydrate Ridge, which indicates the presence of gas hydrate.
- Interactive P- and S-wave velocity analysis of travel-time information in the OBS data allows us to identify the presence of a conversion surface in the gas hydrate-bearing sediments. The conversion surface separates the overlying low P-wave velocity layer and underlying high P-wave velocity layer.
- The inverted P-wave velocity profiles suggest a low velocity layer existing below the sea floor and above the gas hydrate layer overlying BSR, which differs significantly from the conventional Vp profiles of gas hydrate-bearing sediments, and suggests a new geological model of gas hydrate character and distribution.
- Two types of hydrate fabrics, massive and porous hydrates, observed by deep-towed video survey, have been interpreted in inverted P-wave velocity profiles. Three main layers of gas hydrate-sediments separated by conversion surface and BSR are distinguished downward from the sea floor: layer 1 — low P-wave velocity reflecting the presence of porous hydrate, layer 2 — high P-wave velocity indicating normal massive gas hydrate, and layer 3 — low P-wave

velocity showing the presence of free gas in the porous sediments. Below that is the normal liquid-saturated sedimentary section.

- The profiles reflecting the physical properties of sediments, such as the P-wave velocity, acoustic impedance and Poisson’s ratio profiles, reveal the distribution of gas hydrates and show very similar trends of lateral variation of the main layers.
- A series of faults in the accretionary complex under the ridge not only offer pathways for methane and fluid ascending from deeper layers but also control the distribution of the porous hydrates resultant low velocity below the seafloor.
- Hornbach et al. (2003) suggest their results using velocity analysis of seismic reflection data on the Blake Ridge is the first direct seismic detection of concentrated hydrate confirmed by velocity analysis. My results of direct inversion of seismic data extend these results to greater resolution of the entire seismic data set. Further, my results may be the first seismic indication of visually observed porous hydrate zone.

Chapter 4: Summary and future work

4.1 Summary

Seismic attributes such as traveltimes and reflection amplitude variation with offset contain information on the elastic parameters of subsurface rocks. The aim of generalized inversion of seismic data is to estimate values of the elastic parameters such as P-wave velocity, S-wave velocity and density for lithology discrimination, direct detection of hydrocarbon and estimation of gas hydrate characteristics. Gas hydrate, a new focus of international research, can be identified, mapped and described by seismic data. The inverted data from the central offshore Oregon permit characterization of gas hydrate deposits, including identification of a low-velocity (gas-saturated) porous hydrate zone in the sediments below the sea floor and an anomaly above the normal (high velocity) gas hydrate.

My dissertation research comprises two parts: development of a method to improve the least-squares and the preconditioned conjugate gradient algorithm, and application of the algorithm to inversion of seismic data fro the estimation of detailed velocity structure of gas hydrate-bearing sediments offshore Oregon. Consequently, my dissertation work was reported in three chapters.

In Chapter 1, I briefly reviewed inverse theory and methods with an emphasis to the methods of acoustic impedance inversion and pre-stack waveform inversion. Since the recorded seismic data depend nonlinearly on the parameters describing the earth, nonlinear inverse methods are developed for solving such inverse problems. One important element of inversion is ‘optimization’, which is employed to find an earth model corresponding to the minimum of a function that measures the misfit between observed and synthetic data. For nonlinear inversion in geophysics, popular optimization methods includes global optimization methods such as genetic algorithm and simulated annealing, and local optimization methods such as conjugate gradient algorithm and Newton’s method. In practice, if there is a “good” initial model derived from other related measurements and geologic knowledge of the area, local optimization may be the most efficient approach. Using a local optimization method this nonlinear inverse problem can iteratively be solved by using a generalized least-squares formalism. A conjugate gradient technique is often chosen for solving such a system of equations. In exploration geophysics, some special inverse methods have been developed to solve practical problems. In my dissertation work, the related inverse methods include acoustic impedance inversion (post-stack waveform inversion) and pre-stack waveform inversion. Inversion of post-stack seismic data may yield acoustic impedance as a function of two-way reflection time, from which estimate of velocity profile can be derived when density profile is known. Traditional impedance inversion of a recursive scheme is an excellent method of quickly and inexpensively determining relative impedance changes, but absolute impedance information is very difficult to obtain with this method. To get detailed impedance information for a complex inverse problem, model-based inversion with iterative process is a better choice. Based on the acoustic impedance inversion, I developed an effective method to improve the least-squares and conjugate gradient algorithm, a local optimization. The developed method was applied to estimate the physical properties of the gas hydrate-bearing sediments from seismic data. Gas hydrates are important primarily because they may store large amounts of methane, and secondarily because they influence the physical properties of the gas hydrate-bearing sediments.

In Chapter 2, I reported in detail my new approach of improving the least-squares and conjugate gradient algorithm. I developed a new nonlinear inversion algorithm for estimating velocities from stacked seismic data with application to a field data set consisting of well logs from Ocean Drilling Program (ODP) Leg 170 and multi-channel seismic reflection (MCS) data offshore Costa Rica. Inversion of stacked seismic data generally yields reflection coefficients or impedance as a function of two-way reflection time. In this experiment, seismic data and density logs at selected locations along a 2-D seismic line are inverted to estimate seismic velocities. Mathematically, generalized inversion provides the best estimate of earth model parameters by minimizing the so-called cost (or misfit between observed and computed seismic data) function, which is a function of the data covariance matrix $\mathbf{C}_D$ and the a priori model covariance matrix $\mathbf{C}_M$. Matrices $\boldsymbol{C}_{\boldsymbol{D}}$ and $\boldsymbol{C}_{\boldsymbol{M}}$ (generally approximated by scalars σ_d and σ_m) introduce stability and robustness and thus have strong influence on the quality of the final inversion solution. Based on the least-squares and the preconditioned conjugate gradient algorithm, I have developed a 2-step procedure to solve our nonlinear inverse problem by first determining the two matrices:

- ☐ First step — model smoothing: (1) run inversion for several possible values of (σ_d, σ_m) with a smooth starting model; (2) the error surface as a function of (σ_d,

σ_m) is examined and the region of the error surface with very small value can be chosen as optimal (σ_d, σ_m); and (3) any value of (σ_d, σ_m) from within that region generally produces a good data fit along with realistic smooth model.

- ☐ Second step — data fitting: (1) use the optimal (σ_d, σ_m) to determine matrices C_D and C_M, and use the resulting model from the first step as the starting model; (2) run inversion with no smoothness constraint to get final model and corresponding data fit. This further improves data fitting and includes realistic high frequency variations in the final model.

The inversion results from this experiment show that almost every identified reflector of seismic data is very well matched by final synthetic seismograms, which demonstrates the reliability of the inversion method. The density and inverted velocity profiles allow identification of major stratigraphic boundaries.

In Chapter 3, I focused on the estimation of physical properties of gas hydrate-bearing sediments from OBS and MCS data to detect gas hydrates, map their distribution and interpret their formation. The improved inversion method is extended to the inversion of pre-stack seismic data, which is applied to estimate seismic velocities of gas hydrate-bearing sediments, offshore Oregon. Gas hydrates are recognized as a target for major future energy reserves, are believed to be a potential source of an important greenhouse gas, and are considered as a possible cause of submarine geo-hazard. Natural gas hydrates occur worldwide in marine, permafrost, and lake environments. A simple indicator of gas hydrates in marine is a bottom-simulating reflector (BSR), which marks the transition between hydrate-bearing sediments with high V_p above and the presence of free gas with low V_p below the bottom surface. A 3-D streamer and ocean bottom seismometer (OBS) survey in the Hydrate Ridge, offshore Oregon was carried out to image structures controlling the migration of methane-rich fluid and free gas and to map the gas-hydrate distribution. In my study, I first obtained preliminary V_p and V_s profiles from OBS data by interactive travel-time analysis in τ-p domain, and then used them as a starting model to estimate V_p from the streamer data. The pre-stack waveform inversion of estimating V_p from the streamer data was also conducted in τ-p domain. The main results of my inversion and interpretation study in Hydrate Ridge include:

- A strong BSR, indicating the presence of gas hydrate above and free gas below, was clearly identified from both 3-D streamer and OBS data.
- A conversion surface in the gas hydrate-bearing sediments, separating the overlying low P-wave velocity layer and underlying high P-wave velocity layer, was first identified by interactive P- and S-wave velocity analysis of OBS data.
- A low-velocity layer existing below the sea floor and above the normal gas hydrate was shown in inverted velocity profiles. These profiles are different from the conventional V_p profiles of gas hydrate-bearing sediments, and hence suggest a new geological model of gas hydrates.
- Two types of hydrate fabrics — massive and porous hydrates — are identified, and inverted V_p profile shows a thick (40-60 m) porous hydrate. Three main layers of gas hydrate-sediments separated by conversion surface and BSR are distinguished.

- The profiles reflecting the physical properties of sediments, such as the P-wave velocity, acoustic impedance and Poisson's ratio profiles, are able to map the distribution of gas hydrates and show very similar trends of lateral variation of the main layers.
- Faults in an accretionary complex under the Hydrate Ridge not only offer pathways for methane and fluid ascending from deeper layers but also control the formation of the porous hydrates with low velocity.
- Hornbach et al. (2003) suggest their results using velocity analysis of seismic reflection data on the Blake Ridge is the first direct seismic detection of concentrated hydrate confirmed by velocity analysis. My results of direct inversion of seismic data extend these results to greater resolution of the entire seismic data set. Further, my results may be the first seismic indication of visually observed porous hydrate zone.

4.2 Future Work

In my inversion method of improving the least-squares and conjugate gradient algorithm, a key factor is to determine the data covariance matrix $\boldsymbol{C_D}$ and the *a priori* model covariance matrix $\mathbf{C}_M$. $\boldsymbol{C_D}$ is defined by σ_d^2, the variance of the elements of the seismic data vector, and $\mathbf{C}_M$ is defined by σ_m^2 the variance of the elements of the *a priori* model vector. However, searching for the optimal values of (σ_d, σ_m) in a given large sample space of (σ_d, σ_m) is time-consuming. Therefore, how to determine an effectively small sample space of (σ_d, σ_m) will directly influence on widespread and effective application of this method. In my research, I reduce a 2-D sample space into a 1-D (vector) sample space based on experiment. For more widespread and effective application, however, it is necessary to determine an effectively small sample space directly from the observed data and the used parameters. This requires a generalized method to determine matrices $\boldsymbol{C}_D$ and $\boldsymbol{C}_M$. Therefore, my future work for further improving this nonlinear inversion algorithm will include development of a generalized method to extend its application in various fields.

In my experiment of estimating velocities using 1-D waveform inversion for acoustic impedance with the conjugate gradient technique (see Chapter 2), I assumed that the observed data are uncorrelated, and chose the diagonal matrix as the form of matrix C_D. Indeed, this assumption is effective for determining C_D. However, the really recorded data should be correlated because source wavelet varies with depth. To reflect this reality, I will consider an off-diagonal matrix as the form of matrix C_D in future work.

The estimation of the amount of gas hydrate and free gas from marine seismic data is an important issue. Many rock-physics models for gas hydrate-bearing sediments have been developed to describe velocity-porosity relation, which can be used to predict the velocity of gas hydrate-bearing sediment given rock physical parameters or to estimate the amount of gas hydrate or free gas directly from seismic velocities. The established velocity-porosity relationships include Wood equation (Wood, 1941), Wyllie's time-average equation (e.g., Timur, 1968; Pearson et al.; 1983), and three-phase weighted equation (Lee et al., 1996). In my future work, it is possible to apply a theoretical rock-physics model (such as Dvorkin and Prasad 1999 model) to 2-D or 3-D

Hydrate Ridge marine seismic data to determine gas-hydrate and free-gas saturation. Compared to typical profiles (without gas hydrate or gas) expected and obtained in sediments, the porosity profiles obtained from the inverted interval velocity by using the rock-physics model may demonstrate anomalies where gas hydrate and free gas are present.

In the estimation of physical properties of gas hydrate-bearing sediments from OBS and MCS data, I assumed that the S-wave velocity and density are given, and did inversion only for P-wave velocity. Indeed, I can do inversion for P- and S-wave velocities and density simultaneously. Poisson's ratio is an excellent indicator for free gas. I can invert Poisson's ratio directly in my future work.

The conversion surface identified from interactive analysis of OBS data and from the inverted P-wave velocity profiles from MCS data is not clearly demonstrated in the migrated section of MCS data shown in Fig. 3.23. It may be because the velocity profile used to migrate is a conventional velocity function increasing with depth, which has no low velocity zone below the sea floor. I suggest that the inverted velocity profiles with low velocity zone below the sea floor should be used to seismic migration to map the conversion surface.

The low velocity layer existing below the sea floor and above the normal gas hydrates is a new observation. It offers new insight to interpret formation and distribution of gas hydrates. To further confirm the reliability of the inverted velocity model with a low velocity zone below the sea floor it is necessary to calculate porosities of porous hydrate, massive hydrate and free gas layers using the inverted velocities in my future work. The presence of low velocity porous hydrate may raise a new problem in drilling and development of gas hydrates. Therefore, future work must explore whether the structure of velocity derived from seismic data of the Hydrate Ridge area is local, regional, or global. If this is a more general velocity structure, further work is needed for geological genetic interpretation.

Appendix: Least-Squares and Conjugate Gradient Algorithm

Mora (1987, 1988) and Kormendi and Dietrich (1991) summarized least-squares and conjugate gradient algorithm for nonlinear inversion, which is the base of my new approach — a 2-step procedure method for nonlinear inversion. A detailed introduction to this algorithm is described below.

Formulation of the inverse problem

The general nonlinear forward model is given by:

$$\mathbf{d} = \mathbf{f}(\mathbf{m}), \tag{1}$$

where $\mathbf{m}$ is an earth model vector (parameters), $\mathbf{d}$ is the seismic data vector, and $\mathbf{f}$ is a nonlinear operator mapping the model space M into the data space D.

Given a Gaussian-distributed model and data spaces, the joint *a posteriori* probability function is given by

$$P(\mathbf{d}, \mathbf{m}) = \text{constant} \bullet \exp\,[-\tfrac{1}{2}\,(\Delta\mathbf{d}^T\mathbf{C}_D{}^{-1}\Delta\mathbf{d} + \Delta\mathbf{m}^T\mathbf{C}_M{}^{-1}\Delta\mathbf{m})]\,, \tag{2}$$

where $\Delta\mathbf{d} = \mathbf{d} - \mathbf{d}_{\text{obs}} = \mathbf{f}(\mathbf{m}) - \mathbf{d}_{\text{obs}}$ is the data misfit vector corresponding to the earth model parameters $\mathbf{m}$ and data observations $\mathbf{d}_{\text{obs}}$, $\Delta\mathbf{m} = \mathbf{m} - \mathbf{m}_0$ is the model perturbation vector measured relative to the a priori model $\mathbf{m}_0$, and $\mathbf{C}_D$ and $\mathbf{C}_M$ are the *a priori* data covariance and model covariance matrices respectively. The superscript T denotes the transpose of a matrix.

Clearly, the solution corresponding to the maximum probability (also called maximum *a posteriori* or MAP solution) can be obtained by minimizing the least-squares function, also known as cost (or misfit) function, given by:

$$S(\mathbf{m}) = \tfrac{1}{2}\,(\Delta\mathbf{d}^T\mathbf{C}_D^{-1}\Delta\mathbf{d} + \Delta\mathbf{m}^T\mathbf{C}_M^{-1}\Delta\mathbf{m}), \qquad (3)$$

which is a function of the data covariance matrix $\mathbf{C}_D$ and the *a priori* model covariance matrix $\mathbf{C}_M$.

The aim of least-squares inversion is to infer an optimum model $\mathbf{m}_{\text{opt}}$ which minimizes the cost function $S(\mathbf{m})$. Given a "good" starting model, we can use gradient-based techniques to find the minimum of $S(\mathbf{m})$ iteratively. Gradient methods consist in computing, at each iteration n, a direction of descent $\mathbf{\Phi}_\text{n}$, and a positive step length μ_n along that direction, to satisfy the minimization condition

$$S(\mathbf{m}_\text{n} - \ \mu_\text{n}\,\mathbf{\Phi}_\text{n}) < \text{S}(\mathbf{m}_\text{n}). \qquad (4)$$

This procedure is repeated until a satisfactory result is achieved.

The direction of steepest descent $\mathbf{\Gamma}_n$ is obtained from the gradient of the cost function at a given point $\mathbf{m}_\text{n}$. It is defined by

$$\begin{aligned}\mathbf{\Gamma}_n &= \underline{\mathbf{C}}_M \left.\frac{\partial S}{\partial \mathbf{m}}\right|_{\mathbf{m}=\mathbf{m}_n} \\ &= \underline{\mathbf{C}}_M\,\underline{\mathbf{F}}_n^T\,\underline{\mathbf{C}}_D^{-1}[\mathbf{f}(\mathbf{m}_n) - \mathbf{d}_{\text{obs}}] + (\mathbf{m}_n - \mathbf{m}_0)\,, \qquad (5)\end{aligned}$$

where

$$\underline{\mathbf{F}}_n = \left.\frac{\partial \mathbf{f}}{\partial \mathbf{m}}\right|_{\mathbf{m}=\mathbf{m}_n}$$

is the Frechet derivative matrix. Element (i, j) of matrix Γ_n represents the first-order perturbation of the ith sample of data **d** due to a small perturbation of the jth parameter of model **m**. The steepest descent method uses the direction Γ_n to update the model parameters $\mathbf{m}_\mathrm{n}$ at each iteration.

Because of its simplicity and good convergence property, the conjugate gradient method of nonlinear least-squares is chosen to minimize the cost function for the case of nonlinear function **f**(**m**). The algorithm is iterative with background model varying with each iteration.

Conjugate gradient algorithm

The procedure of the least-squares and the preconditioned conjugate gradient algorithm is summarized by Kormendi and Dietrich (1991) as follows:

Step 1: Compute the synthetic data $\mathbf{d}_n$ for $\mathbf{m}_n$

$$\mathbf{d}_n = \mathbf{f}(\mathbf{m}_n), \qquad n = 0, 1, 2, \ldots.$$

Step 2: Compute the data residuals $\Delta\mathbf{d}$

$$\Delta\mathbf{d}_n = \mathbf{d}_n - \mathbf{d}_{\mathrm{obs}},$$

and the discrepancies with respect to the *a priori* model $\Delta\mathbf{m}_n$

$$\Delta\mathbf{m}_n = \mathbf{m}_n - \mathbf{m}_0.$$

Step 3: Compute the cost function $\boldsymbol{S}(\mathbf{m}_n)$

$$\boldsymbol{S}(\mathbf{m}) = \tfrac{1}{2}\,(\Delta\mathbf{d}^T\underline{\mathbf{C}}_D^{-1}\Delta\mathbf{d} + \Delta\mathbf{m}^T\underline{\mathbf{C}}_M^{-1}\Delta\mathbf{m}),$$

and apply the stopping test (exit if converged).

Step 4: Compute the direction of steepest ascent Γ_n

$\boldsymbol{\Gamma}_n = \underline{\mathbf{C}}_M \underline{\mathbf{F}}_n{}^T \underline{\mathbf{C}}_D{}^{-1} \Delta \mathbf{d} + \Delta \mathbf{m}_n$.

Step 5: Compute the conjugate direction $\boldsymbol{\Phi}_n$

$\boldsymbol{\Phi}_n = \boldsymbol{\Gamma}_n + \sigma_n \boldsymbol{\Phi}_{n-1} \qquad (\boldsymbol{\Phi}_0 = \boldsymbol{\Gamma}_0)$.

Step 6: Compute the optimum step μ_n to minimize the cost (misfit) function (see below).

Step 7: Update the model $\mathbf{m}_n$

$\mathbf{m}_{n+1} = \mathbf{m}_n - \mu_n \boldsymbol{\Phi}_n$,

and go back to step (1).

In step (3), the algorithm is stopped when the cost function becomes less than a predefined minimum value or when a maximum number of iterations is reached. In step (5), the conjugate gradient algorithm is initialized with the steepest descent direction. The coefficient σ_n in the definition of $\boldsymbol{\Phi}_n$ at iteration n is computed from the formula of Polak and Ribiere (1969), which is recommended over other choices by Powell (1981). It is written by

$$\sigma_n = \frac{(\boldsymbol{\Gamma}_n - \boldsymbol{\Gamma}_{n-1})^T \underline{\mathbf{C}}_M^{-1} \boldsymbol{\Gamma}_n}{\boldsymbol{\Gamma}_{n-1}^T \underline{\mathbf{C}}_M^{-1} \boldsymbol{\Gamma}_{n-1}}, \tag{6}$$

Step (6) is the heart of the algorithm. The computation of optimum step μ_n is based on a linear search along the direction $\boldsymbol{\Phi}_n$ to find a real positive number minimizing the cost function. This success-failure procedure requires the computation of the cost function, and therefore the computation of synthetic data (seismic response of the medium), for each tested value of μ_n (typically 3). The optimum step is finally computed from a three-point parabolic inverse interpolation (Nash, 1979). The value thus obtained is used to compute the new model, its synthetic data (seismic response), and the corresponding Frechet derivatives; it also serves as a starting value fro the linear search at the next iteration. The benefits of this approach are a considerable reduction of the costly Frechet derivative computations and the certainty of having found the best value of μ at the current iteration. At the first iteration, an initial value for μ_0 is obtained by linearizing $\mathbf{f}(\mathbf{m}_0)$ around $\mathbf{m}_0$ and by canceling the derivative of the cost function with respect to μ_0. This gives

$$\mu_0 = \frac{\mathbf{\Gamma}_0{}^T \underline{\mathbf{C}}_M^{-1} \mathbf{\Phi}_0}{\mathbf{\Phi}_0^T (\underline{\mathbf{C}}_M^{-1} + \mathbf{F}_0^T \underline{\mathbf{C}}_D^{-1} \mathbf{F}_0) \mathbf{\Phi}_0} . \tag{7}$$

The above expression can easily be computed because the Frechet derivatives are obtained as a simple byproduct of the forward modeling scheme. A similar formula can be derived for the following values of μ_n, but these “blind” definitions of the optimum step length often yield very underestimated values of μ.

REFERENCES

Aki, K., and Richards, P.G., 1980, Quantitative seismology: Freeman &Co.

Alterman, Z., and Karal, F. C., 1968, Propagation of elastic waves in layered media by finite-difference methods: Bull., Seis. Soc. Am., **58**, 367-398.

Aubouin, J., et al., 1982, Initial reports of the Deep Sea Drilling Project, vol. **67**, 799pp.: U.S. Government Printing Office, Washington D.C.

Bamberger, A., Chavent, G., and Lailly, P., 1979, About the stability of the inverse problem in 1-D wave equations—Application to the interpretation of seismic profiles: Applied Mathematics and Optimization, **5,** 1-47.

Bamberger, A., Chavent, G., Hemon, Ch. and Lailly, P., 1982, Inversion of normal incidence seismograms: Geophysics, **47**, 757-770.

Becquey, M., Lavergne, M., and Willm, C., 1979, Acoustic impedance logs computed from seismic traces: Geophysics, **44**, 1485-1501.

Berteussen, K. A., and Ursin, B., 1983, Approximate computation of the acoustic impedance from seismic data: Geophysics, **48**, 1351-1358.

Bessonova, E.N., Fishman, V.M., Pyaboyi, V.Z., and Sitnikova, G.A., 1974, The tau-method forinversion of travel time — I. Deep seismic sounding data: Geophys. J. R. Astron. Soc., **36**, 377-398.

Bohrmann, G., Greinert, J., Suess, E., and Torres, M., 1998, Authigenic carbonates from the Cascadia subduction zone and their relation to gas hydrate stability: Geology, **26**, 647-650.

Buffett, B.A., 2000, Clathrate Hydrates: Annu. Rev. Earth Planet. Sci., **28**, 477-507.

Carcione, J. M., Herman, G., C., and ten Kroode, A. P. E., 2002, Seismic modeling: Geophysics, **67**, 1304-1325.

Cerveny, V., 1972, Seismic ray and ray intensities in inhomogeneous anisotropic media: Geophys. J. Roy. Astr. Soc., **29**, 1-13.

Chapman, C. H., and Orcutt, J. A., 1985, The computation of body-wave synthetic seismograms in laterally homogeneous media: Rev. Geophys., **23**, 105-163.

Chapman, N.R., Gettrust, J.F., Walia, R., Hannay, D., Spence, G.D., Wood, W.T., and Hyndman, R.D., 2002, High-resolution, deep-towed, multichannel seismic survey of deep-sea gas hydrates off western Canada: Geophysics, **67**, 1038-1047.

Christeson, G.L., McIntosh, K.D., and Shipley, T.H., 1999, Structure of the Costa Rica convergent margin, offshore Nicoya Peninsula: J. Geophys. Res., **104**, 25443-25468.

Claypool, G.W., and Kaplan, I.R., 1974, The origin and distribution of methane in marine sediments, in: Natural Gases in Marine Sediments, Kaplan, I.R., ed., p. 99-139, Plenum, New York, NY.

Claypool, G.W., and Kvenvolden, K.A., 1983, Methane and other hydrocarbon gases in marine sediment: Ann. Rev. Earth Palnet. Sci., **11**, 299-327.

Clayton, R. W., and Stolt, R. H., 1981, A Born-WKBJ inversion method for acoustic reflection data: Geophysics, **46**, 1559-1567.

Collett, T.S., 1993, Natural gas hydrates of the Prudhoe Bay and Kuparuk River area, North Slope, Alaska: AAPG Bulletin, **77**, 793-812.

Collett, T.S., 2002, Energy resource potential of gas hydrates: AAPG Bulletin, **86**, 1971-1992.

Cooke, D., A., and Schneider, W. A., 1983, Generalized linear inversion of reflection seismic data: Geophysics, **48**, 665-676.

DeMets, C., Gordon, R. G., Argus, D. F., and Stein, S, 1994, Effect of recent revisions to the geomagnetic reversal time scale on estimates of current plate motions: Geophys. Res. Lett., **21**, 2191-2194.

Dickens, G.R., and Quinby-Hunt, M.S., 1997, Methane hydrate stability in pore water: A simple theoretical approach for geophysical applications: Journal of Geophysical Research, **102**, 773-783.

Dickens, G.R.M., Castillo, M., and Walker, J.C.G., 1997, A blast of gas in the latest Paleocene: Simulating first-order effects of massive dissociation of oceanic methane hydrate: Geology, **25**, 259-262.

Domenico, S.N., 1977, Elastic properties of unconsolidated porous sand reservoirs: Geophysics, **42**, 1339-1368.

Donnelly, T. W., 1994, The Caribbean Cretaceous basalt association: a vast igneous province that includes the Nicoya Complex of Costa Rica, *in*: H. Seyfried, and W. Hellmann (Eds.), Profil 7, University of Stuttgard, pp. 17-45.

Dvorkin, J., Prasad, M., Sakai, A., and Lavoie, D., 1999, Elasticity of marine sediments: Rock physics modeling: Geophys. Res. Lett., **26**, 1781-1784.

Fuchs, K., and Muller, G., 1971, Computation of synthetic seismograms with the reflectivity method and comparison with observations: Geophys. J. R. Astr. Soc., **23**, 417-433.

Gajewski, D., and Psencik, I., 1987, Computation of high frequency seismic wavefields in 3-D laterally inhomogeneous anisotropic media: Geophys. J. Roy. Astr. Soc., **91**, 383-411.

Galli-Olivier, C., 1979, Ophiolite and island-arc volcanism in Costa Rica: Geol. Soc. Am. Bull., **90**, 444-452.

Gauthier, O., Virieux, J., and Tarantola, A., 1986, Two-dimensional nonlinear inversion of seismic waveforms: Numerical results: Geopgyics, **51**, 1387-1403.

Grauls, D., 2001, Gas Hydrates: importance and applications in petroleum exploration: Marine and Petroleum Geology, **18**, 519-523.

Hampson, D., 1991, AVO inversion: theory and practice: The Leading Edge, **10**, 39-42.

Henriet, J.P., and Mienert, J., eds., 1998, Gas hydrate—Relevance to world margin stability and climate change: Geological Society (London) Special Publication **137**, 338p.

Henry, M., Orcutt, J.A., and parker, R.L., 1980, A new method for slant stacking refraction data: Geophys. Res. Lett., **7**, 1073-1076.

Hornbach, M.J., Holbrook, W.S., Gorman, A.R., Hackwith, K.L., Lizarralde, D., and Pecher, I., 2003, Direct seismic detection of methane hydrate on the Blake Ridge: Geophysics, **68**, 92-100.

Hyndman, R.D., and Davis, E.E., 1992, A mechanism for the formation of methane hydrate and seafloor bottom simulating reflectors by vertical fluid expulsion: Journal of Geophysical Research, **97**(B5), 7025-7041.

Hyndman, R.D., Foucher, J.P., Yamano, M., Fisher, A., and Scientific Team of Ocean Drilling program Leg 131, 1992, Deep sea bottom-simulating-reflectors: Calibration of bases of the hydrate stability field as used for heat flow estimates, Earth Planet. Sci. Lett., **109**, 289-301.

Hyndman, R.D., and Spence, G.D., 1992, A seismic study of methane hydrate marine bottom simulating reflectors: Journal of Gephysical Research, **97**(B5), 6683-6698.

Ikelle, L. T., Diet, J. P., and Tarantola, A., 1986, Linearized inversion of multioffset seismic reflection data in the ω-k domain: Geophysics, **51**, 1266-1276.

Ikelle, L. T., Diet, J. P., and Tarantola, A., 1988 Linearized inversion of multioffset seismic reflection data in the ω-k domain: Depth-dependent medium: Geophysics, **53**, 50-64.

Jakobsen, M., Hudson, J.A., Minshull, T.A., and Singh, S.C., 2000, Elastic properties of hydrate-bearing sediments using effective medium theory: J. Geophys. Res., **105**, 561-577.

Kappus, M.E., Harding, A.J., and Orcutt, J.A., 1990, A coparison of tau-p transform methods: Geophysics, **55**, 1202-1215.

Kastner, M., Kvenvolden, K.A., Whiticar, M.J., Camerlenghi, A., and Lorenson, T.D., 1995, Relation between pore fluid chemistry and gas hydrates association with bottom-similating reflectors at the Cascadia Margin, sites 889 and 892, in: Proc. Ocean Drill. Program Sci. Results, Carson, B., Westbrook, R.J., Musgrave, R.J., Suess, E., eds., **146** (part 1), 175-197.

Kastner, M., Kvenvolden, K.A., and Loreson, T.D., 1998, Chemistry, isotopic composition, and origin of methane hydrogen sulfide hydrate at the Cascadia subduction zone: Earth Planet. Sci. Lett., **156**, 173-183.

Kelly, K. R., Ward, R. W., Treitel, S., and Alford, R. M., 1976, Synthetic seismiograms: A finite-difference approach: Geophysics, **41**, 2-27.

Kennett, B. L. N., 1983, Seismic wave propagation in stratified media: Cambridge University Press.

Kimura, G., Silver, E., Blum, P. et al., 1997, Proc. ODP, Init. Repts. **170**, Ocean Drilling Program, College Station, TX.

Klitgord, K. M., and Mammerickx, 1982, Northern East Pacific Rise: magnetic anomaly and bathymetric framework: J. Geophys. Res., **87**, 6725-6750.

Kormendi, F., and Dietrich, M., 1991, Nonlinear waveform inversion of plane-wave seismograms in stratified elastic media: Geophysics, **56**, 664-674.

Kvenvolden, K.A., 1988a, Methane hydrates—A major reserve of carbon in the shallow geosphere?: Chemical Geology, **71**, 41-51.

Kvenvolden, K.A., 1988b, Methane hydrates and global climate: Global Biochemical Cycles, **2**, 221-229.

Kvenvolden, K.A., 1993, Methane hydrates—Geological perspective and global change: Reviews of Geophysics, **31**, 173-187.

Kvenvolden, K.A., and Barnard, L.A., 1983, Hydrates of natural gas in continental margins, *in*: Studies in Continental Margin Geology, edited by J.S. Watkins and C.L. Drake, Mem. Am. Asso. Petrol. Geol., **34**, 631-640.

Kvenvolden, K.A., and Kastner, M., 1990**,** Gas hydrates of the Peruvian outer continental margin, *In*: E. Sues, R. von Huene et al., Proceedings of the Ocean Drilling Program, Scientific Results, **112**, 517-526.

Kvenvolden, K.A., and Lorenson, T.D., 2001, The global occurrence of natural gas hydrates, *In*: C.K. Paul, and W.P. Dillon, eds., Natural Gas Hydrates: Occurrence, Distribution, and Detection, Geophysical Monograph **124**, 3-18.

Kvenvolden, K.A., and McDonald, T.j., 1985, Gas hydrates of the Middle American Trench—Deep Sea Drilling Project Leg 84, in: Initial Reports of the Deep Sea Drilling Project, v. **84**, edited by R. von Huene et al., p. 667-682, U.S. Government Printing Office, Washinton, D.C.

Latimer, R. B., Davison, R., and van Riel, P., 2000, An interpreter's guide to understanding and working with seismic-derived acoustic impedance data: The Leading Edge, **March**, 242-256.

Lee, M.W., Hutchinson, D.R., Collett, T.S., and Dillon, W.P., 1996, Seismic velocities for hydrate-bearing sediments using a weighted equation: Journal of Geophysical Research, **101**, 20347-20359.

Lindeseth, R. O., 1979, Synthetic sonic logs—a process for stratigraphic interpretation: Geophysics, **44**, 3-26.

Lines, L. R., and Treitel, S., 1984, Tutorial: A review of least-squares inversion and its application to geophysical problems: Geophysical Prospecting, **32**, 159-186.

Linke, P., Suess, E., Torres, M., Martens, V., Rugh, W.D., Ziebis, W., and Kulm, L.D., 1994, In situ measurement of fluid flow from cold seeps at active continental margins: Deep Sea Research, **41**, 721-739.

Lundberg, N., 1982, Evolution of the slope landward of the Middle America Trech, Nicoya Peninsula, Costa Rica, *in*: J. K. Leggett, ed., Trech-Forearc Geology, *Geol. Soc. London Spec. Publ.*, **10**, 131-147.

Mackay, M.E., 1995, Structural variation and landward vergence at the toe of the Oregon accretionary prism: Tectonics, **14**, 1309-1320.

Markl, R.G., Bryan, G.M., and Ewing, J.I., 1970, Structure of the Blake-Hahama Outer Ridge: Journal of Geophysical Research, **75**, 4539-4555.

McIntosh, K. D., and Sen, M. K., 2000, Geophysical evidence for dewatering and deformation processes in the ODP Leg 170 area offshore Costa Rica: Earth and Planetary Science Letters, **178**, 125-138.

McIver, R.D., 1982, Role of naturally occurring gas hydrates in sediment transport: AAPG Bulletin, **66**, 789-792.

Menke, W., 1984, Geophysical data analysis: Discrete inverse theory: Academic Press.

Meschede, M., Barckhausen, U., and Worm, H. U., 1998, Extinct spreading on the Cocos Ridge: Terra Nova, **10**, 211-216.

Meschede, M., and Frisch, W., 1994, Geochemical characteristics of basaltic rocks from the central America ophiolites: Profil, **7**, 71-85.

Mora, P., 1987, Nonlinear two-dimensional elastic inversion of multioffset seismic data: Geophysics, **52**, 1211-1128.

Mora, P., 1988, Elastic wave-field inversion of reflection and transmission data: Geophysics, **53**, 750-759.

Nolte, B., and Frazer, L. N., 1994, Vertical seismic profile inversion with genetic algorithms: Geophys. J. Int., **117**, 162-178.

Norton, S. J., 1988, Iterative seismic inversion: Geophysical Journal of the Royal Astronomical Society, **94**, 457-468.

Oldenburg, D. W., Scheuer, T., and Levy, S., 1983, Recovery of the acoustic impedance from reflection seismograms: Geophysics, **48**, 1318-1337.

Paull, C.K., Ussler, W., III, and Dillon, W.P., 1991, Is the extent of glaciation limited by marine gas-hydrates?: Geophysical Research Letters, **18**, 432-434.

Pearson, C.F., Halleck, P.M., McGuire, P.L., Hermes, R., and Mathews, M., 1983, Natural gas hydrates: A review of in-situ properties: Journal of Physical Chemistry, **87**, 4180-4185.

Pica, A., Diet, J. P., and Tarantola, A., 1990, Nonlinear inversion of seismic reflection data in laterally invariant medium: Geophysics, **55**, 284-292.

Riedel, M., Spence, G.D., Chapman, N.R., and Hyndman, R.D., 2001, Deep-sea gas hydrates on the northern Cascadia margin: The Leading Edge, **20**, 87-91, 109.

Sambridge, M., and Drijkoningen, G., 1992, Genetic algorithms in seismic waveform inversion: Geophys. J. Int., **109**, 323-342.

Schmidt-Effing, R., 1979, Alter und Genese des Nicoya-Komplexes, ein ozeanischer Palaokruste (Oberjura bis Eozan) im sudlichen Zentral Amerika: Geol. Rundsch., **68**, 457-494.

Sen, M. K., and Stoffa, P. L., 1992a, Rapid sampling of model space using genetic algorithms: Examples from seismic waveform inversion: Geopgys. J. Internat., **108**, 281-292.

Sen, M. K., and Stoffa, P. L., 1992b, Genetic inversion of AVO: The Leading Edge, **11**, 27-29.

Sen, M. K., and Stoffa, P. L., 1995, Global optimization methods in geophysical inversion: Elsevier Sciecne B.V.

Sen, M. K., and Stoffa, P. L., 1996, Bayesian inference, Gibbs' sampler and uncertainty estimation in geophysical inversion: Geophysical Prospecting, **44**, 313-350.

Sen, M.K., Wang, C. and Bangs, N., 2001, Converted waves from gas hydrates: Constraints on the shear velocity structure of shallow sediments in Oregon continental margin:7th International Cogress of the Brazilian Geophysical Society, Salvador.

Sen, M. K., and Roy, A., 2002, Constrained waveform inversion of reflection seismic data, Geophysical J. International, Submitted.

Shipley, T.H., Houston, M.H., Buffler, R.T., Shaub, F.J., McMillan, K.J., Ladd, J.W., and Worzel, J.L., 1979, Seismic evidence for widespread possible gas hydrate horizons on continental slopes and rises: American Association of Petroleum Geologists Bulletin, **63**, 2204-2213.

Shipley, T.H., McIntosh, K.D., Silver, E.A., and Stoffa, 1992, Three-dimensional seismic imaging of the Costa Rica accretionary prism: Structural diversity in a small volume of the lower slope: J. Geophys. Res., **97**, 4439-4459.

Shipley, T.H., Stoffa, P.L., and Dean, D., 1990, Underthrust sediments, fluid migration paths and mud volcanoes associated with the accretionary wedge off Costa Rica: Middle American Trench: J. Geophys. Res., **95**, 8743-8752.

Simmons, J. L., Jr., and Backus, M. M., 1996, A metched-filter approach to impedance estimation: Geophysics, **61**, 484-495.

Sinton, C. M., Duncan, R. A., and Denyer, P., 1997, Nicoya Peninsula, Costa Rica: a single suite of Caribbean oceanic plateau magmas: J. Geophys. Res., **102**, 15507-15520.

Sloan, E.D., Jr., 1990, Clathrate hydrates of natural gases: Marcel Dekker, 641p.

Sloan, E.D., Jr., 1998, Clathrate hydrates of natural gases, 2nd ed.: Marcel Dekker, 705p.

Stoffa, P.L., Buhl, P., Diebold, J.B., and Wenzel, F., 1981, Direct mapping of seismic data to the domain of intercept time and ray parameter – A plane-wave decomposition: Geophysics, **46**, 255-267.

Stoffa, P.L, Shipley, T.H., Kessinger, W., Dean, D.F., Elde, R., Silver, E., Reed, D., and Aguilar, A., 1991, Three-dimensional seismic imaging of the Costa Rica accretionary prism: Field program and migration examples: J. Gepohys., Res., **96**, 21693-21712.

Stoll, R.D., 1974, Effect of gas hydrates in sediments, in: Kaplan, I.R., ed., Nature of gases in marine sediments: Plenum, Press, 235-248.

Stoll, R.D., and Bryan, G.M., 1979, Physical properties of sediments containing gas hydrates: Journal of Geophysical Research, **84**, 1629-1634.

Suess, E., Torres, M.E., Bohrmann, G., Collier, R.W., Greinert, J., Linke, P., Rehder, G., Trehu, A., Wallmann, K., Winckler, G., and Zuleger, E., 1999, Gas hydrate destabilization: enhanced dewatering, benthic material turnover and large methane plumes at the Cascadia convergent margin: Earth Planet. Sci. Lett., **170**, 1-15.

Suess, E., Torres, M.E., Bohrmann, G., Collier, R.W., Rickert, D., Goldfinger, C., Linke, P., Heuser, A., Sahling, H., Heeschen, K., Jung, C., Nakamura, K., Greinert, J., Pfannkuche, O., Trehu, A., Klinkhammer, G., Whiticar, M.J., Eisenhauer, A., Teichert, B., and Elvert, M., 2001, Sea floor methane hydrates at Hydrate Ridge, Cascadia Margin, In: C.K. Paul, and W.P. Dillon, eds., Natural Gas Hydrates: Occurrence, Distribution, and Detection: Geophysical Monograph **124**, 87-98.

Tarantola, A., and Valette, B., 1982, Inverse problem = quest for information: J. Geophys., **50**, 159-170.

Tarantola, A., 1984a, Linearized inversion of seismic reflection data: Geophys. Prosp., **32**, 998-1015.

Tarantola, A., 1984b, The seismic reflection inverse problem, *in* Inverse problems of acoustic and elastic waves, Santosa, F., Pao, Y. H., Symes, W., and Holland, Ch., Eds.: Soc. Industr. Appl. Math.

Tarantola, A., 1987, Inverse problem theory: Methods of data fitting and model parameter estimation: Elsevier Publishing Company.

Tatham, R.H., 2002, Future directions of multicomponent seismic methods in the marine environment: The Leading Edge, **April**, 377-378.

Teichert, B., and Elvert, M., 2001, Sea floor methane hydrates at Hydrate Ridge, Cascadia Margin: C.K. Paull and W.P. Dillon, eds., Natural Gas Hydrates: Occurrence, Distribution, and detection, Geophysical Monograph 124, American Geophysical Union, Washington, DC.

Thomsen, L., 1999, Converted-wave reflection seismology over inhomogeneous, anisotropic media: Geophysics, **64**, 678-690.

Timur, A., 1968, velocity of compressional waves in porous mediam at permafrost temperature: Geophysics, **33**, 584-595.

Torres, M.E., Bohrmann, G., Brown, K., de Angelis, M.A., Hammond, D., Klinkhammer, G., McManus, J., Suess, E., and trehu, A.M., 1999, Geochemical observation on Hydrate Ridge, Cascadia margin, July 99: OSU Data Report **174**, ref. 99-3, 87p.

Trehu, A.M., Lin, G., Maxwell, E., and Goldfinger, C., 1995, A seismic reflection profile across the Cascadia subduction zone offshore central Oregon: New constraints on methane distribution and crustal structure, Journal of Geophysical research, **100**, 15101-15116.

Trehu, A.M., Torres, M.E., Moore, G.F., Suess, E., and Bohrmann, G., 1999, Temporal and spatial evolution of a gas hydrate-bearing accretionary ridge on the Oregon continental margin: Geology, **27**, 939-942.

Treitel, S., Gutowski, P., and Wagner, D., 1982, Plane-wave deconvolution of seismograms: Geophysics, **47**, 1375-1401.

Tucholke, B.E., Bryan, G.M., amd Ewing, J.J., 1977, Gas hydrate horizons detected in seismic-profile data from the western North Atlantic: AAPG Bulletin, **61**, 698-707.

Ursin, B, 1986, Complete inversion of zero-offset seismic data: Geophysical Prospecting, **34**, 1213-1218.

von Huene, R., and Flueh, E., 1994, A review of marine geophysical studies along the Middle American Trench off Costa Rica and the problematic seaward terminus of continental crust, *in*: H. Seyfried and W. Hellmann, eds., Profil **7**, pp. 143-159: Univ. of Stuttgart, Stuttgart, Germany.

von Huene, R. et al., 1985, Initial Reports of the Deep Sea Drilling Project, vol. **84**, 967pp.: U.S. Government Printing Office, Washington D.C.

Westbrook, G.K., Carson, B., Musgrave, R.J., and Leg 146 Scientific Party, 1994, Processings, Ocean Drilling Program, Initial Reports, v. **146**, Ocean Drilling Program, College Station, TX, 609p.

Whalley, E., 1980, Speed of longitudinal sound in clathrate hydrates: Journal of Geophysical Research, **85**, 2539-2542.

Wiggins, R. A., 1977, Minimum entropy deconvolution: Proc. Int. Symp. Computer Aided Seismic Analysis and Discrimination, 7-14.

Wood, A.B., 1941, A textbook of sound: G. Bell & Sons, Ltd.

Ye, S., Bialas, J., Flueh, E., Stavenhagen, A., and von Huene, R., 1996, Crustal structure of the Middle American Trench off Costa Rica from wide-angle seismic data: Tectonics, **15**, 1006-1021.

VITA

Chengshu Wang was born in Linshui county, Sichuan province, China on March 13, 1962, the second child of Shengyao Wang and Qionghua Feng. He completed his High School study at the Jiulong High School in 1978. After that, he was accepted into his college education with a major in Geology in the Department of Petroleum Exploration, the Southwestern Institute of Petroleum from October 1978 through July 1982. After his graduation with a B. E. degree, he joined the Sichuan Bureau of petroleum and served first as a technician and then an assistant engineer from August, 1982 through August, 1984. He was accepted into M. Sc. program at the Beijing Graduate School, Wuhan College of Geology (currently named China University of Geosciences, Beijing) from the Sptember 1984 and July 1987. After getting his M. Sc. degree in Geology, he joined the Institute of Geology, Chinese Academy of Geological Sciences, and served first as an assistant research scientist and then as an associate research scientist (1994 through 1996) for a total of 9 years. In the Fall semester of 1996, he enrolled into the Ph.D. program in Geological Sciences at the University of Texas at Austin. Upon graduation, he will join CNPC (China National Petroleum Corporation).

Permanent address: Institute of Geology, 26 Baiwanzhuang Road, Beijing 100037, P. R. China.

This dissertation was typed by the author.